Plasmon-Enhanced Dynamic Light Scattering of Gold Nanorods in Bulk and Near a Wall

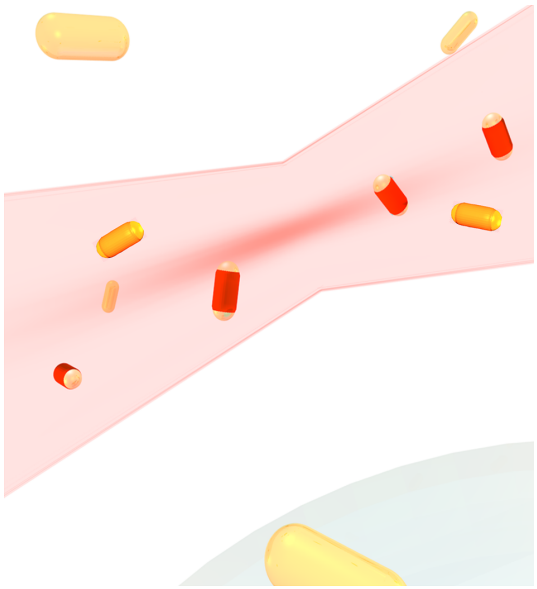

Dissertation

zur Erlangung des Grades

„Doktor der Naturwissenschaften“

im Promotionsfach Physik

Fachbereich Physik, Mathematik und Informatik

der Johannes Gutenberg-Universität Mainz

vorgelegt von

Maryam Haghighi

geboren in Neyriz/Iran

Mainz, April 2014

This dissertation is the result of work carried out in the Physics at Interfaces Group at the Max Planck Institute for Polymer Research (MPI-P) from [in printed version available] until [in printed version available] under the supervision of Prof. Dr. [in printed version available] and Prof. Dr. [in printed version available].

Tag der mündlichen Prüfung:	03.07.2014
Erster Berichterstatter:	[in printed version available]
Zweiter Berichterstatter:	[in printed version available]

The picture on the front page shows the schematic representation of the enhancement of the anisotropic scattering as a consequence of the excitation of a longitudinal plasmon mode.

Abstract

The transport processes of anisotropic metallic nanoparticles such as gold nanorods (GNRs) in complex liquids and/or confined geometries play a significant role in a wide range of biomedical and industrial applications. One route towards a deeper fundamental understanding of transport mechanisms is the use of two powerful methods - Dynamic Light Scattering (DLS) in bulk and Resonance Enhanced Dynamic Light Scattering (REDLS) close to a wall.

In this thesis, nanomolar suspensions of GNRs stabilized with cetyltrimethylammonium bromide (CTAB), were analyzed in bulk by DLS and close to a solid interface by REDLS. In bulk, a wavelength-dependent enhancement of the anisotropic scattering as a consequence of the excitation of a longitudinal surface plasmon resonance (LSPR) mode has been observed. The strong scattering intensity near the LSPR frequency for rods oriented parallel to the excitation optical field allowed the resolution of the translational anisotropy in an isotropic medium. This wavelength-dependent anisotropic light scattering opens up new applications such as to probe the dynamics in complex environments at a single particle level by depolarized DLS. Close to a wall, a strong slowing down of the translational diffusion coefficient has been observed, whereas for rotational diffusion this slowing down was distinct but less pronounced. To study the possible influence of charges on the solid interface on this slowing down, the metal interface has been covered with an electrically neutral layer of poly(methyl methacrylate) (PMMA). Another approach was to exchange CTAB in the GNRs solution for its covalently bound, thiolated analogue 16-mercaptohexadecyl trimethylammonium bromide (MTAB); this reduced the slowing down considerably.

Zusammenfassung

Transportprozesse von anisotropen metallischen Nanopartikeln wie zum Beispiel Gold-Nanostäbchen in komplexen Flüssigkeiten und/oder begrenzten Geometrien spielen eine bedeutende Rolle in einer Vielzahl von biomedizinischen und industriellen Anwendungen. Ein Weg zu einem tiefen, grundlegenden Verständnis von Transportmechanismen ist die Verwendung zweier leistungsstarker Methoden - dynamischer Lichtstreuung (DLS) und resonanzverstärkter Lichtstreuung (REDLS) in der Nähe einer Grenzfläche. In dieser Arbeit wurden nanomolare Suspensionen von Gold-Nanostäbchen, stabilisiert mit Cetyltrimethylammoniumbromid (CTAB), mit DLS sowie in der Nähe einer Grenzfläche mit REDLS untersucht. Mit DLS wurde eine wellenlängenabhängige Verstärkung der anisotropen Streuung beobachtet, welche sich durch die Anregung von longitudinaler Oberflächenplasmonenresonanz ergibt. Die hohe Streuintensität nahe der longitudinalen Oberflächenplasmonenresonanzfrequenz für Stäbchen, welche parallel zum anregenden optischen Feld liegen, erlaubte die Auflösung der translationalen Anisotropie in einem isotropen Medium. Diese wellenlängenabhängige anisotrope Lichtstreuung ermöglicht neue Anwendungen wie etwa die Untersuchung der Dynamik einzelner Partikel in komplexen Umgebungen mittels depolarisierter dynamischer Lichtstreuung. In der Nähe einer Grenzfläche wurde eine starke Verlangsamung der translationalen Diffusion beobachtet. Hingegen zeigte sich für die Rotation zwar eine ausgeprägte aber weniger starke Verlangsamung. Um den möglichen Einfluss von Ladung auf der festen Grenzfläche zu untersuchen, wurde das Metall mit elektrisch neutralem Polymethylmethacrylat (PMMA) beschichtet. In einem weiteren Ansatz wurde das CTAB in der Gold-Nanostäbchen Lösung durch das kovalent gebundene 16-Mercaptohexadecyltrimethylammoniumbromid (MTAB) ersetzt. Daraus ergab sich eine deutlich geringere Verlangsamung.

Contents

Chapter 1

Introduction

1.1 Motivation

Noble metals such as gold and silver with large negative real and small positive imaginary dielectric constants can support surface plasmon polariton resonances, namely, coherent collective oscillations of the electrons in the conduction band excited by electromagnetic radiation [1–3]. In smooth metal films, surface plasmon resonances (SPRs) propagate along the metal/dielectric interface for several micrometers. Normal to the surface, the electromagnetic field decays exponentially over a few hundred nanometers. The optical properties change markedly when gold exists not in the form of an infinitely extending planar surface but of metal nanoparticles (MeNPs) smaller than the wavelength of the light. This fact has been known for centuries, at least since Faraday's investigations on colloidal gold in 1857. For noble MeNPs, localized SPRs oscillate around their surface, and the frequency depends on the size, shape, composition, orientation and local dielectric environment. Thus, the longitudinal and transversal plasmon resonances can be excited at specific wavelengths/frequencies of incident light absorbed by the surface.

These unique and tunable optical properties, with strong field localization in close proximity to the surface of the MeNP, have been utilized in numerous applications: sensing [4, 5], imaging [6], medical diagnostics [7, 8], photothermal therapy [2] (gold

is biologically inert), signal enhancement [1, 9] and optical manipulation [10–12]. The efficient addressability of MeNP photophysical behavior through optical techniques is free of photoblinking (as in quantum dots) and photobleaching (as in fluorophores) while having a much higher molar scattering efficiency ($\sim 5 \times 10^8$ $M^{-1}cm^{-1}$ for 40 nm gold nanoparticles) than the molar emission ($\sim 10^5$ $M^{-1}cm^{-1}$) of fluorescein, a commonly used fluorescent label [2]. The optically excited interactions, which depend on the relative arrangement [13] and the proximity of the MeNP, can be harnessed to realize trapping [8] and functional structures [14, 15] through appropriate assembly [16–18].

In the rapidly developing field of plasmonics, dynamics has received much less attention, despite its ubiquity in nature and its technological importance. Translational and rotational dynamics of MeNPs can capitalize on their enhanced light scattering and the sensitivity of this light scattering to the local environment. For gold nanorods (GNRs), the depolarization ratio, $\rho = I_{VH}/I_{VV}$, of the depolarized light scattering intensity I_{VH} to the polarized scattering intensity I_{VV} was found to exhibit a high resonance maximum of $\rho \approx 0.5$ at a wavelength lower than that of the longitudinal surface plasmon resonance (LSPR) [19, 20]. The frequency dependence of ρ can be theoretically represented by the appropriate choice of the shape parameters and size distribution of the plasmonic nanorods [21]. The strong contribution of the anisotropic scattering to I_{VV} has been utilized to resolve the rotational diffusion component in the polarized quasielastic light scattering spectroscopy of gold nanorods and silver nanoprisms [22, 23]. The latter is recorded in the time domain by Dynamic Light Scattering (DLS) and exhibits a characteristic double-decay relaxation function in contrast to the single translational diffusive decay for dielectric nanoparticles.

Besides the dynamics of the GNRs in bulk solution, translational and rotational dynamics in a confining geometry e.g. close to a solid wall and in complex media e.g. in the presence of the surfactant plays an important role in a wide range of fields. However, previous research focused on other types of nanoparticles other than gold nanorods and e.g. examined a surface-induced anisotropic diffusion close to a wall of polymer nanoparticles, using Evanescent Wave Dynamic Light Scattering (EWDLS) [24, 25]. Using hydrodynamic theory, this anisotropy was attributed to an increase in the hydro-

dynamic drag force near a wall. In another experiment, EWDLS experiments showed unexpected slow near wall dynamics of spherical colloids in a suspension of rods [26]. Furthermore, Ag nanoprism [23] and other optically anisotropic particles [27] were measured in depolarized geometry using EWDLS. These Ag nanoprism exhibited a much less pronounced signal in VH-EWDLS (depolarized) compared to VV (polarized) leading to a not very precise determination of rotational diffusion ($\langle D^r_{\parallel,\perp} \rangle$) [23, 27].

1.2 Aim of the thesis

This thesis started with the aim to understand the transport phenomena of the gold nanorods (GNRs) close to a wall. In order to gain an understanding of the dynamics of the GNRs, first it is necessary to understand the dynamics of the GNRs in bulk solution.

Up to now, few studies have addressed the dynamics of the plasmonic GNRs with strong anisotropic VH scattering signal in bulk solution. Solid proof, however, of LSPR-enhanced dynamic depolarized light scattering and its effects on the dynamics from single-particle dynamic light scattering was still missing. Furthermore, the dynamics of GNRs has not been investigated close to a wall as well as the effect of the surfactant in the GNRs solution on the near wall dynamics. Therefore, the present work reveals the experimental results of the dynamics of the GNRs in bulk solution using Dynamic Light Scattering (DLS) and close to a wall using Resonance Enhanced Dynamic Light Scattering (REDLS) [28, 29]. An advantage of this technique as compared to EWDLS is an enhanced sensitivity and signal-to-noise ratio. This allows studying the translational and rotational dynamics of nanoparticles close to a wall.

1.3 Outline

This thesis is organized as follows:

In Chapter 2, I will briefly review the plasmon modes on planar metal-dielectric interfaces (*surface plasmons*) and in metal nanoparticles (*particle plasmons*) followed by the

theory of Dynamic Light Scattering (DLS).

Chapter 3 presents sample preparation and the experimental methods used for the studies presented in this work. The most important ones are Dynamic Light Scattering (DLS), Surface Plasmon Resonance (SPR), Resonance Enhanced Dynamic Light Scattering (REDLS) and Waveguide Enhanced Dynamic Light Scattering (WEDLS).

Chapter 4 presents results of the experiments. In Section 4.1, first I present the results from the wavelength-dependent depolarized DLS of GNRs. Second, I demonstrate the size selectivity of this technique. Third, I resolve the translational diffusion anisotropy in an otherwise isotropic environment near the LSPR frequency. Sorting plasmonic nanoparticles according to their size and shape can help the development of polarized microscopy techniques, whereas the high sensitivity of depolarized DLS at a single-particle level can yield new insights into the dynamics in complex environments. In Section 4.2, I present the dynamics of GNRs stabilized with MTAB close to a wall using REDLS. Section 4.3 addresses the effect of the surfactant CTAB on the diffusion and rotation of GNRs in water close to a charged solid (gold) and neutral (PMMA) wall using REDLS and WEDLS. Section 4.4 comprises the dynamics of spherical silica coated GNRs (SiO_2@GNRs) close to a wall and compares the results with GNRs and silica particles of the same size.

Chapter 2

Theoretical background

The focus of this work lies on the experimental study of dynamics of gold nanorods (GNRs) in bulk solution and close to a wall (gold layer). In order to gain an understanding of optical properties of metallic planes and nanoparticles, I will briefly introduce the concept of *plasmon* in metallic planes (*surface plasmon polariton (SPP)*) and metal nanoparticles (*particle plasmon*). I will explain properties as well as excitation methods. For more details the reader is referred to standard textbooks on plasmons by Novotny and Hecht (2006) or Sarid and Challener (2010). The second part reviews the theoretical background on dynamic light scattering measurements of nanoparticles in bulk solution and close to a wall including relaxation behavior and data analyzing. Further details can be found in textbooks such as Berne and Pecora (2000) or Schärtl (2006).

2.1 Surface plasmons on metallic planes

Collective electronic excitations at metal surfaces are well known to play a key role in a wide spectrum of science, ranging from physics and material science to biology. These collective oscillations of the quasi-free electrons in metals are called *plasmons*. Historically, the surface plasmon modes were studied as early as the beginning of the 20^{th} century by Zenneck and Sommerfeld [30, 31]. Ritchie was the first to use the term *surface plasmons* when in 1957 he extended the work of Pines and Bohm [32] to include

the interaction of the plasma oscillations with the metal surface [33]. The existence of plasmons is characteristic for the interaction of metal nanostructures with light at optical frequencies. In this section, I will briefly describe the properties and excitation of SPP.

2.1.1 Properties of surface plasmon polaritons

Surface plasmons are coupled oscillations of electron density and the electromagnetic field which can also be called *surface plasmon polariton (SPP)*. The properties of the SPP at a flat metal-dielectric interface can be obtained from the dielectric constant of two media ε_1 and ε_2 ($\varepsilon_1 = \varepsilon^{'}{}_1 + i\varepsilon^{''}{}_1$) and the complex parallel wave vector $k_{\mathrm{x}} = k^{'}{}_{\mathrm{x}} + ik^{''}{}_{\mathrm{x}}$ which defines a wave propagating along the metal-dielectric interface. The imaginary part $k^{''}{}_{\mathrm{x}}$ denotes the damping of the SPP by propagating along the interface while the real part $k^{'}{}_{\mathrm{x}}$ determines the SPP wavelength. The relation between the wave vector along the propagating direction and the angular frequency ω is given by [34]

$$k^{2}{}_{\mathrm{x}} = \frac{\varepsilon_1 \varepsilon_2}{\varepsilon_1 + \varepsilon_2} k^2 = \frac{\varepsilon_1 \varepsilon_2}{\varepsilon_1 + \varepsilon_2} \frac{\omega^2}{c^2}. \tag{2.1}$$

Using the equation 2.1 the real and imaginary parts of k_{x} can be written as

$$k^{'}{}_{\mathrm{x}} \approx \sqrt{\frac{\varepsilon^{'}{}_1 \varepsilon_2}{\varepsilon^{'}{}_1 + \varepsilon_2}} \frac{\omega}{c}, \tag{2.2}$$

$$k^{''}{}_{\mathrm{x}} \approx \sqrt{\frac{\varepsilon^{'}{}_1 \varepsilon_2}{\varepsilon^{'}{}_1 + \varepsilon_2}} \frac{\varepsilon^{''}{}_1 \varepsilon_2}{2\varepsilon^{'}{}_1 (\varepsilon^{'}{}_1 + \varepsilon_2)} \frac{\omega}{c}. \tag{2.3}$$

The SPP wavelength can be obtained by

$$\lambda_{\mathrm{SPP}} = \frac{2\pi}{k^{'}{}_{\mathrm{x}}} \approx \sqrt{\frac{\varepsilon^{'}{}_1 + \varepsilon_2}{\varepsilon^{'}{}_1 \varepsilon_2}} \lambda, \tag{2.4}$$

where λ is the wavelength in vacuum. The plasmon wavelength is always shorter than the wavelength in the transparent medium. The electrical field of a SPP decays exponentially with distance from the interface. The decay into the metal is much shorter

than that into the dielectric [34].

Figure 2.1 shows a system that is composed of an electromagnetic wave in the dielectric medium and an oscillating electron plasma in the metal, where both modes have an exponentially decaying evanescent character.

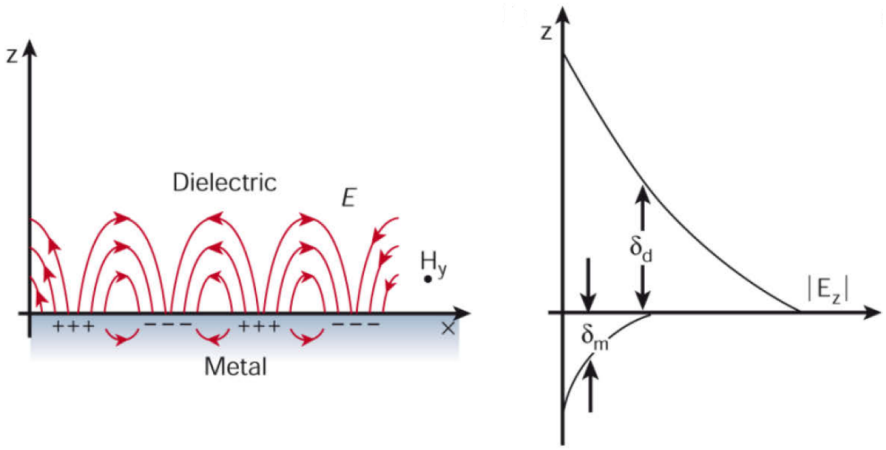

Figure 2.1: Left: composed character of SPPs at the interface between dielectric and metal. Right: evanescent fields in the two half spaces [35].

2.1.2 Excitation of surface plasmon polaritons

Surface plasmons can be excited by both electrons and photons. In the case of an electron, the excitation can be created by firing electrons into the bulk of a metal. As the electrons scatter, energy is transferred into the bulk plasma. The component of the scattering vector parallel to the surface results in the formation of a surface plasmon [36].

Coupling of photons into SPP can be achieved by using a coupling medium such as a prism or grating to match the photon and surface plasmon wave vectors. This can be realized experimentally by placing the prism against a thin metal film in the Kretschmann configuration [37] or very close to a metal surface in the Otto configuration [38] (Figure 2.2). In the Otto configuration, there has to be a small gap between the dielectric and the metal surface. Therefore, this configuration is experimentally inconvenient because it is difficult to control the tiny air gap between the glass and the metal surface. In contrast to Otto configuration, the Kretschmann configuration can be used by depositing

a thin metal film on top of a glass prism. If the metal film is too thick the SPP can no longer be efficiently excited due to absorption in the metal. If the metal film is too thin the SPP will be strongly damped because of radiation damping into the glass. In this work the Kretschmann configuration has been used.

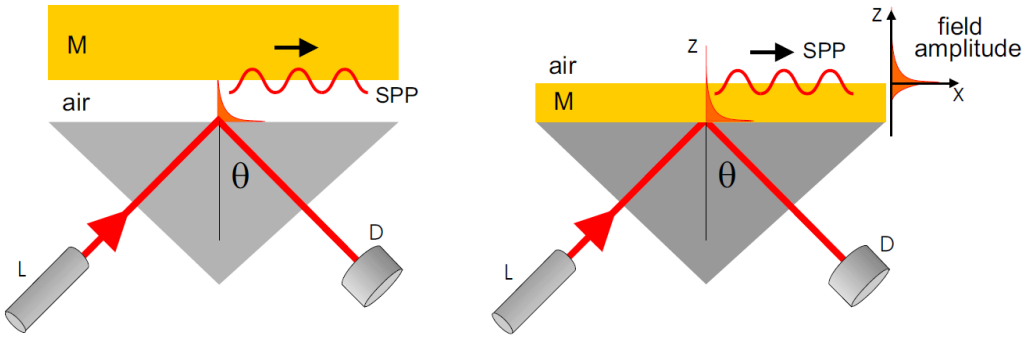

Figure 2.2: Experimental configurations to excite the surface plasmon polariton (SPP) in Otto configuration (left) and Kretschmann configuration (right). The metal layer is sketched in yellow. L: laser, D: detector, M: metal layer [34].

2.2 Particle plasmons in metal nanoparticles

The particle plasmon resonance of tiny gold and silver particles with diameters on the nanometer scale show very bright colors. These bright colors have fascinated people for many centuries. Famous examples are the Lycurgus cup (Roman empire, 4^{th} century AD), which has a green color when observing in reflecting light, while it shines in red in transmitting light conditions, and church window glasses (Figure 2.3).

Plasmon modes in metal nanoparticles - *particle plasmons* or *localized surface plasmon resonance* are charge density oscillations confined to metallic nanoparticles and metallic nanostructures. It is one of the characteristic optical properties of noble metal nanoparticles, which arises when the incident photon frequency is resonant with the collective oscillation of the conduction electrons in the metal nanoparticles. The localized surface plasmon resonance is highly sensitive to the size, size distribution and shape of the nanoparticles as well as to the environments which surround them [39, 40]. Figure 2.4 shows how this effect can be pictured in a very simple way. The electric field of an incoming light wave induces polarization of the free electrons with respect to the much

Figure 2.3: Left: Lycurgus cup, 4^{th} century AD. Right: color windows of the St. Stephan's Church in Mainz. The colors originates from metal nanoparticles embedded in the glass.

heavier ionic core of a spherical nanoparticle. The net charge difference occurs at the nanoparticle surface which in turn acts as a restoring force.

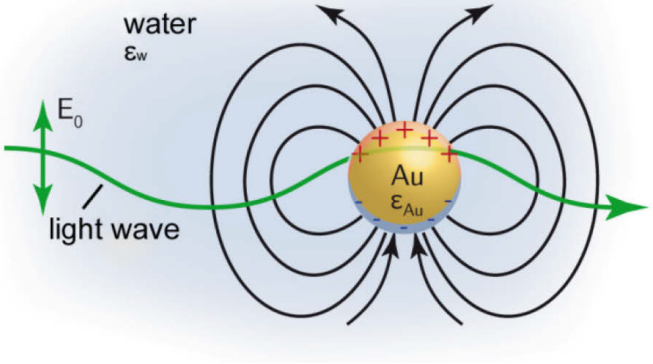

Figure 2.4: Simple model showing the excitation of a particle plasmon in a metal gold particle by an external oscillation field [41].

Experimentally, the localized surface plasmon resonance has been employed for chemical and biological sensors, surface enhanced raman spectroscopy (SERS), biomedical applications, nonlinear optical devices and optical tweezers [7, 42–47]. Theoretically, a variety of techniques have been developed to study the interaction of light with small particles. For spherical particles in a homogeneous medium an analytical solution exists. This theory has been calculated by Mie and is called *Mie theory*. However, for general particle shapes there is no analytical solution. Therefore, a variety of numerical methods have been developed to model different particle shapes such as frequency domain, finite element, finite difference time domain (FDTD), discrete dipole, multiple multipole

methods and transition matrix (T-matrix) method. In this thesis, the T-matrix method has been used to quantitatively describe the absorption and scattering cross section of GNRs. In the following, I will briefly review the theory of the T-matrix method, plasmon resonances of a small spherical particle and plasmon resonances of non-spherical particles.

2.2.1 Transition matrix (T-matrix) method

The T-matrix method (also known as null field method or extended boundary condition method (EBCM)) is the best known of the mentioned theoretical methods above because it is applicable to any kind of shape of the particles and fast computer codes are available [48,49]. The T-matrix method has originally been developed by Waterman in a series of papers [50–52]. It is mainly applied to scattering of non-spherical particles and is based on the linearity of Maxwell's equations.

In the T-Matrix method, both incident $E_{\mathrm{inc}}(r)$ and scattered $E_{\mathrm{sca}}(r)$ electric fields are expanded in a series of vector spherical harmonics M_{mn} and N_{mn} [53]. They are the fundamental solutions of the vector Helmholtz equation [54, 55] and can be generated from the scalar fundamental solutions in spherical coordinates, the spherical Bessel functions [56] of the first kind and the spherical Hankel functions [57] and are given by

$$\begin{aligned} E_{\mathrm{inc}}(r) &= \sum_{n=1}^{\infty}\sum_{m=-n}^{n}\left[a_{\mathrm{mn}}R_{\mathrm{g}}M_{\mathrm{mn}}(kr)+b_{\mathrm{mn}}R_{\mathrm{g}}N_{\mathrm{mn}}(kr)\right], \\ E_{\mathrm{sca}}(r) &= \sum_{n=1}^{\infty}\sum_{m=-n}^{n}\left[p_{\mathrm{mn}}M_{\mathrm{mn}}(kr)+q_{\mathrm{mn}}N_{\mathrm{mn}}(kr)\right] \qquad r > r^{'}. \end{aligned} \tag{2.5}$$

k is the wave number in the surrounding medium and $r^{'}$ is the radius of the smallest circumscribing sphere of the scatterer centered at the origin of the laboratory coordinate system. The functions R_gM_{mn} and R_gN_{mn} are regular (finite) at the origin, while the use of the outgoing functions M_{mn} and N_{mn} in the $E_{\mathrm{sca}}(r)$ function of the equation 2.5 ensures that the scattered field satisfies the so-called radiation condition at infinity.

The linearity of Maxwell's equations enables to relate both scattered (p_{mn}, q_{mn}) and incident (a_{mn}, b_{mn}) field coefficients by means of a T-matrix [58]:

$$
\begin{aligned}
p_{mn} &= \sum_{n'=1}^{\infty} \sum_{m'=-n'}^{n'} [T^{11}_{mnm'n'} a_{m'n'} + T^{12}_{mnm'n'} b_{m'n'}], \\
q_{mn} &= \sum_{n'=1}^{\infty} \sum_{m'=-n'}^{n'} [T^{21}_{mnm'n'} a_{m'n'} + T^{22}_{mnm'n'} b_{\mathrm{m'n'}}].
\end{aligned}
\tag{2.6}
$$

The T-matrix elements are independent of the nature of the incident or scattered fields. They depend on the particle's size, shape, composition and orientation and can be calculated in the so-called natural reference frame (z axis along the revolution axis) and then be averaged for all incidence and scattering directions. The T-matrix can be written in compact notation as [58]

$$
T = -B \times A^{-1} = - \begin{pmatrix} B_{11} & B_{12} \\ B_{21} & B_{22} \end{pmatrix} \times \begin{pmatrix} A_{11} & A_{12} \\ A_{21} & A_{22} \end{pmatrix}^{-1} = \begin{pmatrix} T_{11} & T_{12} \\ T_{21} & T_{22} \end{pmatrix} \tag{2.7}
$$

Expressions for the calculation of the A and B matrix elements are detailed in the references [59], [48] and [60].

Given a two-layered particle with refractive indices n_1 (core) and n_2 (shell), the T-matrix can be derived as [58, 61]

$$
T = -B \times A^{-1} = - \left[B_2 + BB_2 \times (-B_1 \times A_1^{-1}) \right] \times \left[A_2 + AA_2 \times (-B_1 \times A_1^{-1}) \right]^{-1}. \tag{2.8}
$$

A_2 and B_2 are calculated by setting refractive index as n_2 for inner and as 1 for outer, and an incident wavelength as k_0 whereas matrices AA_2 and BB_2 are calculated in the same way as A_2, B_2, except that the Bessel functions of the first kind with argument kr are replaced by Hankel functions with the same argument. The T-matrix for a particle with refractive index as n_1/n_2 for inner, as 1 for outer and incident radiation wave number as $k_0 n_2$ can be written as $-B_1 \times A_1^{-1}$ [58]. The T-matrix elements can be used to calculate any light scattering of interest, either cross sections or scattering matrix elements. For example, expressions for extinction and scattering cross sections are [58]

$$\sigma_{ext} = \frac{2\pi}{k^2} Re \sum_{n=1}^{\infty} \sum_{m=-n}^{n} [T^{11}_{mnn'} + T^{22}_{mnn'}],$$
$$\sigma_{sca} = \frac{2\pi}{k^2} \sum_{i,j=1}^{2} \sum_{n=1}^{\infty} \sum_{n'=1}^{\infty} \sum_{m=0}^{min(n,n')} (2 - \delta_{m0}) |T^{ij}_{mnn'}|^2. \tag{2.9}$$

In Chapter 4.1, the T-matrix method has been used to describe the absorption and scattering cross section of GNRs as well as the polarized I_{VV}, depolarized I_{VH} scattering intensities, and depolarization ratio I_{VH}/I_{VV} as functions of the wavelength of the probing light. In this notation, V and H mean polarization vertically and horizontally, respectively, with respect to the scattering plane.

2.2.2 Plasmon resonances of small spherical particles

Since I have worked in this thesis with gold nanoparticles and gold nanorods (GNRs), I will briefly review the theory of plasmon resonances of spherical and non-spherical particles.

As described in Section 2.2, localized surface plasmons (also known as surface plasmons on metal nanoparticles) are non-propagating plasmon excitations on metallic nanostructures. For small isolated metal particles with sizes in the range of the penetration depth of an electromagnetic field, the clear distinction between surface and bulk plasmon vanishes. An external field can penetrate into the volume and shift the conduction electrons with respect to the ion lattice. The coherently shifted electrons together with the restoring field represent an oscillator, whose behavior is defined by the effective electron mass, charge density and geometry of the particle.

The plasmon resonance for a small spherical particle of radius a in a uniform static electric field $E_{in} = E_0 e_z$ can be expressed with the Laplace equation ($\Delta^2\Phi = 0$) in spherical coordinates (r, θ, φ) as

$$\frac{1}{r^2 \sin\theta} \left[\sin\theta \frac{\partial}{\partial r} \left(r^2 \frac{\partial}{\partial r} \right) + \frac{\partial}{\partial \theta} \left(\sin\theta \frac{\partial}{\partial \theta} \right) + \frac{1}{\sin\theta} \frac{\partial^2}{\partial \varphi^2} \right] \Phi(r, \theta, \varphi) = 0. \tag{2.10}$$

The surrounding medium is isotropic and non-absorbing with dielectric constant ε_{d}. The

optical properties of the metal sphere are described by a complex dielectric constant ε_s. From the solution of the Laplace equation $\Delta^2\Phi = 0$ one can obtain the electric field $E = -\nabla\Phi$. The electric field can then be expressed as

$$E_s = \frac{3\varepsilon_\mathrm{d}}{\varepsilon_s + 2\varepsilon_\mathrm{d}} E_0 \tag{2.11}$$

$$E_d = E_0 + \frac{1}{4\pi\varepsilon_0\varepsilon_d}\frac{3n(n\cdot P) - P}{r^3}. \tag{2.12}$$

n $(= r/\mathrm{r})$ is here the unit vector and P the dipole moment that is induced in the sphere by the external field. From the relation $P = \varepsilon_0\varepsilon_\mathrm{d}\alpha E_0$, the polarizability α is defined as [62]

$$\alpha = 4\pi\varepsilon_0 a^3 \frac{\varepsilon_\mathrm{s} - \varepsilon_\mathrm{d}}{\varepsilon_\mathrm{s} + 2\varepsilon_\mathrm{d}}. \tag{2.13}$$

The scattering and absorption cross sections are then [62, 63]:

$$\sigma_{scatt} = \frac{k^4}{6\pi\varepsilon_0^2}|\alpha|^2 = \frac{8\pi}{3}k^4a^6\left|\frac{\varepsilon_\mathrm{s} - \varepsilon_\mathrm{d}}{\varepsilon_\mathrm{s} + 2\varepsilon_\mathrm{d}}\right|^2 \tag{2.14}$$

$$\sigma_{abs} = \frac{k}{\varepsilon_0}\,\mathrm{Im}(\alpha) = 4\pi k a^3\left(\frac{\varepsilon_\mathrm{s} - \varepsilon_\mathrm{d}}{\varepsilon_\mathrm{s} + 2\varepsilon_\mathrm{d}}\right) \tag{2.15}$$

with $k = 2\pi/\lambda$. The scattering cross section is the total power of the scattered light normalized by the power per unit area of the incident plane wave and has the dimension of the area. Similarly, the absorption cross-section is the ratio of the total power absorbed by a particle to the power per unit area of the incident plane wave [64].

2.2.3 Plasmon resonances of non-spherical particles

The polarizability for a non-spherical particles depends on the orientation of the particle to the incident field. To obtain the plasmon resonances of non-spherical particles one can model them as prolate spheroids and than apply the quasi-static approximation. The polarizability α is given by [63]

$$\alpha = V\varepsilon_0 \frac{\varepsilon_s - \varepsilon_d}{L_i\varepsilon_s + (1 - L_i)\varepsilon_d} \tag{2.16}$$

with V being the volume of the spheroid and L_i the geometrical factors related to the aspect ratio and describes the longitudinal and transverse plasmon resonances of the spheroid.

Of particular interest are ellipsoidal particles which are characterized by the three semi-axes of length a, b, c with $a \geq b \geq c$. Those cases where two of these axes have identical lengths are called *prolate* ($a > b = c$) and *oblate* ($a = b > c$) (Figure 2.5).

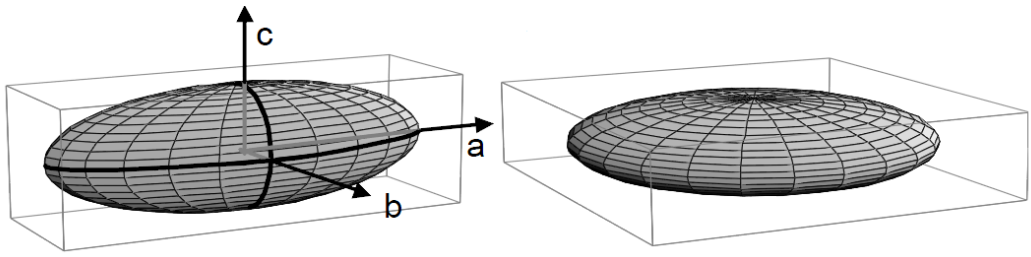

Figure 2.5: Schematic representation of prolate spheroid (left) and oblate spheroid (right) [65].

For a sphere $L_i = 1$ and therefore the equation 2.16 reduces to equation 2.13. The geometrical factor L_i for a prolate particle along its long axis is given by:

$$L_i = \left(\frac{1 - e^2}{e^2}\right)\left[\frac{1}{2e} ln(\frac{1 + e}{1 - e}) - 1\right], \qquad e^2 = 1 - \frac{b^2}{a^2}. \tag{2.17}$$

2.3 Evanescent waves

Evanescent means *tending to vanish* and this refers to the behavior of the evanescent wave. Because the intensity of evanescent waves decays exponentially with distance from the interface at which they are formed. The electric field of an evanescent wave can be described by wave vectors $\vec{k_x}$ and $\vec{k_z}$. If the incident light is s- or p-polarized, the electric field of the evanescent wave is given by [66]

$$\vec{E}(y,t) = \vec{E_0}(y) \cdot e^{i\omega t} \cdot e^{-i\vec{k_x}x} \cdot e^{-i\vec{k_z}z} \tag{2.18}$$

and

$$\vec{E}(x,z,t) = \vec{E_0}(x,z) \cdot e^{i\omega t} \cdot e^{-i\vec{k_x}x} \cdot e^{-i\vec{k_z}z}, \tag{2.19}$$

respectively. Here ω is equal to $\omega = 2\pi\nu$ with ν as the frequency of the light. The wave vector in z-direction for all evanescent waves is a complex number and can be calculated from

$$\vec{k_z} = \frac{1}{i\xi} \cdot \frac{\vec{e_z}}{|\vec{e_z}|}. \tag{2.20}$$

ξ denotes the penetration depth of the evanescent wave and $\vec{e_z}$ is the unit vector. In this work, the evanescent wave is generated with the help of *Total Internal Reflection (TIR)* method.

2.3.1 Total internal reflection (TIR)

When an electromagnetic wave (light) in a dielectric medium of index n_1 is incident upon an interface of a different dielectric material of a lower optical density n_2, at an angle θ_1 greater than the critical angle θ_c, total internal reflection (TIR) occurs and an evanescent wave is formed (Figure 2.6(b)). If the incident angle $\theta_1 < \theta_c$, then part of the incident light is transmitted and part is reflected (Figure 2.6(a)). This phenomenon is called refraction and can be determined by the *Snell's law*. The Snell's law predicts the refracted angle θ_2 by [67]

$$n_1 \sin(\theta_1) = n_2 \sin(\theta_2). \tag{2.21}$$

The angle of total reflection can be then calculated from equation 2.21

$$\theta_c = \sin^{-1}\left(\frac{n_2}{n_1}\right). \tag{2.22}$$

The solution of Maxwell's equations predicts the existence of an electromagnetic field in the less dense medium with intensity decaying exponentially away from the interface. The result is an evanescent wave. In this case the wave vector of the evanescent wave

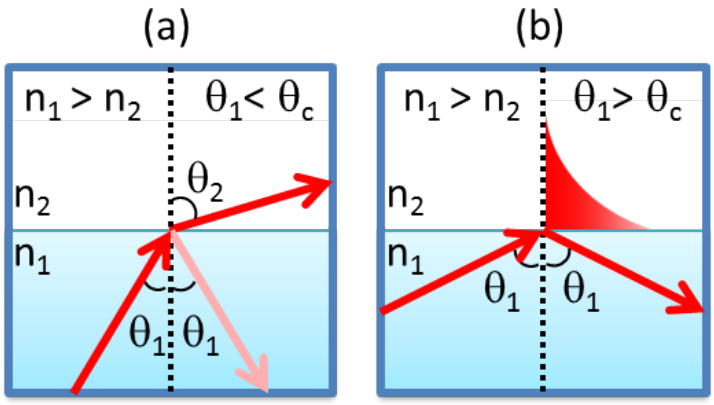

Figure 2.6: Refraction of light at the interface between two media, including total internal reflection. (a): If the incidence angle $\theta_1 < \theta_c$, a part of the beam is transmitted and a part reflected. (b): If $\theta_1 > \theta_c$, no beam is transmitted, total internal reflection will happen and an evanescent wave appears.

of the total internal reflection and the penetration depth are given by [68]

$$k_x^{TIR} = \frac{\omega}{c} \cdot n_1 \cdot \sin(\theta_1) \tag{2.23}$$

and

$$\xi^{TIR} = \frac{c}{\omega}\left[n_2\sqrt{\left(\frac{n_1}{n_2}\right)^2 \cdot \sin(\theta) - 1}\right]^{-1}. \tag{2.24}$$

2.4 Dynamic light scattering (DLS)

For the case of non-interacting particle in solution, Dynamic Light Scattering (DLS) - also called Photon Correlation Spectroscopy (PCS) or Quasi-Elastic Light Scattering (QELS) - is based on the fact that the Brownian motion of particles leads to fluctuations in the particle density and therefore to variations in the scattered electric field. The first developed theory was given by Smoluchowski in 1908 and by Einstein in 1910. They called this theory *fluctuation theory of light scattering* which explained that the thermal fluctuations of a continuous medium give rise to local inhomogeneities and therefore to density and concentration fluctuations.

2.4.1 Time intensity autocorrelation function

To quantitatively analyze the particle mobility by light scattering, the scattering intensity fluctuations in terms of correlation functions can be used and describe how strong two signals at different times are correlated. In colloidal systems one can then determine the dynamics of the system, e.g. if the sample is in an arrested state or still fluid.
The field autocorrelation function is determined as follows:

$$g_1[q,t] = \frac{\langle E[q,t']E^*[q,t'+t]\rangle}{\langle E[q,t']E^*[q,t']\rangle} \tag{2.25}$$

where $E[q,t']$ and $E[q,t'+t]$ are the scattered electric fields at time t' and $t'+t$, respectively.
As the electric field is not accessible to the experiment, one has to consider the intensity autocorrelation function. The intensity autocorrelation function is determined as follows [69, 70]:

$$g_2[q,t] = \frac{\langle I[q,t']I[q,t'+t]\rangle}{\langle I[q,t']\rangle^2} = \frac{\lim_{T\to\infty}\ \frac{1}{2T}\int_{-T}^{T} dt' I[q,t']I[q,t'+t]}{\langle I[q,t']\rangle^2}. \tag{2.26}$$

$\langle I[q,t']\rangle$ and T are the average time intensity and the total experiment time, respectively. q is the scattering vector with $\vec{q} = \vec{k_i} - \vec{k_s}$. $\vec{k_i}$ and $\vec{k_s}$ denote the wave vector of the incident and the scattered light. The value of $\vec{q}$ is given by

$$|\vec{q}| = \frac{4\pi n}{\lambda}\sin\left(\frac{\theta}{2}\right) \tag{2.27}$$

with θ being the angle under which the scattered light is detected.
The field and the intensity autocorrelation functions are connected by the *Siegert* relation [69]:

$$g_2[q,t] = 1 + f\cdot g_1^2[q,t] \tag{2.28}$$

with f being the contrast factor.
There are two types of detection in DLS experiment - *homodyne* and *heterodyne* de-

tection. In the heterodyne measurement, a portion of the incident light is diverted and then mixed with the scattered light. In heterodyne detection it is important that both coherent beams are in phase in order to have a successful positive interference. In the homodyne detection only the scattered light from the sample displays on the detector. In Figure 2.7 the intensity and field auto correlation function as well as time intensity fluctuation as a function of time in the homodyne detection with the DLS experiment is shown.

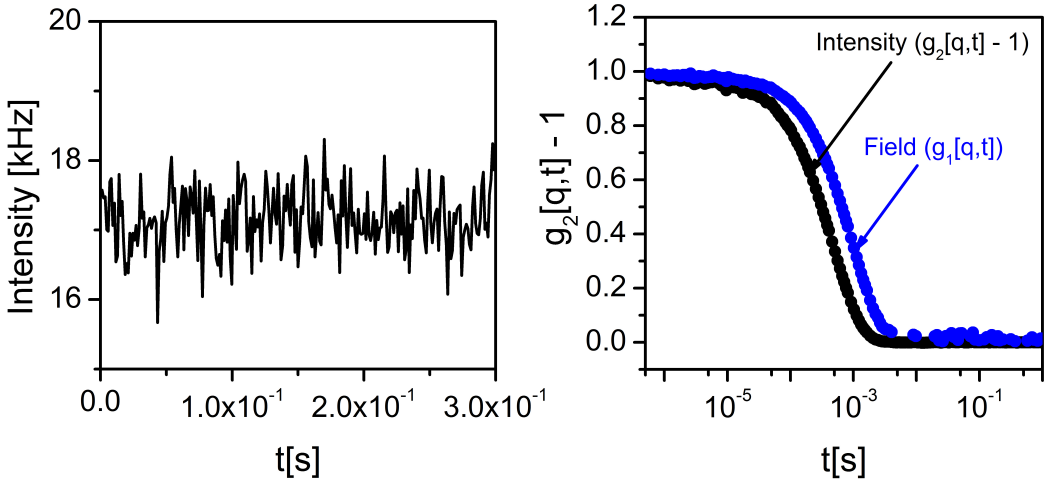

Figure 2.7: Intensity and field autocorrelation function (right) and time intensity fluctuation (left) during a DLS experiment for polystyrene latex particle with $R_h = 101.4 \pm 4$ nm and a concentration of c = 0.47 g/l at a scattering angle $\theta = 90°$.

2.4.2 Data analysis

In standard DLS experiments the intensity auto correlation function, $g_2[q,t] = 1 + f \cdot g_1^2[q,t]$ is related to the physical relevant field autocorrelation function $g_1[q,t]$ via the Siegert relation [69]. $g_1[q,t]$ can be obtained directly by performing the experiment in the heterodyne scattering regime. Here, f is the contrast factor, t the delay or lag time and q the absolute value of the scattering vector, which is defined as $q = 4\pi n/\lambda \sin(\theta/2)$, with n as the refractive index of the medium, λ the wavelength of the laser, and θ the scattering angle [69]. In an ideal system of monodisperse particles with free diffusion, $g_1[q,t]$ decays exponentially $g_1[q,t] = a \cdot exp(-\Gamma t)$ with decay rate Γ and contrast or

amplitude of the decay a related to the scattered or so-called total intensity (I_{tot}) [69,70]. In heterodyne experiments, I_{tot}, the scattered intensity stemming from the particle, can be calculated as the product of the experimentally obtained amplitude or contrast and the count rate measured in the experiment.

In reality, one has always some size polydispersity of the particles leading to a distribution of relaxation times. This can be described, e.g. by the phenomenological Kohlrausch-Williams-Watts (KWW) function as

$$g_1[q,t] = a \cdot exp\{(-\Gamma t)^{\beta}\}, \Gamma = \frac{1}{\tau} \tag{2.29}$$

with a being the amplitude of the decay, τ the relaxation or characteristic time, Γ the relaxation rate, and β the stretching parameter. From these parameters the weighted *mean relaxation time* or *mean relaxation rate* is calculated [71,72], which is the physical relevant parameter:

$$\langle\Gamma\rangle = \beta\Gamma/Gamma[\frac{1}{\beta}] \tag{2.30}$$

with *Gamma* the gamma function. In Chapter 4, I call $C_{VV}[q,t]$ or $C_{VH}[q,t]$ the measured field autocorrelation functions (VV: polarization axis of incident and scattered light is vertical with respect to the scattering plane, VH: polarization of the scattered light is horizontal with respect to the scattering plane).

For a dilute solution of monodisperse spherical nanoparticles in DLS the translational diffusion coefficient D_0 is directly obtained from $\Gamma = \Gamma_{VV} = D_0 q^2$ ($I_{VV} = I_{iso} + \kappa I_{VH}$ with $I_{VH} << I_{iso}$ and thus $I_{VV} \approx I_{iso}$). For anisotropic monodisperse particles, $I_{VH}[q,t]$ is experimentally available via the square of the polarizability tensor reflecting translational and rotational motion [73]. The uncoupled dynamics are given by [74]

$$C_{VH}[q,t] = a_{VH} exp\{-(\Gamma_{VH} t)^{\beta_{VH}}\} \tag{2.31}$$

and

$$\Gamma_{VH} = 6D_R + D_0 q^2 \tag{2.32}$$

with $D_0 = (D_{\parallel} + 2D_{\perp})/3$ being the average of the translational diffusion coefficients

along and normal to the rod axis. In the case of very small rods, $6D_R >> D_0q^2$, thus Γ_{VH} becomes nearly q-independent [75]. In the VV geometry both I_{iso} and I_{VH} contributions are included in the scattering intensity. Normally, in experiments studying particles in solution, the depolarized I_{VH} part is very small compared to the I_{iso} part and is neglected in the analysis. But for noble metal nanoparticles (MeNP), I_{VH} is enhanced and

$$C_{VV}[q,t] = a_f exp\{-(\Gamma_f t)^{\beta_f}\} + a_s exp\{-(\Gamma_s t)^{\beta_s}\} \tag{2.33}$$

and

$$\Gamma_s = D_0q^2, \quad \Gamma_f = \Gamma_{VH} \tag{2.34}$$

becomes bimodal [22,23,74], with a as fast and slow process characterized by amplitudes a_f and $a_s = (1 - a_f)$. The fast component can be related to the VH results and the slow to the isotropic scattering [75], therefore: $\Gamma_f = \Gamma_{VH}$, $\Gamma_s = \Gamma_{iso}$.

Another way of describing the correlation function is the Cumulant analysis (also called initial slope analysis) [76–78],

$$\ln(C[q,t]) = -\Gamma_c t + \frac{\mu}{2!}t^2 - ...., \tag{2.35}$$

where Γ_c is the initial decay rate, $C[q,t]$ is the normalized field autocorrelation function $g_1[q,t]$ and μ is the variance of the distribution. Note that for monodisperse particles in bulk solution $\Gamma_c = D_0q^2$. From the physics point of view, only the Cumulant method can be derived mathematically, as was done for the case of evanescent light scattering [79, 80]. But for autocorrelation functions assembled from several relaxation functions the Cumulant or initial decay method is difficult to handle. Therefore, I stick to one phenomenological method - the KWW function introduced above - in order to compare the results from VV and VH in bulk with DLS as well as close to a wall with REDLS/WEDLS.

An alternative method for analyzing the autocorrelation function can be achieved through an inverse Laplace-transformation (ITS) known as CONTIN or regularization

method developed by Steven Provencher [81, 82]. It is useful for heterodisperse, polydisperse and multimodal systems that cannot be resolved with the Cumulant method. The CONTIN method assumes that the distribution is an arbitrary but smooth function and seeks a non-negative distribution producing the fit to the experimental data. The quantity χ can be described as [83]

$$\chi^2 = \sum_i (1/\sigma^2)[G(r) - (KA)_i]^2, \tag{2.36}$$

with K being a matrix having elements $K[r_i, s_j], i = 1, ..., N, j = 1, ..., M$, σ a standard error, G(r) the variable accessible experimentally (autocorrelation function), A a function characteristic for the system under investigation which can be expressed theoretically and $K[r, s]$ a specific function for the experimental method e.g. $K[r, s] = exp(-r.s)$ in DLS experiments. The CONTIN method adds an extra parameter α into the equation above which is given by [83]

$$\chi^2(\alpha) = \sum_i (1/\sigma^2)[G(r) - (KA)_i]^2 + \alpha \|\ell A\|. \tag{2.37}$$

α is called the regularization parameter and ℓ is an operator which is usually taken to be the second derivative. The value of α controls the strength of the regularization. If $\alpha = 0$ or very small the solution will be equivalent to a non-negative least-squares method. Higher α values lead to solutions with many peaks. CONTIN generally presents a progression of solutions with increasing α.

The choice of the parameter is one of the most difficult and important parts of this method. One has to be careful at interpreting the CONTIN output and should not accept automatically the chosen solution especially if the solution does not meet the expectation. It is a good idea to look at solutions that are slightly more and less penalized to see whether a particular peak is robust to small changes in α. If true, the chances are that it is real.

There is an ongoing discussion which model is best to fit light scattering data. As pointed out above, from the physics point of view only the Cumulant or initial decay method is

justified. For practical reasons as in this work one can resort to KWW functions or the regularized inverse Laplace methods as CONTIN. Nevertheless, for some of my data I did comparisons of the KWW, Cumulant and CONTIN methods to give the reader a feeling of how much the one or other fit might disagree or systematically shift e.g. the points in a plot vs. scattering vector or the cube of the scattering vector. In the inset to Figure 2.8 the results for 60/25 nm MTAB stabilized GNRs (MTAB-GNRs) measured by DLS (lines for the relaxation times from KWW and Cumulant) are compared which displays the distribution of relaxation times from a CONTIN fit.

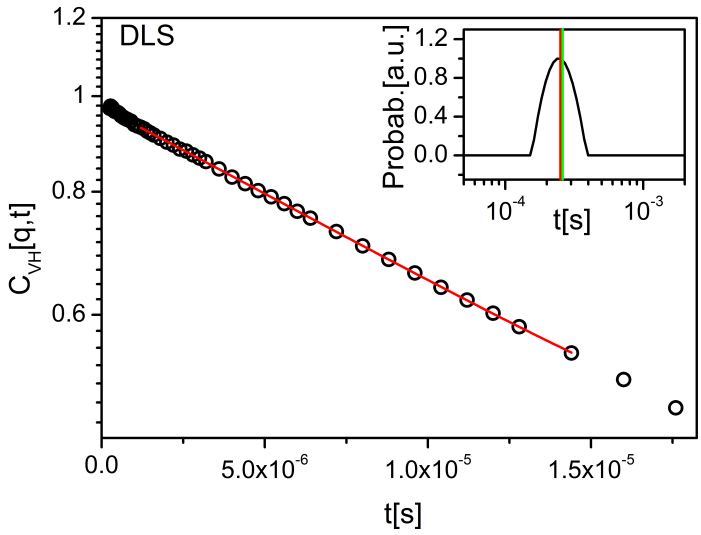

Figure 2.8: Comparison of results from Cumulant (main plot), CONTIN and KWW method (inset) for 60/25 nm MTAB-GNRs at a scattering angle of 90° (q = 0.019 nm^{-1}) in VH geometry. Main plot: results from Cumulant fit. Inset: results from KWW with a barely visible red line and the Cumulant with a green line coincident within the experimental error with the maximum of the CONTIN distribution of relaxation times for a bulk DLS experiment.

Another example is the fit of a REDLS correlation function in the VV geometry for 60/25 nm CTAB stabilized GNRs (CTAB-GNRs). In Figure 2.9(a) the CONTIN distribution of relaxation times is compared with the results from the KWW fit (red line) for 60/25 nm CTAB-GNRs whereas Figure 2.9(b) indicates that due to the not unambiguous fit from Cumulant this method was not used and only KWW and CONTIN are compared. In VH geometry the fit of a REDLS correlation function with all three

methods are compared (Figure 2.10). Here the CONTIN distribution of relaxation times (black curve) is compared with the results from KWW fit (red line) and Cumulant (blue line) which is coincident within the experimental error with the maximum of the CONTIN distribution of relaxation times.

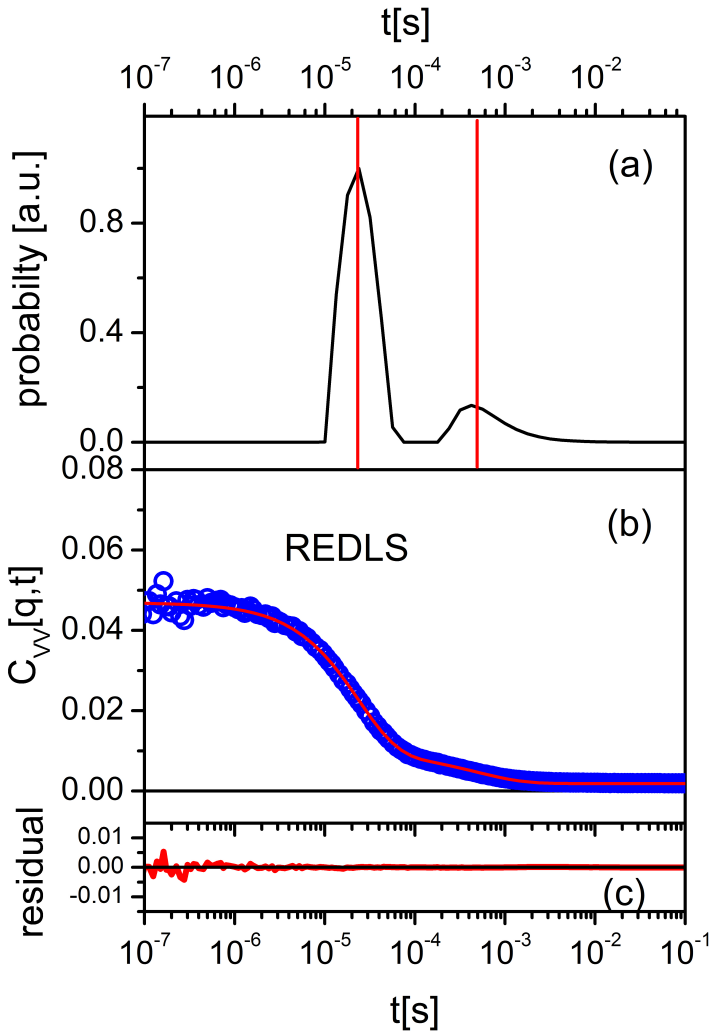

Figure 2.9: Comparison of results from KWW and CONTIN method for 60/25 nm CTAB-GNRs at a scattering angle of 90° (q = 0.019 nm^{-1}) in VV geometry. (a) CONTIN distribution of relaxation times for the REDLS experiment with red, vertical lines showing the resulting $<\tau>$ from KWW fit. (b) Fitting the data using KWW function (solid, red line through the data points). Here due to the not unambiguous fit from Cumulant this method was not used and only KWW and CONTIN are compared. (c) The residual plot for the fit with the KWW function.

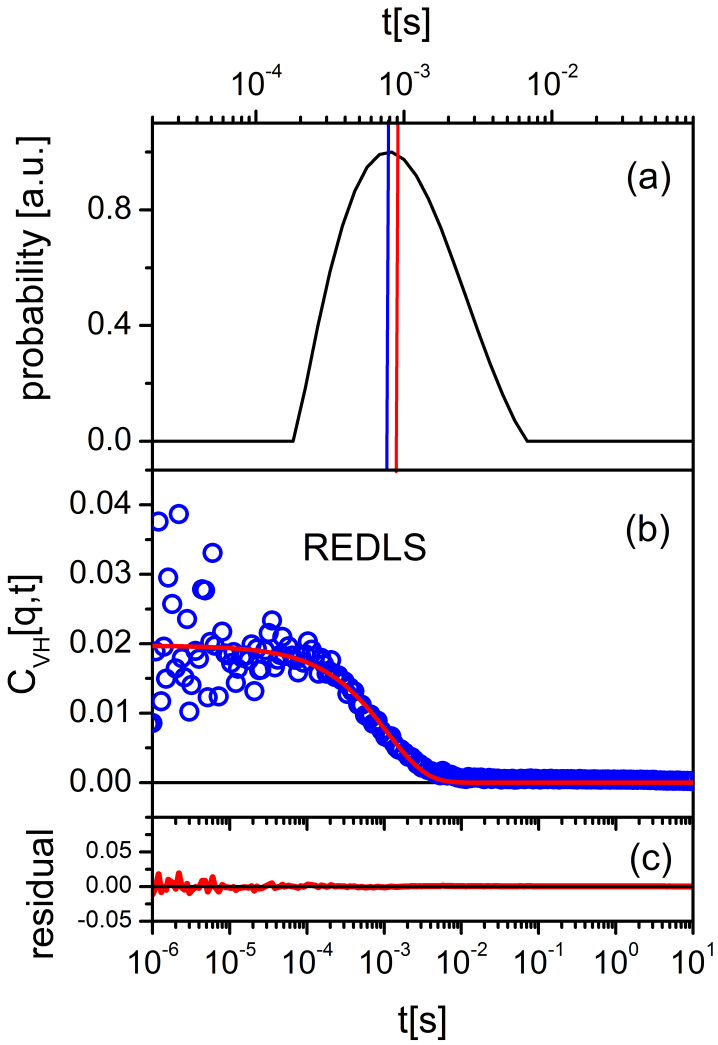

Figure 2.10: Comparison of results from KWW, Cumulant and CONTIN method for 60/25 nm CTAB-GNRs at a scattering angle of 90° (q = 0.019 nm^{-1}) in VH geometry. (a) CONTIN distribution of relaxation times (black curve) for the REDLS experiment with red and blue vertical lines showing the results from KWW fit and Cumulant, respectively. (b): fitting the data using KWW function (solid, red line through the data points). (c) is the residual plot for the fit with the KWW function.

2.5 Stokes-Einstein relation

The Brownian motion is described by a well-established law given by the combination of the Einstein-Smoluchowski equation and the Stokes' law.

The Stokes' law is a mathematical description of the force required to move a sphere

through a quiescent, viscous fluid at specific velocity.

Stokes' law is written as

$$\vec{F} = -6\pi\eta R_h \vec{v}, \tag{2.38}$$

where R_h is the radius of the sphere, η is the viscosity of the medium and v is its velocity.

The Einstein-Smoluchowski equation is defined as

$$\vec{F} = -\frac{k_B T}{D_0} \cdot \vec{v}. \tag{2.39}$$

A combination of the equations 2.38 and 2.39 leads to the the Stokes-Einstein relation

$$D_0 = \frac{k_B T}{6\pi\eta R_h}, \tag{2.40}$$

where k_B is the Boltzmann constant. The Stokes-Einstein relation is used to determine the hydrodynamic radius R_h of a particle in a solvent. The particle might be hydrated, which means that there is a layer of solvent molecules around the particle. The hydrodynamic radius takes this additional solvent layer into account. The thickness of this layer depends on the particle surface, shape and on the system temperature, while different solvents lead to different layer characteristics. The hydrodynamic radius of a specific particle then depends on the surrounding liquid. So this radius is not the hard core radius of the particle, but the radius of an imaginary sphere that diffuses at the same rate as the particle in solution.

2.6 Dynamic light scattering in evanescent geometry

One of the first dynamic light scattering measurement in evanescent geometry has been done by Lan et al [25] and is called Evanescent Wave Dynamic Light Scattering (EWDLS). In this technique the evanescent field is generated with the help of total internal reflection and then used as the light source for the dynamic light scattering measurement close to a wall.

In this thesis, I have used two recently developed methods; Resonance Enhanced Dynamic Light Scattering (REDLS) and Waveguide Enhanced Dynamic Light Scattering (WEDLS), for the measurement close to a solid charged (gold) and neutral (PMMA) wall [28,29,84]. An advantage of this technique as compared to EWDLS is an enhanced sensitivity and signal-to-noise ratio [29]. This allows studying the translational and rotational dynamics of nanoparticles close to a wall. In REDLS, the evanescent field of the surface plasmon was used as the light source whereas in WEDLS the evanescent field of a metal enhanced leaky waveguide has been used. In the following, I will explain briefly how the interface influences the dynamics of nanoparticles close to a wall including the anisotropic diffusion near a wall.

2.6.1 Influence of hydrodynamic effects on diffusion near a wall

Interfaces significantly influence the dynamics of particles in their vicinity. A sphere of hydrodynamic radius R_h moving at a drift velocity $\vec{v}$ in a bulk solution of viscosity η experiences a drag force $\vec{F}$ opposite to the drift velocity which can be computed as [80]

$$\vec{F} = -\frac{k_B T}{D_0} \cdot \vec{v} \tag{2.41}$$

where D_0, k_B and T represent diffusion coefficient, Boltzmann constant and temperature, respectively.

As a sphere approaches a solid surface, the drag force increases and diffusion is hindered. It is due to the hydrodynamic interaction of the sphere with the surface and results in an anisotropic diffusion parallel and perpendicular to the surface. This can be taken into account by including a correction factor which depends on the drag force. The drag force depends on the surface properties (e.g. mobility, hardness, form) as well as particle properties (e.g. size, structure, distance from the surface).

Neglecting non-hydrodynamic effects like chemical, electrostatic and electro-osmotic forces along with an assumption of nonslip boundary conditions and a low Reynolds number, one can compute the drag force using Stokes' law [85]. Due to the linearity of equation 2.41, both drag force $\vec{F}$ and diffusion coefficient D_0 can be resolved into

independent components for motion parallel and perpendicular to the wall [85].

Happel and Brenner derived the correction factor of the diffusion coefficient for motion perpendicular to a surface as [80]

$$\lambda_\perp = \frac{D_0}{D_\perp} = \frac{4}{3}\sinh(A)\sum_{n=0}^{\infty}\frac{n(n+1)}{(2n-1)(2n+3)}\cdot\left[\frac{2\sinh(A\cdot B)+B\sinh(2A)}{2\sinh((n+\frac{1}{2})A)^2-B^2\sinh^2(A)}-1\right], \tag{2.42}$$

with $A = \operatorname{arccosh}(z/R_h)$ in which z ($z = R_h + h$) represents the distance of the center of the diffusing spherical particle from the surface and $B = 2n + 1$. Assuming z to be very large ($h > 2R_h$), it is sufficient to use only the first summand of the equation 2.42. In addition, one can approximate $\sinh(A)$ through an exponential function by using again the first term, so one gets a simple expression for correction factor of the diffusion coefficient for motion perpendicular to a surface [77]

$$\lambda_\perp = \left[1-\frac{9R_h}{8z}\right]^{-1}. \tag{2.43}$$

The motion of a sphere parallel to a surface is more complicated due to the torque acting on the sphere. The shear on the side of the sphere facing the interface is higher than the shear on the opposite side, consequence of which is a torque resulting in rotation of the sphere. Considering purely hydrodynamic conditions, magnitudes of drag force $\vec{F}$ and torque $\vec{M}$ acting on a sphere moving with a velocity $\vec{v}_\parallel$ and rotating with an angular velocity ω can be described in terms of translational (F_t, M_t) and rotational (F_r, M_r) components using the expressions [86]

$$F = 6\pi\eta R_h(v_\parallel F_t + \omega R_h F_r) \tag{2.44}$$

and

$$M = 8\pi\eta R_h^2(v_\parallel M_t + \omega R_h M_r). \tag{2.45}$$

F_t, F_r, M_t and M_r are dimensionless functions and depend on the distance of the sphere from the surface. The subscripts t and r represent translation and rotation.

For a freely rotating sphere, torque M is zero and angular velocity ω can be determined by the expression [85]

$$\omega = -\frac{M_t}{M_r R_h} v_{\parallel}. \tag{2.46}$$

Therefore, the correction factor of the diffusion coefficient for motion in parallel direction can be calculated by [87]

$$\lambda_{\parallel} = \frac{D_0}{D_{\parallel}} = F_t - \frac{M_t}{M_r} F_r. \tag{2.47}$$

If the distance between the particle and the wall is very large ($h > 0.4R_h$), the analytical approximation by Faxén reported in the literature yields the expression [77, 80]

$$\lambda_{\parallel} \approx -\frac{1}{1 - \frac{9}{16}\frac{R_h}{z} + \frac{1}{8}(\frac{R_h}{z})^3 - \frac{45}{256}(\frac{R_h}{z})^4 - \frac{1}{16}(\frac{R_h}{z})^5}. \tag{2.48}$$

There is a slight deviation of ca. 10% for $h > 0.04R_h$ between the numerical calculations by O'Neill and the analytical approximation by Faxén [77]. The correction factors of the diffusion coefficients, $\lambda_{\perp}$ and $\lambda_{\parallel}$, from the equations 2.42 and 2.48 are larger than one and different from each other [87]. In this case one gets a decrease as well as an isotropy of the particle movements close to the surface.

2.6.2 Anisotropic diffusion near solid walls

As discussed above, when a spherical particle approaches a wall the drag force leads to an anisotropic hindered diffusion parallel and normal to the wall, i.e. $D_{\parallel,\perp}/D_0 \leq 1$ [80]. By considering the hydrodynamic interaction between the particle and the wall as well as the exponentially decaying evanescent field of the excitation light, the measurable relaxation rate can be rewritten as [77, 79, 88]

$$\Gamma_c = \left(\langle D_{\parallel} \rangle (\xi) q_{\parallel}^2 + \langle D_{\perp} \rangle (\xi) (q_{\perp}^2 + \frac{1}{\xi^2}) \right). \tag{2.49}$$

Here, $q_{\parallel,\perp}$ are the components of the magnitude of the scattering vector q and $D_{\parallel,\perp}$,

the mean diffusivities parallel and perpendicular to the surface. ξ is the penetration depth of the evanescent wave. In dynamic light scattering in evanescent geometry one measures the mean diffusivities because it is not possible to measure the diffusion for a fixed distance from the surface. The mean diffusivities can be defined as [77]

$$D_{\parallel,\perp} = D_0 \frac{2}{\xi} \int_R^\infty dz \cdot exp\{-\frac{2}{\xi}(Z-R)\} \cdot {\lambda_{\parallel,\perp}}^{-1} \tag{2.50}$$

with $\lambda_{\parallel,\perp} = D_0/D_{\parallel,\perp}$ being the correction factor of the diffusion coefficient. The normalized mean diffusion coefficient as a function of the reduced penetration depth ξ/R_h of the evanescent wave is shown in Figure 2.11 [77].

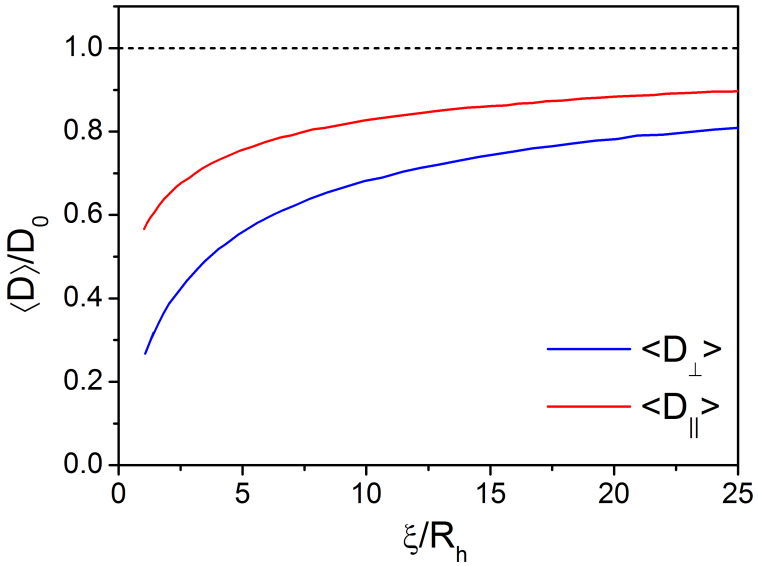

Figure 2.11: Normalized mean diffusion coefficient $\langle D_{\parallel,\perp} \rangle / D_0$ as a function of the reduced penetration depth ξ/R_h of the evanescent wave [77]

Chapter 3

Materials and methods

In this chapter, I will introduce the sample preparation as well as the main experimental methods used in this work. In particular, these are Dynamic Light Scattering (DLS) and Resonance Enhanced Dynamic Light Scattering (REDLS) which is a combination of Surface Plasmon Resonance (SPR) Spectroscopy and DLS.

3.1 Sample

3.1.1 Gold nanorods (GNRs)

Aqueous suspensions of GNRs with nominal length- (L) to-thickness (d) ratios, L/d, equal to 135/20 (with 6.2×10^{11} NPs/cm^3 or 1 nM), 45/10 (with 5×10^{11} NPs/cm^3 or 0.8 nM), and 60/25 (with 1×10^{11} NPs/cm^3 or 0.2 nM) were purchased from Nanopartz^{TM}, Loveland, CO. The GNRs were charge-stabilized with a layer of cetyltrimethylammonium bromide (CTAB) on their surface. Dust free solutions were prepared by filtering the GNRs suspensions through a Millex HA 0.45 μm polytetrafluoroethylene (PTFE) filter (Millipore, UK).

3.1.2 MTAB stablized GNRs

For MTAB (16-mercaptohexadecyl trimethylammonium bromide) stabilized GNRs, again commercial GNRs with the aspect ratio of 2.4 (60/25 nm), charge stabilized with

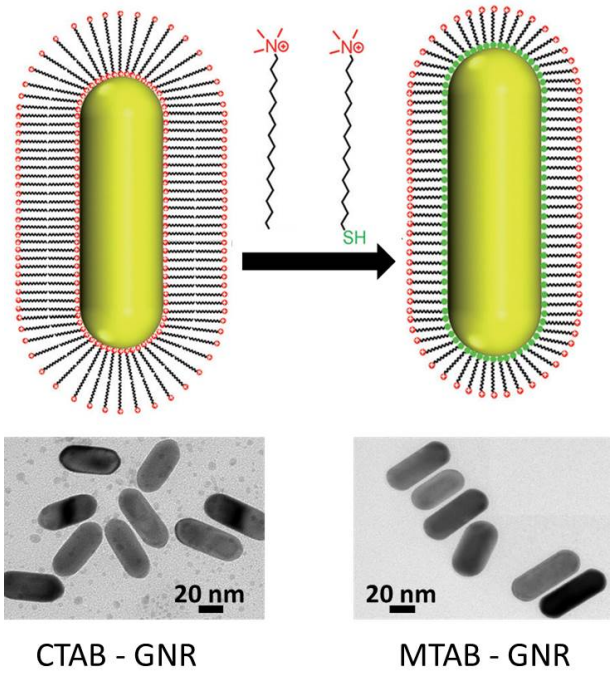

Figure 3.1: Exchange of the CTAB for the MTAB thiol. The grey spots in the TEM picture around the CTAB-GNRs are probably collapsed micelles of free CTAB after drying the sample on the TEM grid.

a layer of CTAB (cetyltrimethylammonium bromide) at their surface, were obtained. To avoid CTAB in solution, the CTAB was replaced with MTAB. MTAB was synthesized according to the procedure reported by Vigderman et al [89]. CTAB stabilized GNRs were washed two times using centrifugation at 13000 rpm. The washed GNRs were dispersed in water and mixed with 5 ml solution of MTAB (1 mg/ml). The resulting dispersion was stirred for three days at room temperature. The MTAB functionalized GNRs were purified by 2 cycles of centrifugation (13000 rpm) and finally dispersed in water to a concentration similar to the original GNRs dispersion. Dust free solutions for DLS and REDLS were prepared by filtering MTAB stabilized GNRs in Milli-Q water through a Millex HA 0.45 μm PTFE filter (Millipore, UK). Figure 3.1 shows the exchange of the CTAB for the MTAB thiol, which is covalently anchored to the surface through gold-sulfur bonds. In the TEM image the successfull exchange of CTAB for MTAB can be seen. The grey spots in the TEM picture around the CTAB-GNRs are probably collapsed micelles of free CTAB after drying the sample on the TEM grid. In this work, the functionalizing of GNRs with MTAB has been done by Dr. Muhammad

Nawaz Tahir from the University of Mainz [90].

3.1.3 Silica coated GNRs (SiO_2@GNRs)

For silica coating, commercial GNRs with aspect ratio (L/d) of 2.4 (60/25 nm) charge stabilized with a layer of CTAB on their surface were used. SiO_2@GNRs were synthesized according to the procedure reported by Chen et al [91,92]. The GNRs (0.43 mg) were washed twice with fresh Milli-Q water (Millipore purification system operating at 18.2 MΩ) in subsequent centrifugation steps (for 30 min at 18,000 g) and then resuspended in 20 ml Milli-Q water. A solution of O-(2-mercaptoethyl)-O′-methyl-hexa(ethylene glycol) (mPEG-thiol, MW 5,000, Laysan Bio, 10 ml, 0.2 mM) was stirred vigorously and the GNR suspension was added. The mixture was sonicated for 30 s and then stirred for 2 h. The suspension was centrifugated (for 20 min at 8,000 g) and the GNRs were resuspended in 1.2 ml Milli-Q water. The suspension was added to vigorously stirred 2-propanol (Sigma-Aldrich, 1.8 ml) and a solution of 0.4 ml aqueous ammonium hydroxide (28%, VWR) in 5 ml 2-propanol was added slowly. Half of a solution of tetraethyl orthosilicate (98%, Sigma-Aldrich) in 2-propanol (2 ml, 410 mM) was added immediately, the other half over a time span of 1 hours. After 3 hours, the SiO_2@GNRs were washed with 2-propanol and fresh Milli-Q water. The SiO_2@GNRs have been prepared by Dr. Lena Mammen from the Max Planck Institute for Polymer Research (MPI-P).

3.2 Metal evaporation

The substrates (26 mm×76 mm×1.5 mm) have been cutted in three parts and then cleaned with the Milli-Q water to remove dust from the substrates. Substrates were cleaned by immersion in a 1% Hellmanex solution (Hellma GmbH, Müllheim) for 15 minutes in the ultrasonic bath. Afterwards, they were washed several times with ethanol and Milli-Q water and dried with nitrogen gas. For measurements close to a wall with resonance enhanced dynamic light scattering (REDLS), a smooth gold layer is required

for high surface plasmon coupling beyond 95% coupling efficiency. In this work, the substrates were prepared by thermal evaporation at a constant rate of 1 Å/s and at a pressure of 5×10^{-6} mbar. The evaporation has been performed for 47 nm thin film of gold onto NLAK8 glass slides (n = 1.710, Hellma GmbH, Müllheim) with a 1 nm layer of chromium as an adhesive layer inbetween. To prevent adhesion and aggregation of the GNRs onto the gold layer, it was coated with a monolayer of 2-aminoethanethiol (cysteamine). This provides a positively charged surface in water. To prepare the surface layer, the gold coated glass substrates were stored in a 1 mM solution of cysteamine in ethanol for 24 hours. Thus, it is possible to alter the effect of electrostatic particle-surface repulsions on the surface-induced diffusion anisotropy. Section 4.2, provides further details.

3.3 Spin-coating technique

A technique to coat a substrate with a thin layer of polymer is the spin-coating technique. A droplet of a polymer solution is put on a flat substrate. Then this substrate is set in rotation. The rotation spreads the liquid over the substrate. If the substrate is hydrophobic, such as the silanized or thiolized surfaces, the droplet may flow off the substrate or may form a film which dewetts macroscopically during the spin-coatig process. In this case it is useful to scratch a lattice pattern into the substrate. Sometimes it is sufficient to make a single circular scratch. The scratches act as pinning lines to avoid dewetting. During the evaporation of the solvent, the polymer solidifies and forms a smooth film. The thickness d of the resulting film depends on the viscosity, the polymer concentration, and the spin-frequency f ($d \propto \sqrt{1/f}$). Using polymer concentrations between 0.1% and 5% and spin speeds between 10000 and 1000 rpm, film thicknesses from a few angstrom up to a few micrometers can be realized [93]. If a good solvent is used, the resulting polymer films are of a surprising quality with a roughness of only a few angstrom. Figure 3.2 shows the schematic representation of the spin-coating process. The substrate is fixed with the vacuum chuck. After applying the polymer solution on the substrate, closing the glass encloser and adjusting the rotational speed, the spin

coating process can be started.

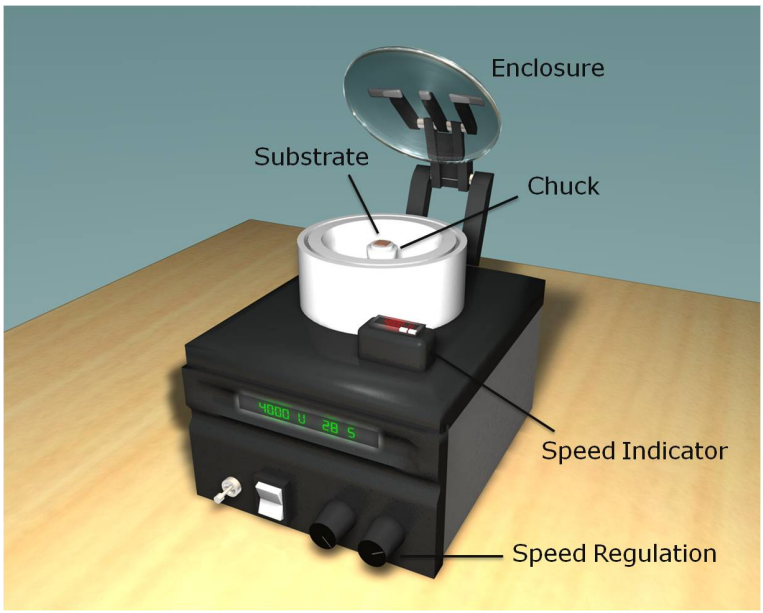

Figure 3.2: Representation of the spin-coating process to produce smooth films.

There are three steps in the spin coating process:

- *Deposition, Dispense.* The substrate is fixed through the vacuum chuck. After filtering the polymer solution, the surface should be completely covered with the solution before spin coating (Figure 3.3(a)).

- *Thinning, Spreading.* Afterwards the chuck starts to rotate and the polymer solution dispenses on the substrate through the centrifugal force. The spinning time and spinning speed can be adjusted on the spin-coater. The thickness of the resulting film can be estimated with the help of the viscosity, the polymer concentration and the spin-frequency (Figure 3.3(b)).

- *Evaporation, Drying.* Finally the polymer solution evaporates, so that the polymer solution formed as a film on the substrate (Figure 3.3(c)).

In this work, the spin-coating technique has been used for the preparation of the thick polymer film (waveguide). The films are characterized by profilometer (Tencor P-10) and SPR. The primary characterization of the thickness was done on test samples by means of a profilometer with resolution of approximately 1 nm. These films were not

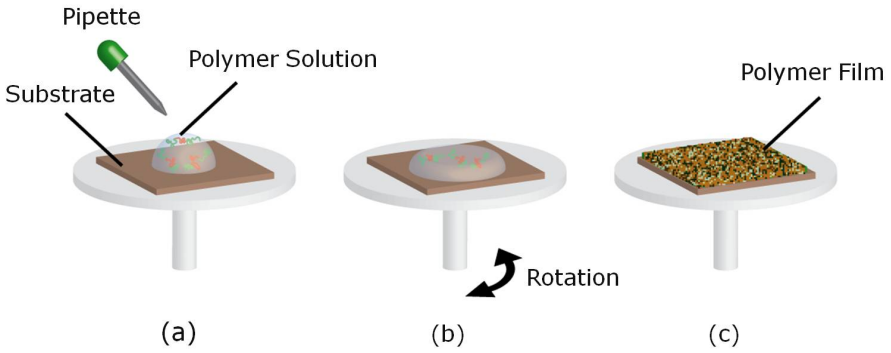

Figure 3.3: Schematic representation of the the spin-coating procedure. (a) Fixing the substrate and applying the polymer solution on the substrate. (b) Spreading the solution via the rotation of the spin-coater. (c) Drying the solution and formation of a polymer film.

used in my measurements. Instead, films prepared with exactly the same parameters were used for the experiments with WEDLS.

3.4 Preparation of waveguide

To prepare the waveguide structure, right after deposition of the gold layer on the NLAK8 glass the gold covered glass was functionalized with 3-(4-benzoylphenoxy)-propanethiol (BPSH) for 12 hours by immersion [94]. Right after the poly(methyl methacrylate) (PMMA) layer was spin coated (t = 7.5 min., 1500 rpm) with a solution of PMMA (M_w = 90 kg/mol, M_w/M_n = 1.03) in high purity cyclohexanone with concentration 11 % w./w (Section 3.3). Prior to use the solution, it was filtered through a PTFE Millipore filter (0.22 μm pore size). The PMMA film was annealed at 130° (Tg + 25°C) for about 24 h and finally cross-linked by applying UV radiation (λ = 254 nm) for 6 h [84]. Not only does the film not swell in water afterwards, but it is, due to crosslinking to the BPSH, covalently attached to the interface which prevents delamination/dewetting.

3.5 UV-Visible absorption spectroscopy (UV-Vis)

Energy absorbed in the UV or visible region causes a change in the electronic excitation of the molecule and hence results in a corresponding change in its ability to absorb light

in the UV-visible region of the electromagnetic radiation. The relationship between energy absorbed in an electronic transition and the frequency (υ), wavelength (λ) and wave number ($\bar{\nu}$) of radiation producing the transition is given as

$$\Delta E = h\upsilon = h\frac{c}{\lambda} = h\bar{\nu}c \tag{3.1}$$

where h is Planck's constant, c is the velocity of light and ΔE is Energy absorbed in an electronic transition in a molecule from ground state (lower energy) to excited state (higher energy).

The energy absorbed depends on the energy difference between ground state and excited state. The smaller the difference the larger the wavelength of absorption. The principal characteristics of an absorption band are position and intensity. The position of an absorption band corresponds to the wavelength of radiation whose energy is equal to that required for an electronic transition. The intensity of absorption depends on the probability of interaction between the radiation energy and the electronic system and the difference between the ground state and excited states.

The intensity of absorption is derived from Beer-Lambert's law: $A = \log \frac{I_0}{I} = \epsilon cl$, where A is the measured absorbance, I_0 intensity of the incident light, I intensity of the light transmitted through the sample, ϵ ($Lmol^{-1}cm^{-1}$) the proportionality constant called *absorptivity*, l (cm) the path length of the cell and c (mol/L) is the concentration of the analyte.

In the work presented in this thesis, UV-Vis absorption spectroscopy has been used to monitor the absorption spectra of GNRs and SiO_2@GNRs in order to find the transversal and longitudinal plasmon mode. The measurements were performed on a Perkin-Elmer Lambda 900 spectrometer using 1 cm path cells. Figure 3.4 shows the absorption spectrum of 60/25 nm GNRs with two absorption maxima at 532 nm and 634 nm, which correspond to the transverse plasmon band and longitudinal plasmon band, respectively.

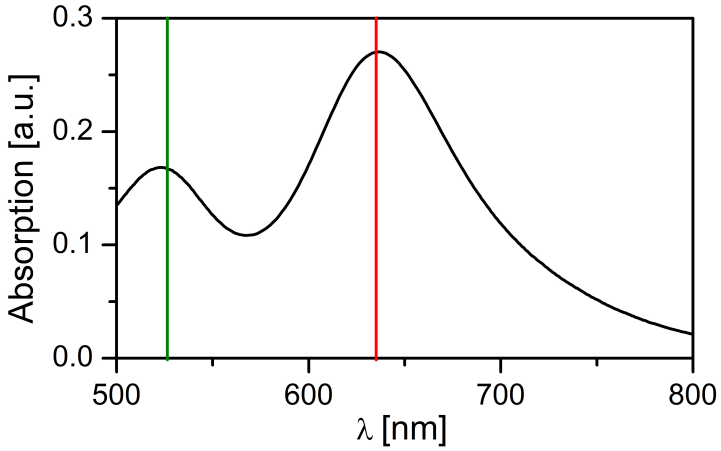

Figure 3.4: Absorption spectrum of 60/25 nm GNRs with two absorption maxima at 532 nm and 634 nm, which correspond to the transverse plasmon band and longitudinal plasmon band, respectively.

3.6 Transmission electron microscopy (TEM)

A beam of accelerated electrons interacts with an object in a conventional TEM. The transmitted electrons are used to create an image of the sample. Scattering occurs when the electron beam interacts with matter. Scattering can be elastic (no energy change) or inelastic (energy change). Elastic scattering can be both coherent and incoherent (with or without phase relationships). Elastic scattering occurring from well-ordered arrangements of atoms results in coherent scattering, giving spot patterns. Inelastic processes give characteristic absorption or emission, specific to the compound, element or chemical structure.

In this work, a Tecnai F20 microscope (FEI; 200 kV) for imaging the GNRs and silica coated GNRs (SiO_2@GNRs) was used. Samples were prepared by drop evaporation of aqueous solutions on a copper grid. Statistical analyses of TEM images to characterize the size of samples were performed by using the software program *ImageJ 1.45s* (developer: Wayne Rasband, Research Services Branch of the National Institute of Mental Health). From the TEM images of the GNRs samples, I estimated their lengths (L) and thicknesses (d) which are listed in Table 3.1, as well as the width of the aspect ratio distribution using a Gaussian representation. This width determined to 0.54, 0.57 and 1.2 for 60/25, 45/10 and 135/20 GNRs, respectively (Figure 3.5).

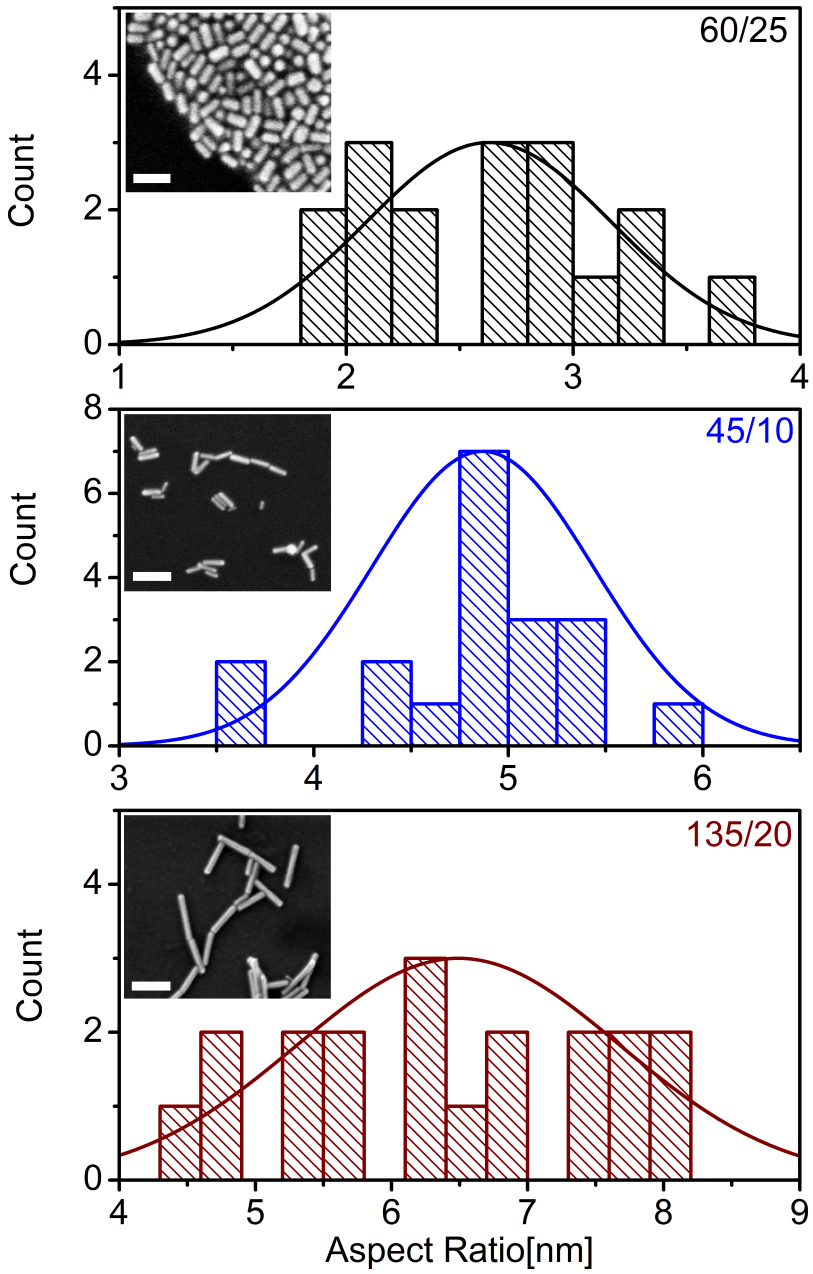

Figure 3.5: Histogram obtained from TEM (inset, scale bars = 100 nm) showing the size distribution of GNRs for three different sizes of GNRs.

Table 3.1: Length (L) and diameters (d) of three GNRs with different aspect ratios (L/d)

	reported by supplier			determined by TEM[a]		
Samples	L[nm]	d[nm]	L/d	L[nm]	d[nm]	L/d
60/25	58	25	2.3	68	27	2.5
45/10	44	10	4.4	54	11	4.9
135/20	134	20	6.7	117	18	6.5

[a] Error of 8% for L and 20% for d.

The number of SiO_2@GNRs counted was in the range of 200. The TEM images reveal an uniform shape of silica coating of the GNRs. Figure 3.6 shows a histogram obtained from TEM (inset) showing the size distribution of the SiO_2@GNRs with a mean diameter of 180.2 ± 26.2 nm using a Gaussian fit. About half of the spheres contain a GNR.

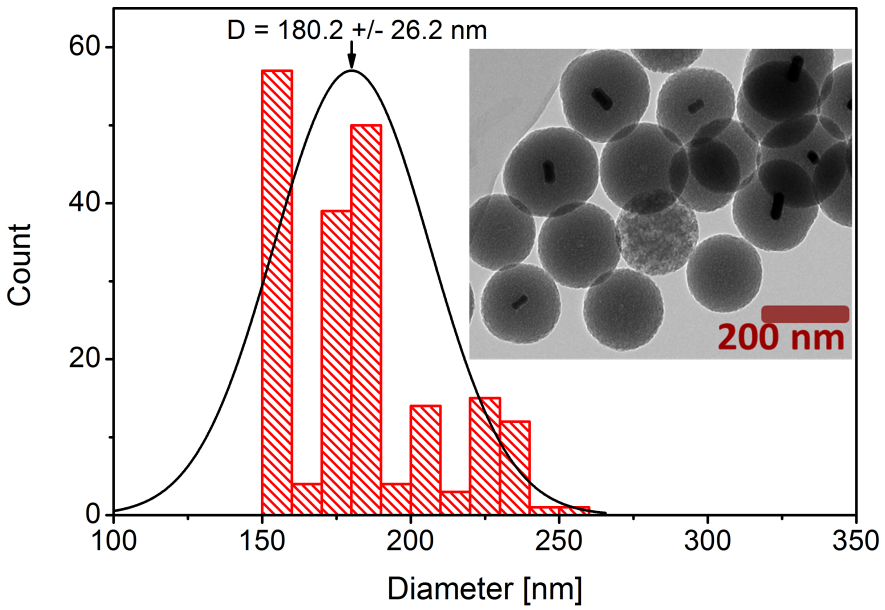

Figure 3.6: Histogram obtained from TEM (inset) showing the size distribution of the silica coated GNRs with a mean diameter of 180.2 ± 26.2 nm. About half of the spheres contain a GNR.

3.7 Surface plasmon resonance (SPR) spectroscopy

Surface plasmon resonance (SPR) spectroscopy is a surface sensitive optical reflection technique which non-invasively monitors changes in the local index of refraction at a metal surface [95, 96]. In this work, this method is used to measure the reflectivity in order to find the incident angle for surface plasmon excitation as well as for kinetic SPR which will be explained in the next section. This is utilized in the so-called Kretschmann configuration [97] which is shown in Figure 3.7. Angular resolved techniques using a prism in a total internal reflection (TIR) configuration are the most common configuration, the other methods use grating coupling [95].

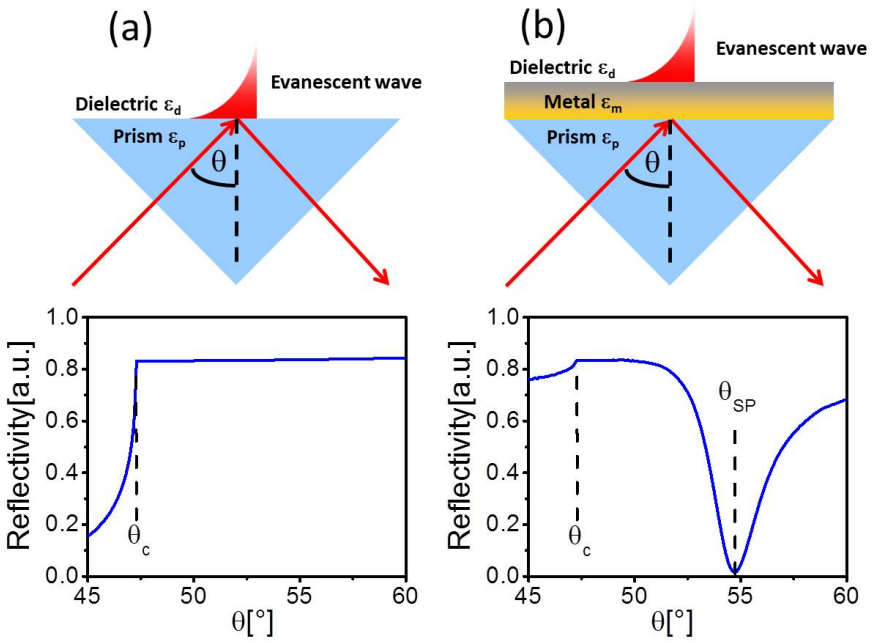

Figure 3.7: Total internal reflection at a glass prism in contact with a dielectric without a metal film (a) and at a metal film (b). θ_c denotes the critical angle and θ_{sp} the angle of SP resonance.

Using a metal film at the base of a prism (Figure 3.7(b)) results in a minimum of the reflectivity curve and one can measure with much higher intensity of the evanescent field compared to the intensity in case of no metal film (Figure 3.7(a)). Because the photons are coupled to the metal/dielectric interface via the evanescent tail of the light at the base of a high index prism.

Figure 3.8 shows the used SPR setup for the reflectivity measurement. A NLAK8 glass substrate with gold layer was attached with immersion oil with refractive index n = 1.715 (Series M, 1.7150, Cargille Laboratories) to the base of a NLAK8 prism (Hellma GmbH, Germany). The reason for using a glass substrate is that it enables the use of the high price prism as often as needed. Monochromatic light of a HeNe laser (Uniphase) with $\lambda = 632.8$ nm was modulated by a chopper. To ensure linear transverse magnetic polarized (p-polarized) light, a Glan-Thompson polarizer with extinction coefficient 10^{-5} (B. Halle, Germany) was inserted in the incident beam. To vary the intensity of the light a second polarizer was placed in the incident beam. This light was focused by a lens (focal length: 500 mm) onto the metal layer. The suspension in a quartz

cell (Type-Nr.: 136.045-QS (V2), Hellma GmbH, Germany) was mounted on a two-circle goniometer (Huber, Germany). Varying the external angle of incidence ψ, angular dependent intensities are recorded by a photo-diode (220D, OSI Optoelectronic GmbH, Germany). The recorded signal was than measured with the help of a Lock-In amplifier (Model 7265, Signal Recovery). The Lock-In amplifier compares the signal frequency with the chopper frequency and can filter out the light which is not modulated with this frequency. This leads to an enhancement of the signal-to-noise ratio [98, 99]. The folding mirror was used to choose between photo-diode in the reflectivity measurement and DLS-detector for the measurement close to the surface with REDLS.

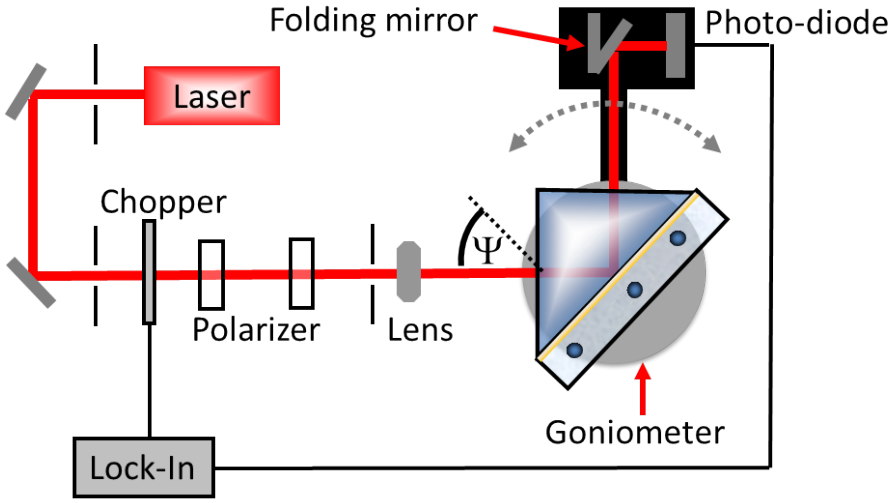

Figure 3.8: SPR setup: Kretschmann-Raether configuration for surface plasmon excitation and measuring the reflectivity.

3.8 Kinetic surface plasmon resonance

Kinetic SPR is an optical method that probes the thickness and dielectric constant of thin film at a noble metal surface. To describe the phenomena at interfaces, scan and kinetic SPR measurements have been used. In the scan mode the reflectivity changes are monitored as a function of the angle. The resonance angle is highly sensitive to the dielectric constant of the medium surrounding the metal interface. Any shift in the resonance angle indicates that some material binds to or dissociates from the metal

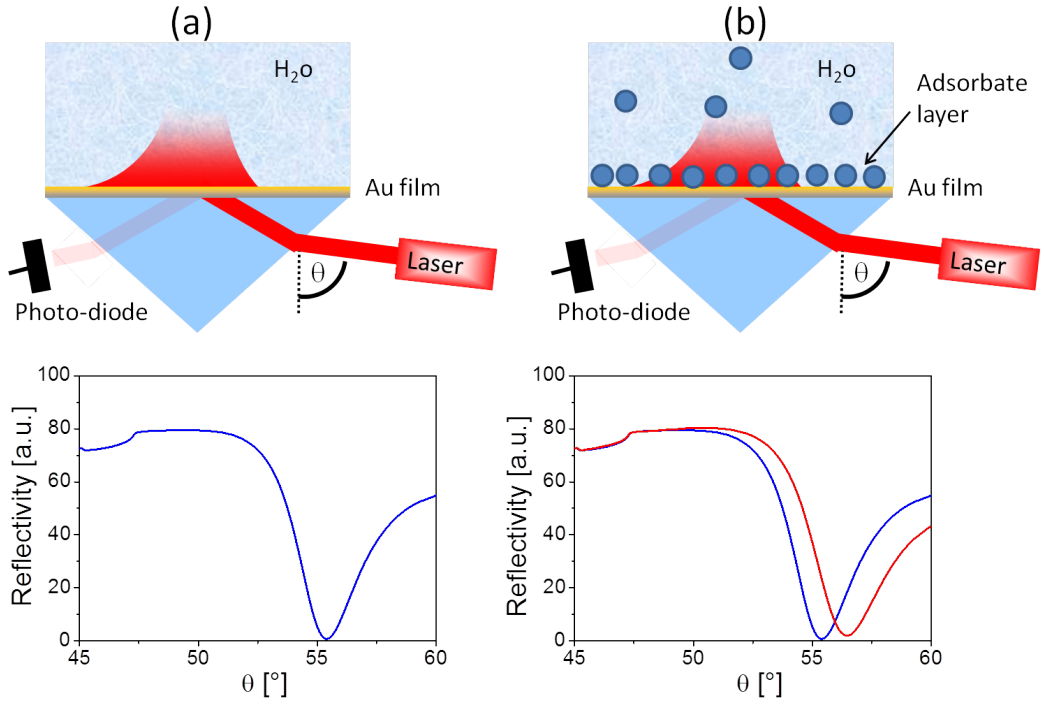

Figure 3.9: Schematic of the molecular adsorption and angular shift with the SPR measurement. (a): Reflectivity scan for water. (b): Reflectivity scan after adsorption of some materials on the surface which result in a shift in the reflectivity scan.

interface. Figure 3.9 shows the molecular adsorption and angular shift with the SPR measurement. In Figure 3.9(a) the reflectivity scan as a function of the angle for water is shown. By injection of material that binds to the surface, one observes a shift in the reflectivity scan (Figure 3.9(b)). These phenomena can be probed additionally by kinetic measurement at a certain angle which shows a linear region close to the resonance angle in order to achieve a proportional relation between reflected intensity and the layer's growth [100]. Figure 3.10(a) shows a shift in the resonance angle and Figure 3.10(b) exhibits the corresponding kinetic measurement of the adsorption process.

The thickness of the film can be estimated from [101]:

$$d_f = \frac{\epsilon_s \lambda \sqrt{-\epsilon_m}(\epsilon_s - \epsilon_m)\epsilon_f}{2\pi(\epsilon_f - \epsilon_s)(\epsilon_f - \epsilon_m)}\left(\frac{\epsilon_m + \epsilon_s}{\epsilon_m \epsilon_s}\right)^2 \Delta(\sin\theta_r) \tag{3.2}$$

where ϵ_s, ϵ_m and ϵ_f are the dielectric constants of the solvent, the real part of the dielectric constant of the metal and the dielectric constant of the film, respectively. λ is the wavelength of the laser (632.8 nm) and θ_r is the resonance angle of the plasmon

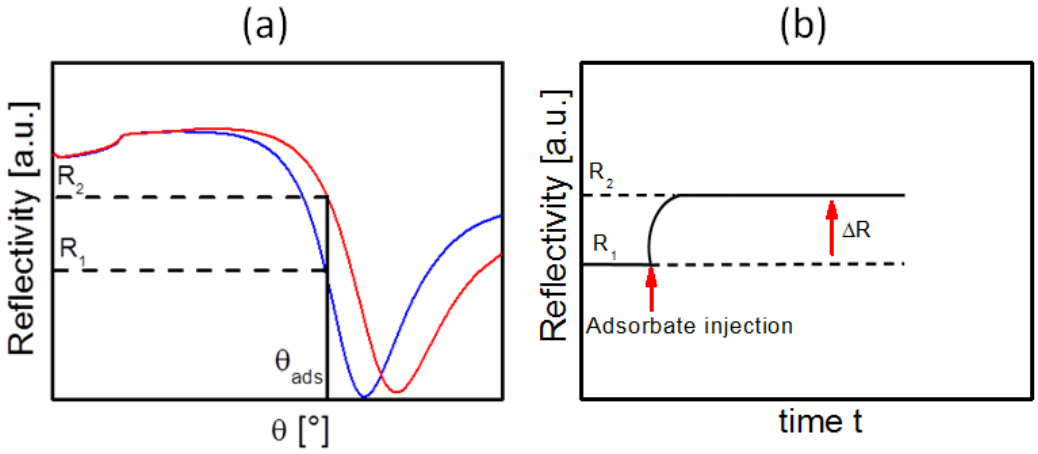

Figure 3.10: Kinetic SPR measurement. (a) Reflectivity scan for a material that binds to the surface. θ_{ads} indicates the used angle for the kinetic SPR. (b) The corresponding kinetic measurement at angle θ_{ads}.

resonance curve. The SPR configuration is described above in Section 3.7.

3.9 Dynamic light scattering (DLS)

All DLS experiments in this thesis were performed on a setup built in-house at the Max Planck Institute for Polymer Research (MPI-P). DLS experiments were performed at different scattering angles between 20° and 120°, corresponding to a scattering vector q = 1.43 × 10^{-2} - 8.04 × 10^{-3} nm^{-1} using an ALV-6010/160E digital full correlator (ALV GmbH, Langen, Germany). All measurements were carried out at room temperature (∼T = 20°C). To demonstrate the DLS measurement at different wavelengths, four continuous-wave (cw) laser sources were incorporated in the DLS setup, with wavelengths of 532 nm (Verdi V2, Coherent, Santa Clara, CA), 634 nm and 660 nm (diode lasers, Coherent, Santa Clara, CA) and 832 nm (diode laser, SuK, Hamburg, Germany). Two avalanche photodiodes (SPCM-AQR-14, Perkin-Elmer, Wellesley, MA) were used for optimal detection. To remove unwanted contributions from correlated after-pulses, which are inherent in this type of detector, pseudo-cross-correlation measurements were performed. The scattered light from the sample was directed to the photodetectors by a single-mode Y-beam splitter fiber (SuK, Hamburg, Germany). A schema of the whole setup is shown in Figure 3.11. A laser beam passes trough a polarizer, reaches the sample

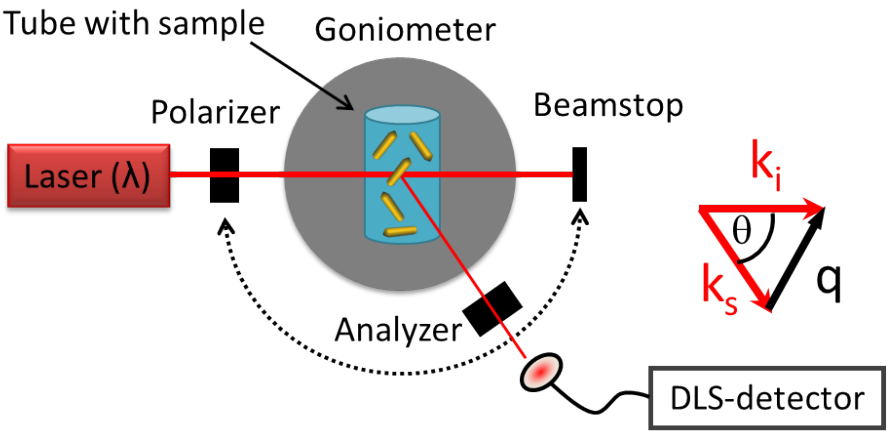

Figure 3.11: Schematic presentation of the in-house built DLS setup.

and scatters in all directions. A detector can be in principle placed in any of these directions and follow the fluctuation of the intensity of scattered light in time. Prior to light scattering measurements, the dispersion was prepared by filtering through a 0.45 μm PTFE filter (Millipore, UK) directly into cylindrical silica glass cuvettes (Hellma, inner diameter of 8 mm).

The incident beam is always vertically (V) polarized and the analyzer can be set to select vertically (V) or horizontally (H) scattered light. In DLS measurements, VV means that the polarization axis of incident and scattered light are vertical with respect to the scattering plane. The depolarized case VH means that the selected polarization of the scattered light is horizontal and thus perpendicular to the polarization of the incident beam. If no analyzer is used, it is called VU (vertical-unpolarized).

3.10 Resonance enhanced dynamic light scattering (REDLS)

REDLS method enables measurements of Brownian diffusion coefficients (parallel and perpendicular) close to the solid interface for particles as small as ca. 10 nm in radius. It enables to investigate interface induced dynamics, e.g. the hindering of diffusion and rotation close to a solid interface. The used setup is a combination of two well established techniques, Surface Plasmon Resonance (SPR) Spectroscopy and Dynamic

Light Scattering (DLS).

The first step was to prepare the sample and fix it to the setup. For this purpose the NLAK8 prism (Hellma GmbH, Germany) was attached to a NLAK8 glass substrate with gold layer using immersion oil that has a refractive index of n = 1.715 (Series M, 1.7150, Cargille Laboratories). Afterwards the prism and the quartz cell was installed to a special constructed rider assembly (Figure 3.12). The sample was then filtered using a Millex HA 0.45 μm filter (Millipore, UK) and filled into a quartz cell (Type-Nr.: 136.045-QS (V2), volume 20 μl, height 100 μm, Hellma GmbH, Germany). The reason for using a cell of small height is to reduce possible second or multiple light scattering of photons in the bulk.

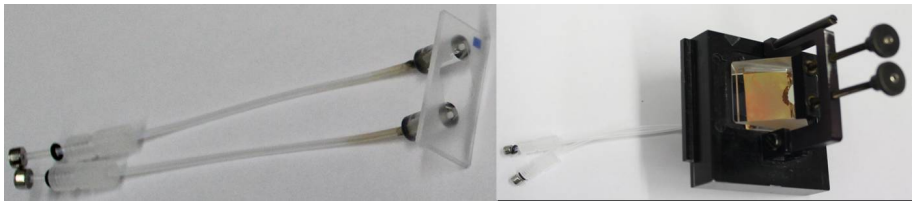

Figure 3.12: The picture shows the quartz cell and its installation onto the rider.

The measurement cell was assembled on a two-circle goniometer (414A-415A, Huber). Using two translation tables, two tilt tables and one height-adjustable table (Owis GmbH) placed between measurement cell and goniometer enables the precise alignment of the measurement cell. In this way it was possible to perform reflectivity measurement as well as light scattering in the evanescent geometry. The complete setup was placed on the top of an anti-vibration table (Table Stable TS300, Scientific Instruments GmbH) and the whole construction was enclosed in a dark box. This was necessary to decrease the effect of the external vibration modes e.g. from the building and any external correlated signal from an external source of light.

For REDLS measurement, the chopper was turned off because it modulates the light and generates an interfering correlated signal. With a folding mirror which is shown in Figure 3.8 one can choose between DLS-detector and photo-diode in the reflectivity measurement. The setup was moved to the resonance angle which was found by the reflectivity measurement. Only particles interacting with the evanescent field located

at the surface can scatter light. This scattered light is detected by the DLS-detector, which can be rotated to measure correlation functions at different scattering angles or different scattering vectors q. Figure 3.13 shows the schematic representation of the REDLS setup as well as the real setup in the lab.

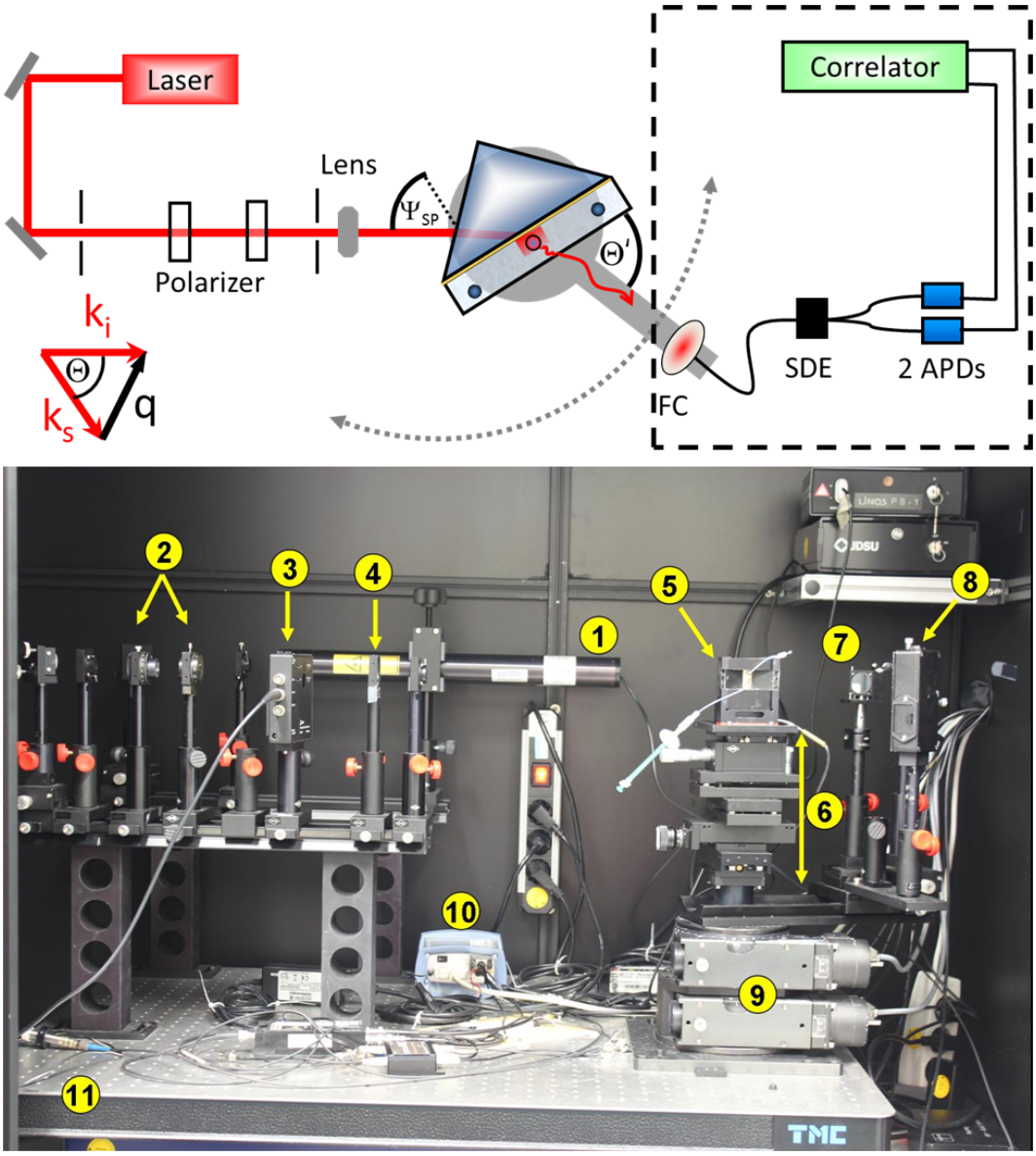

Figure 3.13: Upper picture: Schematic of the REDLS setup. Lower picture: REDLS setup in the lab: (1) He-Ne laser $\lambda = 632.8$ nm, (2) polarizers, (3) chopper for the SPR measurement, (4) lens, (5) measurement cell, (6) two translation tables, two tilt tables and one height-adjustable table, (7) folding mirror, (8) photo-diode for SPR which is replaced by DLS detector in REDLS measurement, (9) two-circle goniometer, (10) digital multiple tau correlator, (11) anti-vibration table.

The DLS detector consists of a lens focusing the scattered light onto a single mode fiber with fiber coupler (FC, Schaefter+Kirchhoff-SuK, Hamburg) to transport the light to two avalanche photodiodes (APD, SPCM-AQR-14, Perkin-Elmer), a static and dynamic enhancer (SDE, ALV GmbH, Langen) and a digital multiple tau correlator with fast option (ALV7004/fast multiple tau digital correlator, ALV GmbH). The static and dynamic enhancer is needed in heterodyne light scattering experiments using fibers as part of the detection system to remove unwanted contributions induced by the single mode fiber [87].

Normally, single mode fibers are ideal receivers in DLS. Because the sensitivity of single mode fibers is higher than a classical two aperture setup and the correlations show higher contrast levels [102, 103]. The problem in this type of fiber is that temperature fluctuations can couple with the fiber and result in phase interference. Thereby, self-correlation can appear. To avoid this self-correlation, the static and dynamic enhancer was used to decrease the contrast of the self-correlation [87].

In the DLS, the correlation is measured form the sub-μs region to about 1000 seconds. If one uses only one APD, the correlation function is distorted by the correlated after-pulsing of this type of detector. For this reason, the pseudo-cross-correlation technique was used in this work to eliminate the undesired signals [104]. This technique is based on splitting the incoming signal onto two photon detectors and then their outputs into a correlator.

With a Glan-Thompson polarizer with an extinction coefficient of 10^{-8} (B. Halle) placed between the sample and the DLS-detector, polarized and depolarized measurements can be performed. The REDLS measurements were performed at a fixed penetration depth (ξ) of 200 nm.

In REDLS experiment, the scattering angle Θ is not equivalent with the angle between scattering volume and detector Θ' (Figure 3.13). To calculate Θ one has to consider the water/air interface. From Snell's law (equation 2.21) the angle Θ is given by

$$\Theta = \arcsin\left(\frac{\sin\Theta' \cdot n_{air}}{n_{water}}\right) \approx \arcsin\left(\frac{\sin\Theta'}{1.33}\right). \tag{3.3}$$

3.11 Waveguide enhanced dynamic light scattering (WEDLS)

If a transparent dielectric layer is attached to a metal layer, new type of modes are generated by increasing the thickness of the dielectric layer [105]. These modes can be excited with s- (TE0, TE1, TE2, ...) as well as p-plarization (TM0, TM1, TM2, ...) and are called metal enhanced leaky waveguide [106, 107]. TM and TE stand for *transverse magnetic* and *transverse electric* modes, respectively. The number of the modes depends on the thickness and the refractive index of the layer. The surface plasmon resonance itself is the TM0 mode. Each of the modes (except TM0 for thick layers) has an evanescent tail that leaks into the dielectric medium above with different penetration depths for each mode

$$\xi_{TM1} < \xi_{TM2} < \xi_{TM3} < ... \tag{3.4}$$

and

$$\xi_{TE0} < \xi_{TE1} < \xi_{TE2} < ... \tag{3.5}$$

Figure 3.14(a) shows the schematic presentation of metal enhanced leaky waveguide in the Kretschmann-Raether configuration with the corresponding field distribution. P-polarized light leads to the TM modes whereas s-polarized light allows TE modes. The WINSPALL simulation in Figure 3.14(b) belongs to a 2000 nm PMMA layer on a 46 nm gold layer. The used dielectric constant and layer thickness for the simulation are shown in Table 3.2 [108–110]. In this thesis, the WINSPALL software was used to simulate resonance curves in order to determine the dielectric properties of the layers as well as their thicknesses. The software is based on Fresnel equations and the transfer matrix formalism [111].

The change of refractive index in the range of the evanescent fields can be detected with a resolution of $\Delta n_{eff} = 10^{-7} - 10^{-5}$ [84] with this technique. The resolution is limited in the same way as the surface plasmon spectroscopy by experimental conditions e.g. temperature controller, precision of the motor position and laser noise.

Table 3.2: Dielectric constant and layer thickness using WINSPALL simulation in Figure 3.14(b) [111].

Layer	Layer thickness[nm]	ϵ'	ϵ''
Prism	∞	3.404	0
Gold	46	-12.34	1.33
PMMA	2000	2.22	0
Water	∞	1.774	0

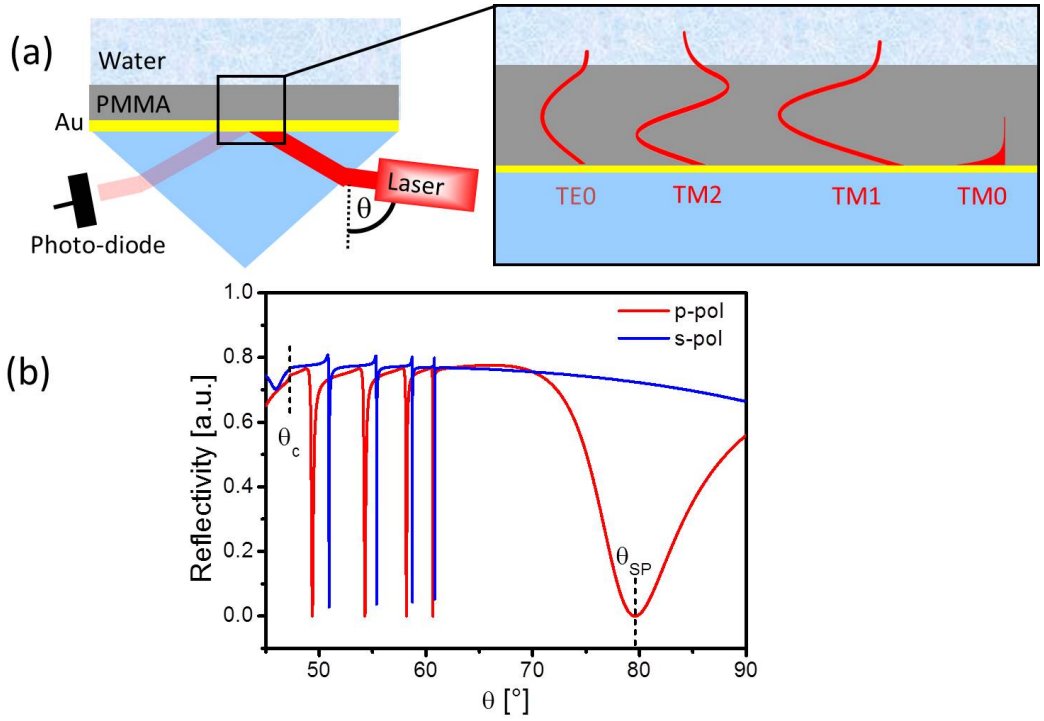

Figure 3.14: (a) Schematic presentation of metal enhanced leaky waveguide in the Kretschmann-Raether configuration with the corresponding field distribution. By using p-polarized light, transverse magnetic (TM) modes can be excited, while s-polarized light allows transverse electric (TE) modes. (b) WINSPALL Simulation (s- and p-polarization) of a 2000 nm PMMA layer on a 46 nm gold layer with critical angle θ_c and SPR angle θ_{sp} [111].

Metal enhanced leaky waveguides are nonradiative modes. The radiation losses in this technique are caused by the inhomogeneity of the leaky waveguide (PMMA layer) or the surface roughness [112]. The intensity of the evanescent fields of the metal enhanced leaky waveguide is enhanced just as in the case of the evanescent fields of the surface plasmons and total internal reflection. For the configuration in Figure 3.14(a) the intensity enhancement F $= I/I_0$ for each mode can be calculated with the help of ATSOS software [113]. One gets F ≈ 30 for the TM1 mode, F ≈ 65 for the TM4 mode and F

≈ 140 for the TE0 and TE3 mode.

In this work, I have used a TM mode to obtain the dynamics of GNRs close to a neutral surface (PMMA layer). The PMMA layer was prepared according to the procedure described in Section 3.4. Figure 3.15 shows a simulation of the normalized electrical field as a function of the penetration depth (ξ). Using WINSPALL software one can fit the reflectivity curves (inset in Figure 3.15) and obtain the thickness of the PMMA layer which was 1030 ± 10 nm [111].

With the ATSOS software [113], parameters based on those extracted from the WINSPALL fit (layer thickness and dielectric constant), the penetration depths of the evanescent field of the TM1 and TM2 mode were obtained (Figure 3.15). For the WEDLS measurements, I have used TM2 mode with a penetration depth of ξ = 345 nm.

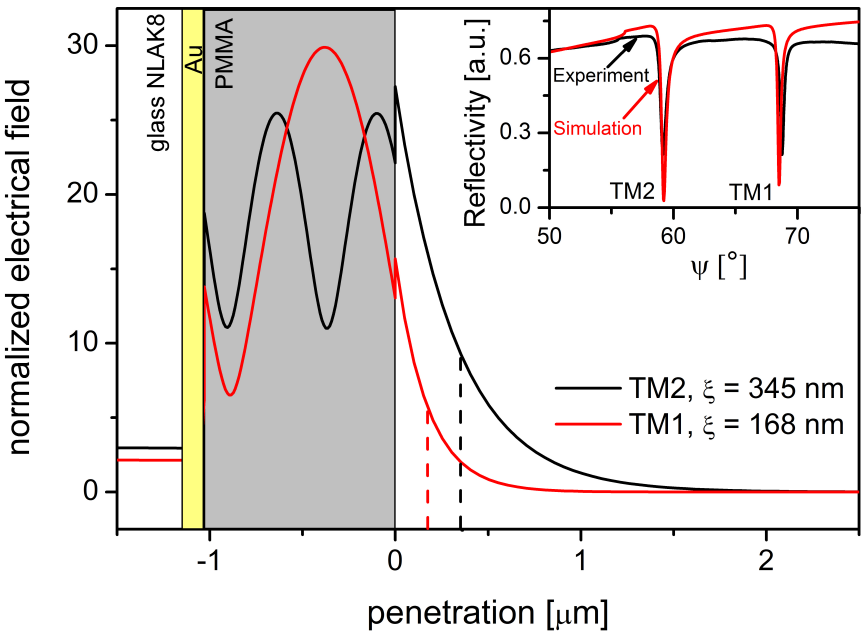

Figure 3.15: Transverse magnetic (TM) modes in a WEDLS setup simulated by ATSOS software. The vertical, broken lines represent the penetration depth ξ. Inset: TM waveguide mode spectra of the PMMA film coated on a thin gold layer on a NLAK8 glass and a simulation to obtain the parameter of the film.

Chapter 4

Results and discussion

In this chapter, I present results on nanomolar suspensions of gold nanorods (GNRs). First, I demonstrate dynamics of GNRs with Dynamic Light Scattering (DLS), a powerful method to measure the diffusion as well as the rotation of anisotropic particles in bulk solution. Second, I investigate the dynamics of a surfactant free solution of GNRs close to a wall with very high spatial and temporal resolution by using Resonance Enhanced Dynamic Light Scattering (REDLS). Third, I show the effect of the surfactant CTAB on the diffusion and rotation of GNRs in water close to a charged solid (gold) and neutral (PMMA) wall using REDLS and Waveguide Enhanced Dynamic Light Scattering (WEDLS). Finally, dynamics of spherical silica coated GNRs (SiO_2@GNRs) close to a wall and comparison of the results with GNRs and silica particles of the same size are shown.

4.1 Plasmon enhanced dynamic depolarized light scattering in bulk

Nanomolar suspensions of GNRs were analyzed by Dynamic Light Scattering (DLS) complemented by optical absorption spectroscopy. A wavelength-dependent enhancement of the anisotropic scattering as a consequence of the excitation of a longitudinal plasmon mode was observed. The strong scattering intensity near the longitudinal

surface plasmon resonance (LSPR) frequency for rods oriented parallel to the excitation optical field allowed the resolution of the translational anisotropy in an isotropic medium. Estimations of lengths and thicknesses of the GNRs from both translational and rotational diffusion coefficients were in qualitative agreement with values from transmission electron microscopy images. This wavelength-dependent anisotropic light scattering enables new applications such as probing dynamics in complex environments at a single-particle level by depolarized DLS and sorting plasmonic nanoparticles according to their size and shape by polarized microscopy [75].

4.1.1 Absorption and scattering extinction patterns

In order to quantitatively describe the absorption and scattering cross section of the GNRs, a numerical calculation using the T-matrix method (Section 2.2.1) with extended boundary conditions has been performed. This method imposes continuity at the tangential components of the electromagnetic (EM) field at the surface of the scattering moieties through appropriate surface integrals [60, 114]. The theoretical calculations have been performed by Dr. Georgios Gantzounis from California Institute of Technology (Graduate Aerospace Laboratories (GALCIT)).

The orientation-averaged scattering and extinction cross sections of an uniform distribution of randomly oriented identical particles are respectively obtained from

$$\sigma_{sc} = \frac{2\pi}{q^2} \sum_{Plm;P'l'm'} |T_{Plm;P'l'm'}|^2 \tag{4.1}$$

and

$$\sigma_{ext} = -\frac{2\pi}{q^2} Re \sum_{Plm} T_{Plm;Plm} \tag{4.2}$$

where P denotes the polarization of electric (P=E) or magnetic (P=H) type and *l,m* are the major and minor numbers of angular momentum, respectively [60, 63]. On the other hand, a monochromatic wave can be fully characterized by the Stokes parameters I, Q, U, V [63, 115]. For example, for a plane monochromatic wave, with intensity I_{0V},

incident light on a distribution of particles polarized vertically (V) to the plane of incidence, the Stokes parameters take the values (I_0, Q_0, U_0, V_0) = (I_{0V}, -I_{0V}, 0, 0), and the Stokes parameters (I, Q, U, V) of the scattered wave for a given scattering direction are calculated through the Stokes parameters of the incident wave with the help of the scattering [63] or phase matrix (I, Q, U, V) = $F(\theta)\cdot$ (I_0, Q_0, U_0, V_0) [60]. It is noteworthy that for a random distribution of particles the Stokes parameters of the distribution are just the sum of the Stokes parameters of each particle of the distribution [63]. For an uniform distribution of randomly oriented mirror-symmetric particles the Müller matrix takes the form [60, 63, 115]

$$F(\theta) = \begin{pmatrix} F_{11}(\theta) & F_{12}(\theta) & 0 & 0 \\ F_{12}(\theta) & F_{22}(\theta) & 0 & 0 \\ 0 & 0 & F_{33}(\theta) & F_{34}(\theta) \\ 0 & 0 & -F_{34}(\theta) & F_{44}(\theta) \end{pmatrix} \tag{4.3}$$

where θ is the angle between the incident and the scattered light and $F(\theta)$ can be calculated by means of the scattering T-matrix, as described in ref. [60]. The Müller matrix describes the change of intensity and polarization state of the polarized as well as unpolarized light during reflection, refraction or transmission through material.

For cylindrical symmetry, the absorption, the polarized I_{VV} and depolarized I_{VH} scattering intensities and depolarization ratio I_{VH}/I_{VV} are calculated as a function of the wavelength of the probing light. In this notation, V and H denote polarization vertical and horizontal to the scattering plane defined by the wave vectors k_i and k_s of the incident and scattered light; a polarized (V) incident laser beam is used. From the definition of the Stokes parameters, Q = $I_{VH} - I_{VV}$, and so [63, 115]

$$\frac{I_{VH}}{I_{VV}} = \frac{F_{11}(\theta) - F_{22}(\theta)}{F_{11}(\theta) + F_{22}(\theta) - 2F_{12}(\theta)} = \frac{F_{11}(\pi) - F_{22}(\pi)}{F_{11}(\pi) + F_{22}(\pi)}. \tag{4.4}$$

In the case of a spherical particle, the Lorenz-Mie identity $F_{22}(\theta) = F_{11}(\theta)$ implies that I_{VH} vanishes identically. However, for non-spherical particles $F_{11}(\theta) > F_{22}(\theta)$ and thus the depolarization ratio becomes positive.

The nanoparticle dynamics are manifested in the time fluctuations of the scattered intensity I_{VX}[q,t] (X=V,H) recorded as the autocorrelation function $G_{VX}[q,t] = \langle I_{VX}[q,t] I_{VX}[q,0] \rangle / \langle I_{VX}[q] \rangle^2$ in a dynamic light scattering measurement at a scattering wave vector |q|= |k_i-k_s|= $(4\pi n/\lambda)\sin(\theta/2)$ where n and λ are the refractive index of the solvent and the wavelength of the laser beam in vacuum. The desired relaxation function $C_{VX}[q,t] = [G_{VX}(q-t) - 1]^{1/2}$ relates to the translational and rotational motion probed with a space resolution $\sim q^{-1}$.

For the two GNRs samples with aspect ratios of 2.4 (60/25 nm) and 4.5 (45/10 nm), the peak position of the LSPR mode (Figure 4.1(a)) almost coincides with the wavelength of the lasers utilized in the scattering experiments, whereas the transverse SPR mode seems to be not very sensitive to the length variation and occurs at about 525 nm for all three GNRs. Unfortunately, the theoretical calculations are not applicable for the 135/20 nm GNRs. Therefore, I have not included the experimental absorption of 135/20 GNR in Figure 4.1. The SPR modes for the 135/20 GNRs appear at 525 nm and 1170 nm.

The four vertical lines in Figure 4.1 indicate the wavelengths of the cw lasers used for the DLS experiments. The values of the depolarization ratio I_{VH}/I_{VV} and the associated scattering intensities are shown in panels (b) and (c), respectively (Figure 4.1). The position of the absorption maxima is well captured (dashed lines) by using interpolated values for the optical constants [62], whereas the rod width and average rod length were obtained by TEM (Table 3.1 in Section 3.6), as suggested by the modeling of extinction spectra [116]. Nevertheless, an adequate description (dash-dotted lines) requires inclusion of size polydispersity.

The absorption cross section, as well as the polarized and depolarized light scattering intensities, for a polydisperse sample can be calculated by the weighted average of the intensities of the different particles in the distribution, because particles scatter incoherently [63]. To account for polydispersity in the calculations, a log-normal distribution for the diameter of the particles is used and the parameters of the distribution (mean and standard deviation) are evaluated by fitting to the experimental values (eqs. 4.5 and 4.6). It should also be mentioned that the relative intensity of the low- to high-

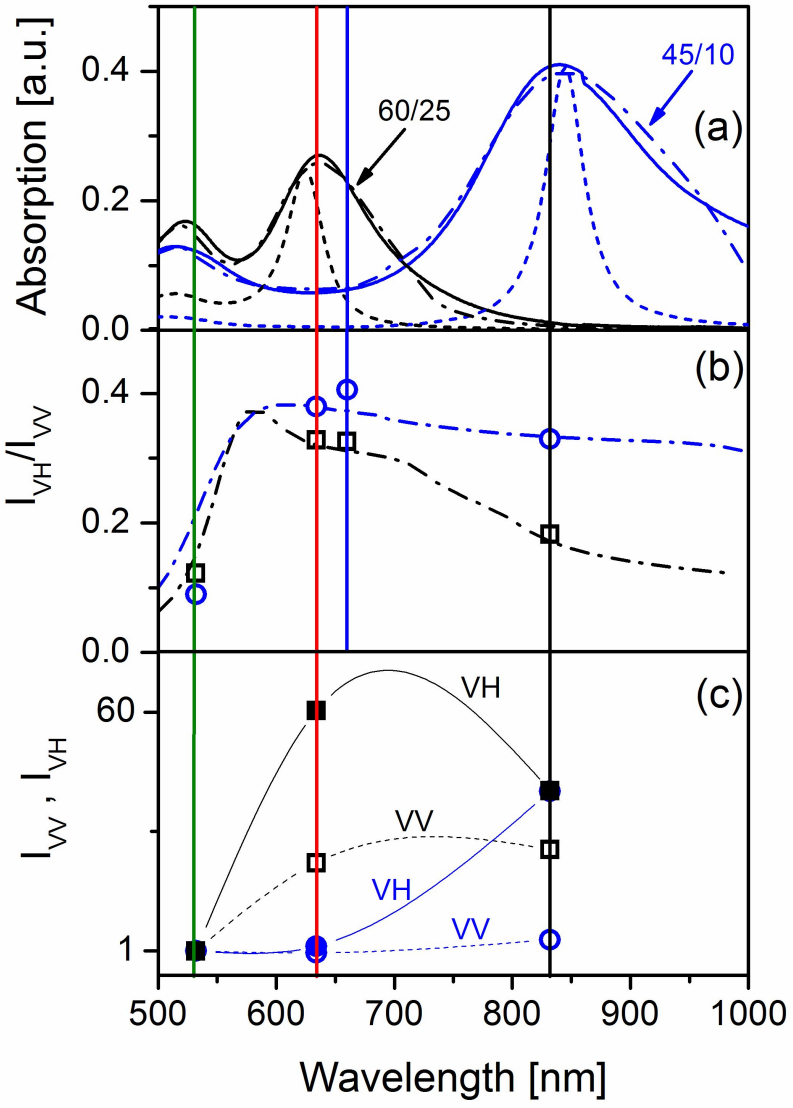

Figure 4.1: (a) Experimental (solid lines) and theoretical (dash-dotted lines) absorption spectra for two GNRs. The dashed lines represent the theoretical absorption spectra in the absence of polydispersity. (b) Depolarization ratio for the two systems depicted in panel (a), where symbols and dash-dotted lines denote the experimental and theoretical quantities, respectively. (c) Normalized (to 532 nm) polarized I_{VV} and depolarized I_{VH} light scattering intensities at four different wavelengths (vertical lines) for the systems depicted in panel (b). The data in panel (c) at 660 nm could not be included because the DLS setup was newly adjusted.

frequency absorption peak can be fitted only if an amount of nearly spherical particles of equal diameter are considered.

$$n_{\mathrm{i}} = \exp\left\{ -\frac{\left[\frac{\log(L_{\mathrm{i}})}{\mu}\right]^2}{2\log(1+\sigma)^2} \right\} \tag{4.5}$$

$$n_{\mathrm{i}} = \begin{cases} \exp\left[-\left(\frac{L_{\mathrm{i}}-\mu}{\sigma}\right)^2 \right] & L_{\mathrm{i}} > \mu \\ 0 & L_{\mathrm{i}} \leq \mu \end{cases} \tag{4.6}$$

For the 60/25 GNRs, It was considered that the sample consisted of 47% spherical nanoparticles, with the rest of the nanoparticles following a discretized log-normal distribution for the lengths $\mathrm{L_i}$ with $\mu = 56$ nm and $\sigma = 0.18$, which has been found to be efficient for similar scattering problems [117, 118]. To represent the shape of the absorption spectra of 45/10 GNRs, it is necessary to include 61% spherical nanoparticles with a discretized folded normal distribution for the lengths $\mathrm{L_i}$ with $\mu = 10$ nm (exactly spherical) and $\sigma = 8$, and with the rest of the particles following a discretized log-normal distribution (eq. 4.5) with $\mu = 46$ nm and $\sigma \approx 0.17$ nm. However, it should be noted, that this large polydispersity for the calculations is not supported by the experimental relaxation functions (eqs. 2.31 and 2.33) and the TEM images in the inset of Figure 4.7.

The peak position and the width of the LSPR peak for nanorods depend on the exact particle shape (spherical, ellipsoidally capped cylinders or rods), size and polydispersity. The latter causes a red shift and asymmetric broadening of the LSPR peak and exact form of the wavelength-dependent complex dielectric function $\varepsilon^*(\lambda)$ [116]. Because of this large number of adjustable parameters, the representation of the experimental absorption spectra is a formidable task. Even keeping the width and length of the nanorods fixed (to the TEM values), it is still necessary to include spherical nanoparticles, which affect only the position and amplitude of the transverse SPR peak. This artificial size distribution does not represent the real gold nanoparticle suspensions. Instead, these deviations should be attributed to the presence of spherically caped cylinders (TEM

images in Figure 4.7) and the change in the exact size and/or shape of the stabilizing surfactant layer covering the nanoparticles.

According to numerical calculations [116], the effect of spherocylinders on the LSPR peak might be coincidental with the effects of the rod-length size distribution. With regard to the surfactant layer, it is possible that the interaction of the plasmon polaritons with the dipoles of the surfactant layer could shift the eigenfrequencies of the plasmon polaritons, thus contributing to the broadening effect. On the other hand, the stabilizing surfactant layer could also be responsible for the broadening of the LSPR peak. In particular, polydispersity in the grafting density can dramatically affect the surface polarization [119].

The light scattering intensities, I_{VV} and I_{VH}, in Figure 4.1(b) can be calculated as the weighted averages of the intensities of the different particles in the distribution, because particles scatter incoherently [63]. The theory provides an adequate description of the absorption and depolarization data in Figure 4.1(a),(b) concurrently and corroborates the notion of an LSPR-enhanced depolarization ratio [20, 21]; it attains its maximum value at wavelengths lower than that of the LSPR as seen for 45/10 GNRs (Figure 4.1(a),(b)). However, Figure 4.1(c) shows that the maximum enhancement of I_{VH} occurs near the LSPR wavelength. This finding might be utilized for sorting nanoparticles according to their size, measuring the polarized scattering function C_{VV}[q,t] at two wavelengths (see below) and for imaging with polarized optical microscopy, relying on the strong light scattering of plasmonic nanoparticles and the aspect-ratio-dependent depolarization ratio.

If the incident wavelength is close to or at the absorption maximum, local heating of the sample could occur. To exclude thermal effects, a range of laser intensities was examined prior to the selection of the appropriate laser power assuring negligible local heating (Figure 4.2). In Figure 4.2 the correlation function of 45/10 GNRs at a wavelength of 832 nm with three different laser powers has been shown. Increasing the laser power does not influence the shape of the correlation function.

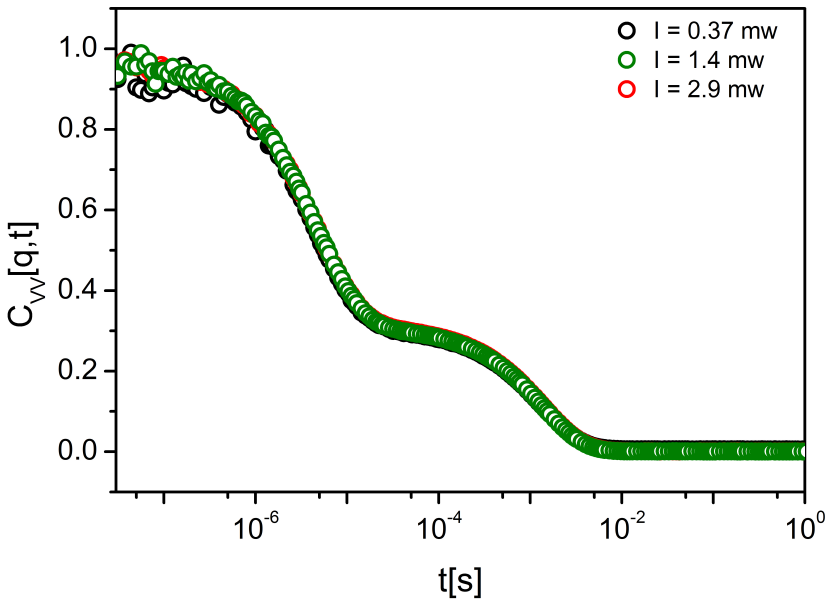

Figure 4.2: Correlation function of 45/10 GNRs at a wavelength of 832 nm with three different laser powers. The laser power does not influence the shape of the correlation function.

4.1.2 LSPR-Enhanced depolarized dynamic light scattering

As mentioned in Section 2.4.2, for anisotropic monodisperse particles the depolarization ratio $\rho > 0$ and $I_{VH}[q,t]$ fluctuates because of translational and rotational motion within a volume of the order of q^{-3}. For uncoupled dynamics of rod-like nanoparticles, $C_{VH}[q,t] = \exp(-\Gamma_{VH}t)$ and $\Gamma_{VH} = 6D_R + D_0q^2$ with D_R being the rotational diffusion coefficient and $D_0 = (D_{\parallel}+2D_{\perp})/3$ is an average of the translational diffusion coefficients along and normal to the rod axis; for small rods $6D_R >> D_0q^2$ and $\Gamma_{VH} = 6D_R$ becomes q-independent.

For a dilute solution of monodisperse spherical nanoparticles, $\rho \approx 0$ and the translational diffusion coefficient D_0 is directly obtained from the diffusive relaxation rate $\Gamma = \Gamma_{VV} = D_0q^2$ of the isotropic relaxation function $C_{VV}[q,t] = C_{iso}[q,t] = \exp(-\Gamma t)$; $I_{VV} = I_{iso}$ and $I_{VH} = 0$. But for noble spherical metal nanoparticles, it is possible to measure Γ_{VH} due to the strong anisotropic VH scattering and a q-dependent behavior has been observed [69]. Figure 4.3 shows the relaxation rate of the spherical gold nanoparticles

with a radius of 52 nm at different laser wavelengths. The laser wavelength does not have an influence on the dynamics of the spherical gold nanoparticles. In VH geometry a q-dependent behavior has been observed.

For the three GNRs, polarized and depolarized DLS measurements were performed at four different cw-laser wavelengths to access resonance effects on the anisotropic dynamic scattering. Figure 4.4 displays the polarized C_{VV}[q,t] and the depolarized C_{VH}[q,t] relaxation function for 45/10 (0.8 nM) and 60/25 (0.2 nM) GNRs at 832 nm and q = 1.31×10^{-2} nm^{-1} at 294 K. The double step C_{VV}[q,t] and the single step C_{VH}[q,t] decay functions are well described by eqs. 2.33, 2.34 and 2.31, 2.32, respectively. According to eqs. 2.32 and 2.34, the slow rate Γ_s in C_{VV}[q,t] is diffusive ($\sim q^2$) (eq. 2.34 and inset to Figure 4.4(a)), while the fast rate Γ_f (open symbols in the inset to Figure 4.4(b)) is independent of the scattering wave vector. Further, the rate Γ_f (open circles) is the same as the rate Γ_{VH} (solid circles) of the orientation relaxation function C_{VH}[q,t] in Figure 4.4(b) as seen in the inset. In agreement with eq. 2.34, this finding implies that the fast process in the VV scattering function can be identified with the rod orientational dynamics and Γ_f becomes insensitive to q-variations when $D_R \gg D_0$ according to eq. 2.32. Because of the inevitable presence of some size polydispersity that more strongly affects C_{VH}[q,t] ($\Gamma_{VH} \sim L^{-3}$) than the slow process of C_{VV}[q,t] ($\Gamma_s \sim L^{-1}$), the former is better represented by a slightly stretched exponential, $C_{VH}[q,t] = \exp(\Gamma_{VH}t)^{\beta}$, where $1 > \beta \geq 0.9$. This rather large value conforms to moderately narrow length distribution in agreement with the TEM images but is at odds with the substantial polydispersity assumed for the calculation of the absorption spectra, as mentioned in Section 4.1.1.

For polarized DLS, it is the strong I_{VH} of the plasmonic particles that renders the fast process in C_{VV}[q,t] discernible, in contrast to the established single and purely diffusive C_{VV}[q,t] for dielectric particles. Based on the absorption spectra (Figure 4.1), only the 45/10 GNRs exhibit strong extinction at 832 nm which is the reason for the larger depolarized amplitude a_f in C_{VV}[q,t] as compared to the 60/25 GNRs in Figure 4.4(a). This is in accord with the depolarization ratio and the corresponding I_{VH} and I_{VV} intensities at 832 nm in Figure 4.1(b,c). As $I_{VV}(= I_{iso} + \kappa I_{VH})$ includes both isotropic and anisotropic scattering contributions, it is the stronger increase of I_{VH} at 832 nm

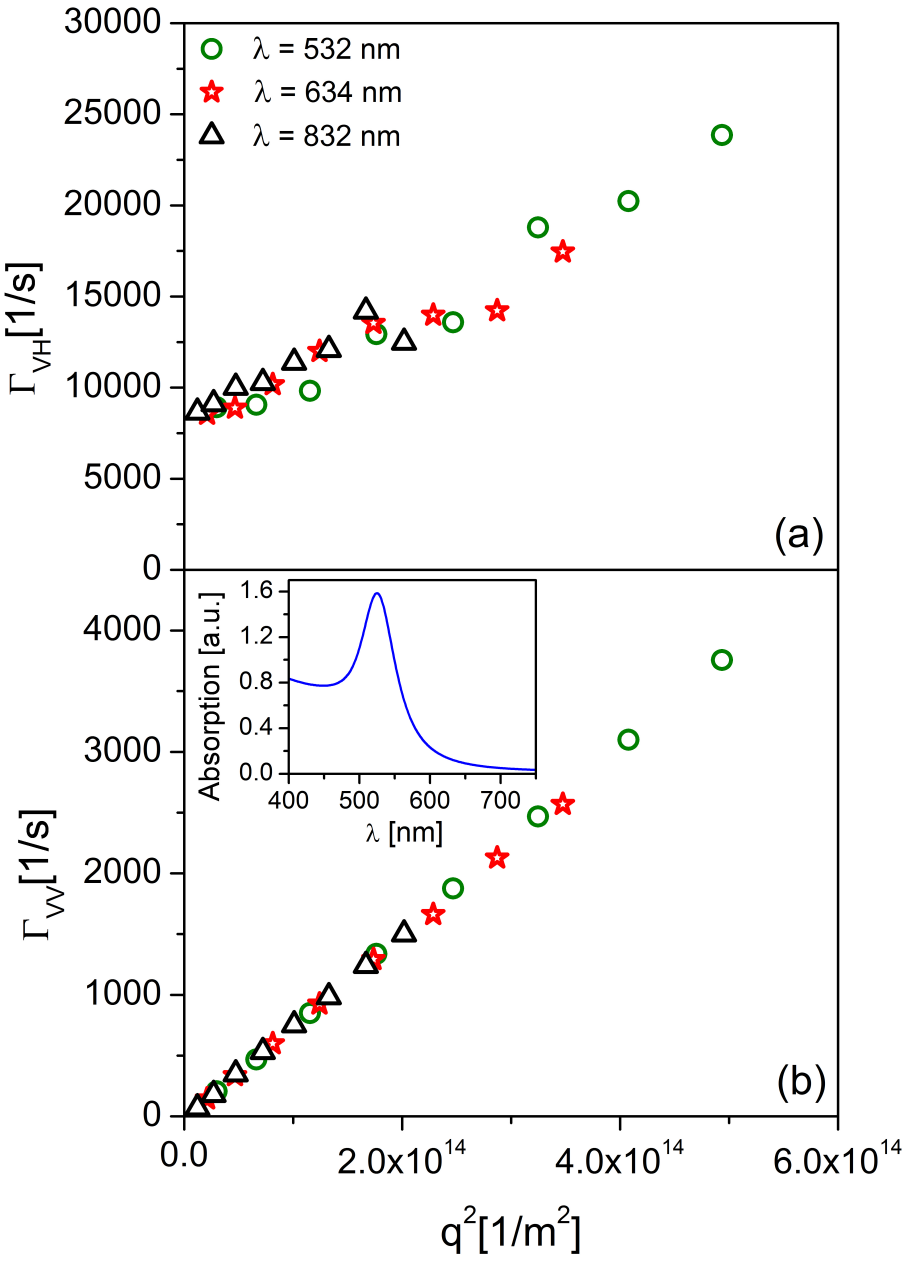

Figure 4.3: Relaxation rates Γ_{VV} and Γ_{VH} as functions of the square of the magnitude of the scattering wave vector q^2 for spherical gold nanoparticles (R = 52 nm) obtained from the corresponding C_{VV}[q,t] (a) and C_{VH}[q,t] (b) functions recorded at three different laser wavelengths: 532 nm (green circles), 634 nm (red stars) and 832 nm (black triangles). The laser wavelength does not have an influence on the relaxation rates. Inset: Absorption spectrum of the sample.

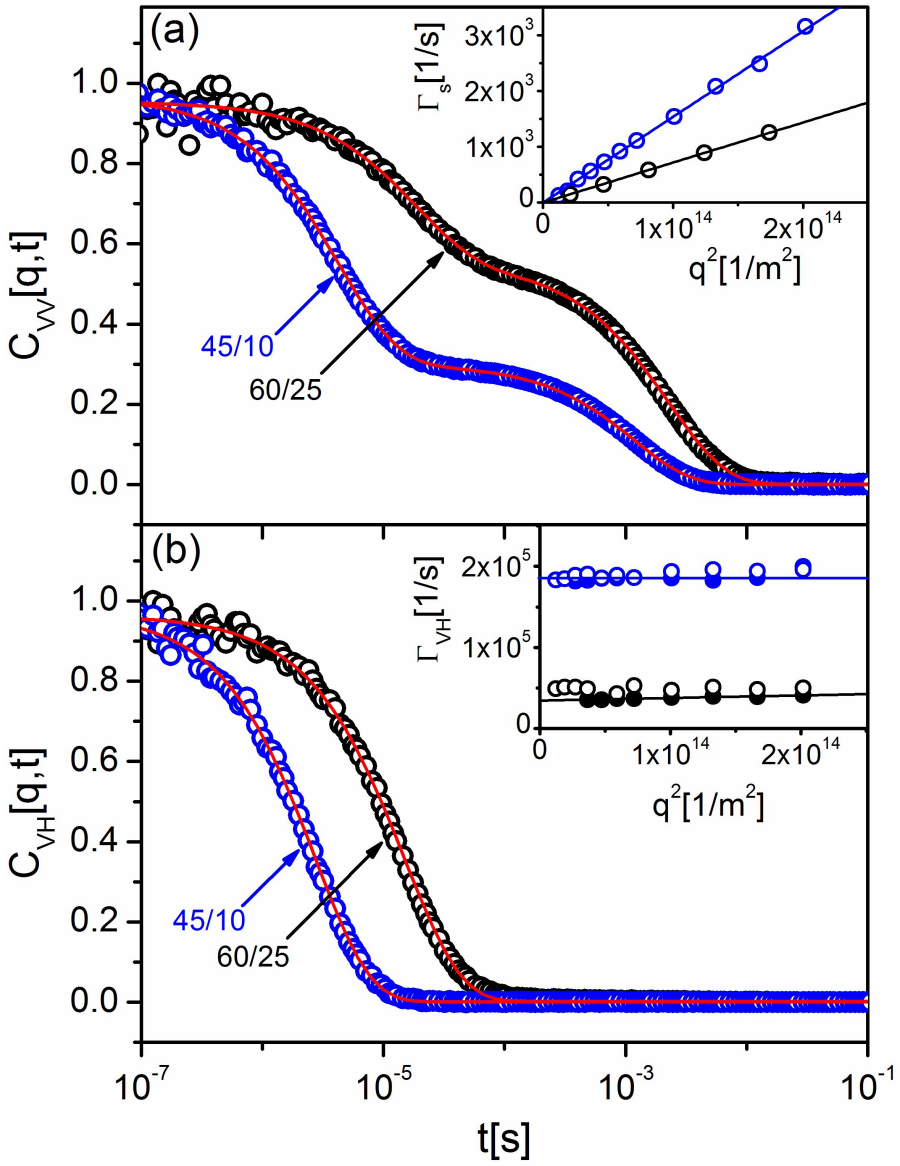

Figure 4.4: Relaxation functions of two GNR suspensions (60/25 GNRs (black circles) at 0.2 nM and 45/10 GNRs (blue circles) at 0.8 nM) at a wavelength of 832 nm and q = 1.31×10^{-2} nm^{-1}, recorded in the (a) VV (polarized) and (b) VH (depolarized) geometries. The solid lines represent the fits of eqs. 2.33 and 2.31 to the experimental functions of (a) $C_{\mathrm{VV}}[q,t]$ and (b) C_{VH}[q,t]. The rate of the slow process in the bimodal C_{VV}[q,t] function is diffusive (inset in panel (a)), whereas the orientation rate Γ_{VH} (solid circles) in the single C_{VH}[q,t] function represents a reorientation of the long axis of the GNR. In the inset in panel (b), the solid symbols denote the relaxation rate of C_{VH}[q,t], and the open symbols denote the high relaxation rate of C_{VV}[q,t].

that leads to the larger a_f/a_s ratio for the fast and slow processes in $C_{VV}[q,t]$. Hence, this amplitude ratio represents a stronger wavelength-dependent increase in I_{VH} than I_{iso}.

A consequence of the relation between depolarized light scattering and absorption for selective probing of plasmonic nanorods is examined for two mixtures of 45/10 and 60/25 GNRs with volume fraction of the short rods $\phi = 0.56$ and $\phi = 0.92$. Figure 4.5 displays the relaxation functions $C_{VV}[q,t]$ at 634 nm and 832 nm close to the LSPR of the low- (2.4) and high- (4.5) aspect ratio GNRs. The relaxation functions of the two parent solutions (solid lines) recorded at the same scattering wave vector for the two mixtures in Figure 4.5 are also displayed, for comparison. At 634 nm, the two nanoparticle solutions display similar I_{VH}/I_{VV} depolarization ratios (Figure 4.1(b)), and consequently the amplitude ratio a_f/a_s for the rotational and translational processes in $C_{VV}[q,t]$ is rather robust with respect to variations of the composition. On the other hand, the $C_{VV}[q,t]$ of the mixtures are also robust but closely resemble the $C_{VV}[q,t]$ of the low aspect ratio (60/25) nanoparticle suspension (black solid line in Figure 4.5(a)). This is, however, an expected observation as the scattering per 60/25 particle is about 70 times stronger than per 45/10 nanoparticle, because of the dependence of the VV scattering intensity on the square of the nanoparticle volume.

The variation of the I_{VH} and I_{VV} with excitation wavelength depends on the aspect ratio (Figure 4.1(c)). This dependency has two consequences for the experimental $C_{VV}[q,t]$ of the two mixtures in Figure 4.5(b). First, their dynamics become distinctly different from the $C_{VV}[q,t]$ of the low aspect ratio nanoparticle suspension (black solid line in Figure 4.5(b)) at 832 nm with increasing volume fraction of the high (45/10) aspect ratio GNR. In particular, the proximity of the fast decay of $C_{VV}[q,t]$ (associated to the rotational dynamics) to the corresponding decay in the pure 45/10 GNR suspension increases from the almost symmetric ($\phi = 0.56$) to the mixture rich in the short rods ($\phi = 0.92$). It is worth mentioning that, even in the highly asymmetric mixture, the long rods should dominate the scattering intensity. The second consequence relates to the increase of the amplitude a_f/a_s ratio with ϕ of the short GNR, notwithstanding the domination of the scattering by the long GNR. Hence this wavelength-dependent

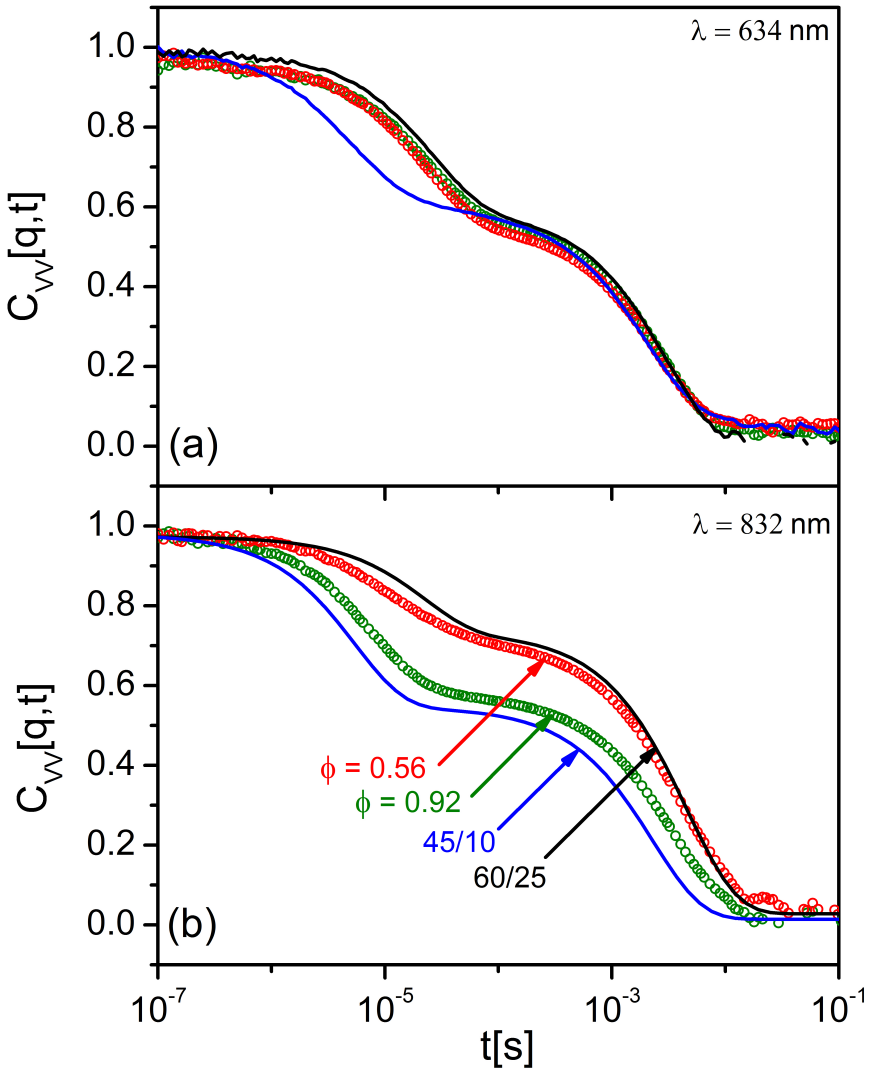

Figure 4.5: Relaxation functions in the VV geometry of 45/10 nm and 60/25 nm GNRs and their mixtures. (a) at q = 1.71 × 10^{-2} nm^{-1} and λ = 634 nm and (b) at q = 1.31 × 10^{-2} nm^{-1} and λ = 832 nm for 45/10 GNRs (blue line), 60/25 GNRs (black line), and their mixtures with 45/10 GNR volume fractions of ϕ = 0.56 (red symbols) and ϕ = 0.92 (green symbols).

increase in a_f/a_s of the short rods is a nontrivial finding as seen by the virtually ϕ-independent shape of C_{VV}[q,t] at 634 nm in Figure 4.5(a). Both amplitudes a_f, a_s include contributions from both GNRs depending on the excitation wavelength.

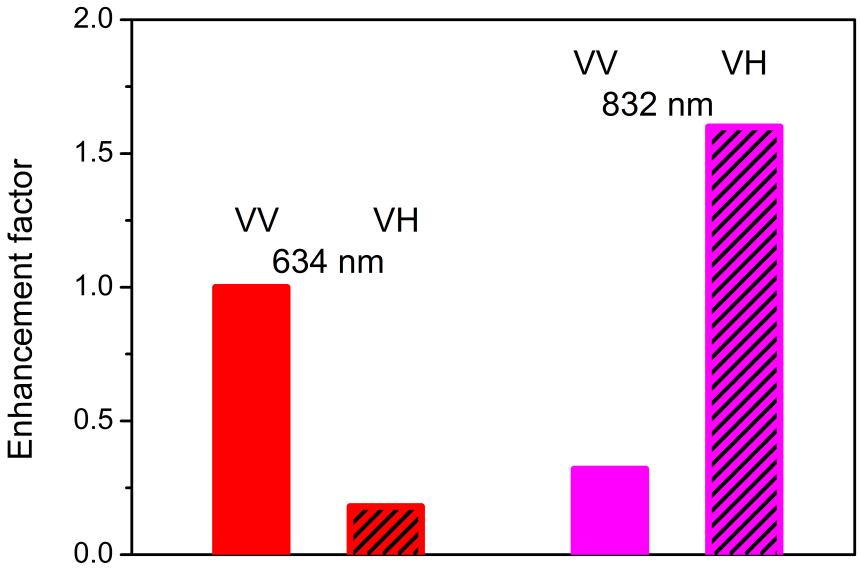

Figure 4.6: LSPR-enhanced dynamic depolarized light scattering from an equimolar mixture of 45/10 and 60/25 GNRs. The enhancement factors for the two scattering polarizations (normalized to the corresponding value for the polarized component at 634 nm) are shown for 634 and 832 nm, at which the LSPR approximately assumes its maximum for 65/20 and 45/10 GNRs, respectively. The enhancement was defined as the ratio of the sum of the amplitudes of the two fast processes to the sum of the amplitudes of the two slow processes corresponding to the two individual GNRs for VV scattering and as the ratio of the amplitude of the fast process to the amplitude of the slow process for VH scattering.

A quantitative analysis is feasible because of the sufficiently different dynamics of the two GNRs and involves a representation of the C_{VV}[q,t] by four (two for each GNR) exponential processes. Nevertheless, this is only a three parameter fit, as the relaxation rates can be fixed to their values in the pure GNR solutions and the sum of the four amplitudes is normalized to the short time intercept of the relaxation function. In the case of C_{VH}[q,t], the fit involves two relaxation processes representing the rotational diffusion of the two types of GNR. The two orientation relaxation times were fixed to the values of the individual pure GNR solutions.

For the VH depolarized geometry, the LSPR enhancement factor is defined as the amplitude ratio a_H/a_L of the high- and low-aspect-ratio GNRs. For the VV polarized scattering geometry with a contribution (κI_{VH}) of depolarized scattering, the LSPR enhancement is defined as the ratio $({a^f}_H+{a^f}_L)/({a^s}_H+{a^s}_L)$ of the total fast anisotropic (f) and slow isotropic (s) contributions. Figure 4.6 visualizes the stronger LSPR enhancement for the dynamic depolarized scattering relatively to the polarized light scattering from the 45/10 GNRs near its LSPR wavelength at about 850 nm. This finding can be applied for selective size/shape probing in complex environments and development of novel microscopy techniques.

4.1.3 Transport coefficients and translational diffusion anisotropy

In the absence of local heating, both the rotational and translation diffusion coefficients should be independent of the wavelength of the incident laser light. Figure 4.7 displays the q dependence of the slow relaxation rate Γ_s, and the single Γ_{VH} of the dynamic polarized and depolarized light scattering experiment, respectively. In fact, the GNRs with aspect ratio L/d = 2.4 conforms to the anticipated behavior; that is, both D_R and D_0 are relatively insensitive to the variation of the excitation wavelength. For the GNRs with L/d = 4.5, however, D_0 becomes faster when measured at 832 nm, near to the LSPR wavelength, whereas the rotational diffusion is independent of the excitation wavelength.

Two obvious explanations arising from either local heating and/or rod-length polydispersity are disproved. Local heating could, in principle, arise from the enhanced absorption of GNR near LSPR frequencies and absorption of water at $\sim$ 760 nm due to overtones. The latter is rather weak and it would also affect the short (60/25) GNRs. Heating near LSPR frequencies is also ruled out because there is no effect on the rotational coefficient D_R and the scattering functions were recorded at different laser powers. The polydispersity issue is conceivable through the SPR-enhanced light scattering mechanism, which sorts GNRs according to their aspect ratio. Based on the TEM

image, the 45/10 GNRs with an average aspect ratio of 4.5 is near resonance at 832 nm (Figure 4.1(a)).

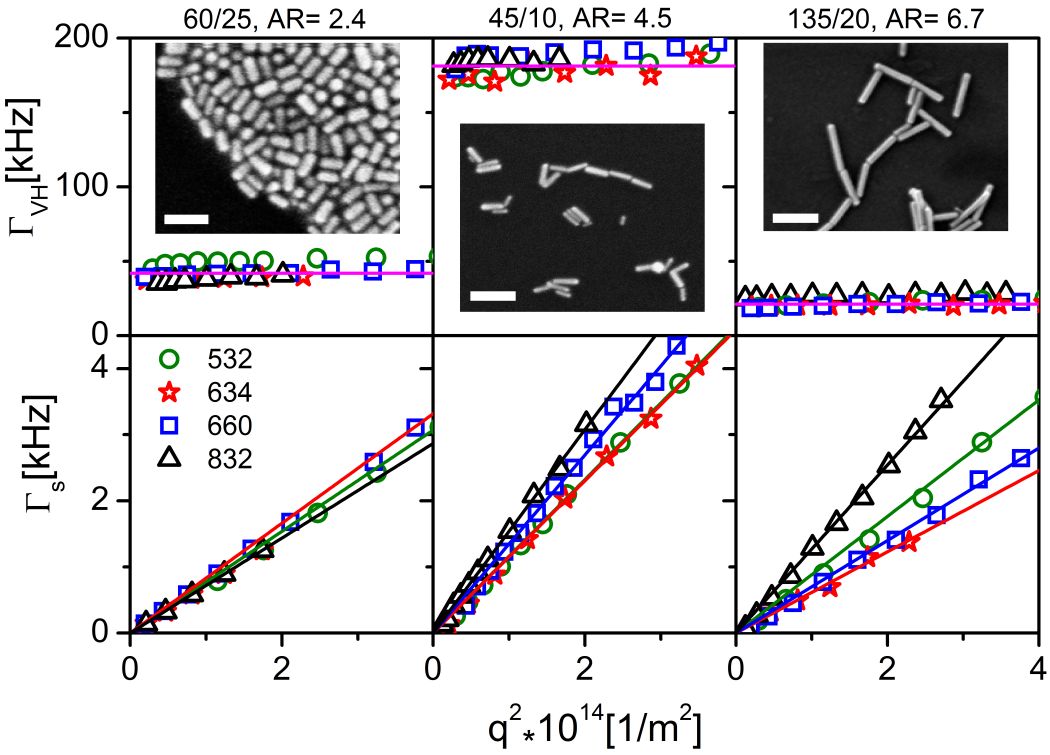

Figure 4.7: Relaxation rates Γ_s and Γ_{VH} as functions of the square of the magnitude of the scattering wave vector q^2 for 45/10 (AR = 4.5), 60/25 (AR = 2.4), and 135/20 (AR = 6.7) GNRs obtained from the corresponding C_{VV}[q,t] and C_{VH}[q,t] functions recorded at four different laser wavelengths: 532 nm (green circles), 634 nm (red stars), 660 nm (blue squares), and 832 nm (black triangles). The solid lines in the Γ_s plots represent the fits of eq. 2.34, whereas the lines in the Γ_{VH} plots represent the averages of the Γ_{VH} values from measurements at different q values. Inset: TEM images of the three types of GNRs (scale bars = 100 nm).

For rod-like particles, the ratio $D_{\parallel}/D_{\perp} = 1$, and hence the ratio $D_{\parallel}/D_0$ to the average D_0 increases with aspect ratio. To increase $D_{\parallel}/D_{\perp}$, the 135/20 GNRs with larger aspect ratio (L/d = 6.7) have been examined and found a LSPR redshift to about 1170 nm. According to Figure 4.7 (triangles), this system shows a larger wavelength dependent increase than for 45/10 GNR, despite the off-resonance situation for an average L/d value of 6.7. For 135/20 GNR, however, the width of the aspect ratio distribution (from the TEM images in the inset in Figure 4.7) is twice that for the other two types of GNRs. Therefore, an explanation consistent with the 45/10 GNRs might be the presence of

a significant population of particles with AR $\approx$ 5 in the 135/20 system. In the same context, the much narrower distribution of 60/25 GNRs excludes the presence of GNR with AR $\approx$ 5 and, hence, the absence of excitation wavelength dependence on the excitation wavelength.

To resolve the two components $D_{\parallel}$ and $D_{\perp}$, a biased probing of nanorods with orientation along the polarization of the incident laser field is required. This occurs close to the LSPR frequency [10], where the scattering cross section is large and its spatiotemporal fluctuations decay via diffusion along the nanoparticles axis. For shorter laser wavelengths, off-resonance leads to the measurement of the average D_0 translational diffusion. Thus, LSPR can reveal translational anisotropy in an isotropic solution of nanorods.

The analysis of non-spherical colloids has attracted interest in recent years [120,121]. D_0 and D_R parallel to a solid surface for spheres and colloidal clusters of spheres of relatively large size (2-9 μm) was found to change differently with size and shape and their relation is not accounted by the Stokes-Einstein-Debye (SED) equation for spheres [121]. The complex hydrodynamic conditions, due also to the particle symmetry renders the translational-rotation decoupling a challenging task.

Access to three transport coefficients increases the reliability of the size and shape characterization of the GNRs. The rotational diffusion motion about the rod axis described by D_R is independent of the wavelength of the laser radiation for the two short GNRs. This is a rather expected observation considering the vastly faster rotational dynamics (e.g. AR = 4.5 in Figure 4.7), thereby excluding coupling to translational dynamics. For the higher-AR (135/20) GNRs, however, a careful inspection of the much lower Γ_{VH} in Figure 4.7 unravels about 15% faster when probed at 832 nm than at shorter wavelengths. The values of the two transport coefficients D_0 and D_R for the three types of GNRs at off-resonance conditions and the translational anisotropy $D_{\parallel}/D_0$ (for 45/10 and 135/20 GNRs) are listed in Table 4.1. Under the common assumption of stick boundary conditions and cylindrical shape (used for the description of the absorption spectra), I first searched for the best values of length (L) and diameter (d) describing D_0 and D_R and then proceeded with $D_{\parallel}/D_0$. For cylindrical shape rods, the analytical

Table 4.1: Translational and rotational transport coefficients of three GNRs with aspect ratios L/d obtained from DLS using different excitation wavelengths

L/d(AR)	λ[nm]	$D_T \times 10^{-12}$ [m^2s^{-1}]	$D_\parallel \times 10^{-12}$ [m^2s^{-1}]	$D_\parallel/D_T$	$D_R \times 10^3$ [s^{-1}]
60/25(2.4)	$532-832$	7.6 ± 0.3			6.7 ± 0.6
70/32[a](2.2)		9.2	9.7	1.0	6.8
45/10(4.5)	$532-660$	12.4 ± 0.4			30 ± 1.3
	832		15.6 ± 0.5	1.3 ± 0.1	
56/13[a](4.3)		16.3	19.0	1.2	24.9
135/20(6.7)	$532-660$	7.3 ± 0.8			3.3 ± 0.7
	832		12.7 ± 0.6	1.7 ± 0.2	
124/19[a](6.7)		9.0	10.8	1.2	3.2

[a] From eqs. 4.7, 4.8, 4.9 and 4.10.

expressions D_0, D_R, $D_\parallel$ and $D_\perp$ are valid in the range $2 < L/d < 20$. The expressions were used for the calculation of transport coefficients for three GNRs (Table 4.1) and are given by [74]:

$$D_0 = (k_B T/3\pi\eta L) \times T(L/d) \tag{4.7}$$

$$D_R = (3k_B T/\pi\eta L^3) \times R(L/d) \tag{4.8}$$

$$T(L/d) = \ln(L/d) + 0.312 + 0.565(L/d)^{-1} - 0.1(L/d)^{-2} \tag{4.9}$$

$$R(L/d) = \ln(L/d) - 0.662 + 0.917(L/d)^{-1} - 0.05(L/d)^{-2} \tag{4.10}$$

$$D_\parallel = (k_B T/2\pi\eta L) \times \ln(L/d) - 0.207 + 0.980(L/d)^{-1} - 0.133(L/d)^{-2} \tag{4.11}$$

$$D_\perp = (k_B T/4\pi\eta L) \times \ln(L/d) + 0.839 + 0.185(L/d)^{-1} + 0.233(L/d)^{-2} \tag{4.12}$$

From eqs. 4.7 and 4.8, the ratio of the model-dependent functions of the aspect ratio is

$$R(L/d)/T(L/d) = (D_R/D_0)(L^2/9). \tag{4.13}$$

In Table 3.1 of Section 3.6, the length (L) and diameter (d) of GNRs reported by the supplier and determined by TEM using software program *ImageJ 1.45s* have been shown. In Table 4.2, length (L) using eqs. 4.13 and analytical expressions 4.7, 4.8, 4.9, 4.10 are provided.

Both T(L/d) and R(L/d) are very weak functions of the aspect ratio and hence their ratio is quite robust to L/d variations as seen in Figure 4.8 (blue line, R/T). Equation 4.13 is then suitable for the estimation of the rod length L which, in turn, is used to determine T(L/d) and R(L/d) from eqs. 4.5 and 4.6 using the solvent (water) viscosity. The cylinder length L assumes 65 nm, 45 nm and 109 nm using aspect ratios 2.4, 4.5 and 6.7 from which only 45/10 GNR shows larger (beyond the error $\sim 8\%$) deviations from the TEM value (Table 4.2): L_{TEM}: 68, 55, 117 nm with aspect ratios of 2.5, 5, and 6.5, respectively.

Table 4.2: Lengths (L) and diameters (d) of three GNRs with different aspect ratios (L/d) including theoretical values

	reported by supplier			determined by TEM[a]				
Samples	L[nm]	d[nm]	L/d	L[nm]	d[nm]	L/d	L[b] (eq. 4.13)	L^c_{calc}
60/25	58	25	2.3	68	27	2.5	65 ± 3	70
45/10	44	10	4.4	54	11	4.9	45 ± 2	56
135/20	134	20	6.7	117	18	6.5	109 ± 9	124

[a] Error of 8% for L and 20% for d. [b] Refs. [122, 123]. [c] See Table 4.1 (error $\approx 20\%$).

To verify the self-consistency of the L estimation, the values of T(L/d) computed from eq. 4.7 are shown in Figure 4.8 (open squares), along with the values of R/L (open circles) which, as expected, fall within less than 1% of the theoretical R/T ratio (solid blue line) that was assumed to calculate L. However, the experimental T(L/d) values are significantly lower than the theoretical T(L/d) curve, and forced agreement through a shift along the L/d axis to overlap with the dashed and solid lines in Figure 4.8, is not feasible and, moreover, not achievable with realistic d values. Instead, the deviation might arise from the assumed cylindrical shape, possibly hydrodynamic boundary conditions, and/or validity of the model; a similar deviation from the TEM values was also

recently reported [74]. One should probably approach the problem numerically, solving the Stokes equation around a cylinder for a prescribed aspect ratios and different hydrodynamic conditions [121].

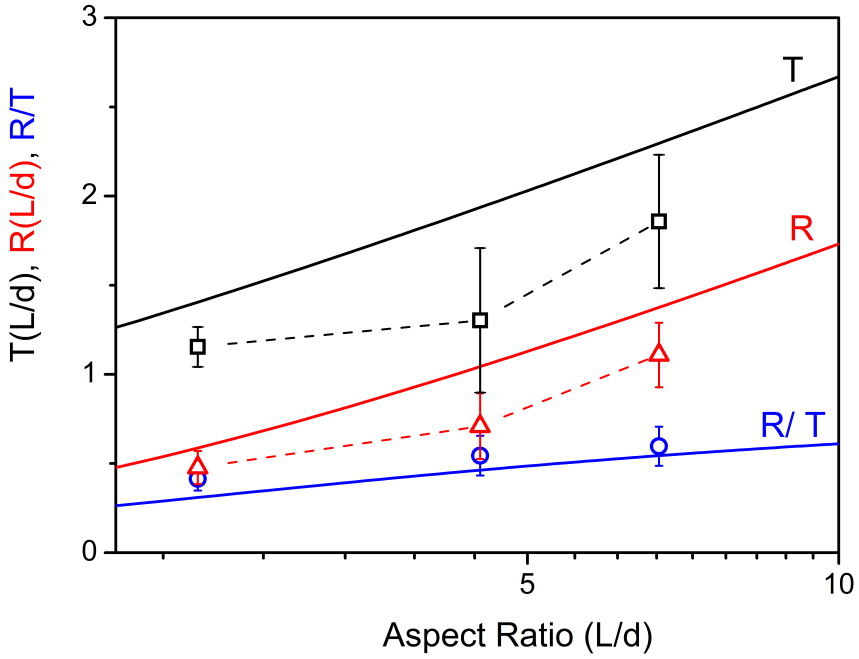

Figure 4.8: Translational, T(L/d), and rotational, R(L/d), functions and their ratio (R/T) as functions of the aspect ratio either computed for cylindrical rods using eqs. 4.9 and 4.10 (solid lines) or estimated from eqs. 4.7 and 4.8 (open symbols) using the values of L (65, 45, and 109 nm) obtained from eq. 4.13 for the corresponding aspect ratios (2.4, 4.5 and 6.7, respectively).

Despite the semiquantitative description, the resolved translational anisotropy near the LSPR frequencies can be captured for cylindrical shape under stick boundary conditions (eqs. 4.7, 4.8, 4.9, 4.10 and 4.13). Under this assumption, use of the L and d values listed in Table 4.1 led to an overestimation ($\sim$ 25%) of D_0 and an underestimation of the translational anisotropy $D_{\parallel}/D_0$, but captured D_R with exception of the 45/10 GNRs; using the values of L obtained from eq. 4.13 led to even larger deviations from the experimental D_R values. The values of L obtained by means of TEM and DLS through either eq. 4.13 (independently of the solvent viscosity) or the simultaneous representation of all three transport coefficients (Table 4.1) define the range within which the actual values might fall. A more precise estimation requires simulation work

which was outside of the scope of this work.

4.2 Dynamics of MTAB stabilized gold nanorods (MTAB-GNRs) near a wall

I measured the rotational and translational diffusivity of dilute MTAB stabilized gold nanorods (MTAB-GNRs) (60/25 nm, AR = 2.4) in aqueous suspension close to a hard planar wall. Therefore, Resonance Enhanced Dynamic Light Scattering (REDLS), an evanescent technique, was applied, making use of the strong scattering intensity near the longitudinal surface plasmon resonance (LSPR) frequency of the particle. I observed a slowing down beyond the known hydrodynamic models. The functionalizing of GNRs with MTAB is described in Section 3.1.2. In the following, I will present the major experimental results.

4.2.1 Translational and rotational diffusion of MTAB-GNRs

The basic experimental technique in REDLS is dynamic light scattering measuring field auto correlation functions of scattered light to extract, via the characteristic times of these functions, the dynamic behavior of systems studied. The difference to DLS is the exciting electromagnetic field or coherent light source; it is the evanescent part of a surface plasmon travelling along the surface of a noble metal interface. Apart from the finite penetration depth of this field away from the interface and its influence on the q-behavior of relaxation times, the rules of DLS apply as summarized in Section 2.4.2. In Section 2.6.2, the anisotropic diffusion near solid wall is described. The measured relaxation rate can be rewritten as [88]

$$\Gamma_c = \left(\left\langle D_{\parallel} \right\rangle (\xi) q_{\shortparallel}^2 + \left\langle D_{\perp} \right\rangle (\xi) (q_{\perp}^2 + \frac{1}{\xi^2}) \right) \tag{4.14}$$

with $q_{\parallel,\perp}$ being the components of the magnitude of the scattering vector q and $D_{\parallel,\perp}$ the mean diffusivities parallel and perpendicular to the surface. ξ is the penetration depth of the evanescent wave. In order to fit the relaxation rate Γ in the plot Γ_c vs. q^2 for

the measurement close to the wall, I have derived the $q_{\parallel,\perp}$ in eq. 4.14 as a function of q starting from existing relaxation rate Γ in the literature (eq. 4.14) [88]. The relaxation rate Γ_c can then be rewritten as

$$\Gamma_c = \left(\left\langle D_{\parallel} \right\rangle (\xi)(\frac{q^2}{2.64 \times 10^7})^2 + \left\langle D_{\perp} \right\rangle (\xi)(q^2(1 - \frac{q^2}{(2.64 \times 10^7)^2}) + \frac{1}{\xi^2}) \right), \tag{4.15}$$

where $q = (4\pi n/\lambda_0) \sin(\theta/2)$. By using $n = 1.33$ and $\lambda_0 = 632.8$ nm, $\sin(\theta/2)$ is equal to

$$\sin(\theta/2) = \frac{q}{2.64 \times 10^7}. \tag{4.16}$$

The $q_{\parallel}$ and $q_{\perp}$ can then be written as

$$q_{\parallel} = \frac{q}{\sin(\theta/2)} = \frac{q^2}{2.64 \times 10^7} \tag{4.17}$$

and

$$q_{\perp}^2 = q^2 - q_{\parallel}^2 = q^2 - \left(\frac{q^2}{2.64 \times 10^7} \right)^2 = q^2 \left(1 - (\frac{q}{2.64 \times 10^7})^2 \right). \tag{4.18}$$

As discussed in Section 3.2, the adsorption of the GNRs onto the gold layer can be prevented by functionalizing the gold layer with 2-aminoethanethiol (cysteamine). To check for the differences in interactions between MTAB-GNRs and gold layer with and without a cysteamine layer, surface plasmon resonance (SPR) scans have been used. The SPR part of the experiments allows monitoring possible adsorption of the GNRs to the surface during the REDLS measurements. A complete scan performed by SPR measurements before and directly after the REDLS measurements shows the possible extent of adsorption. But even during the REDLS experiment an adsorption leads to a shift of the resonance minimum and thus to a strong change in scattered intensity. Thus, a change of the system during the REDLS experiments can be monitored.

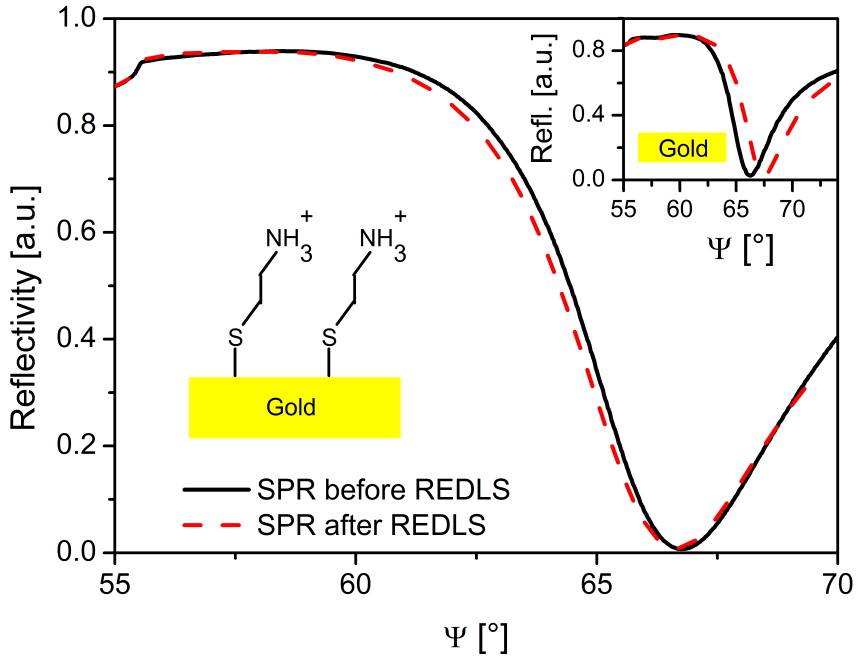

Figure 4.9: Reflectivity scans on a cysteamine-functionalized gold layer before (full lines) and directly after (dashed lines) injection of the MTAB-GNRs. After the REDLS measurements no shift of the resonance curve is visible. Thus, no adsorption of MTAB-GNRs on the cysteamine-functionalized gold layer took place. Inset: reflectivity scans on a non-functionalized gold surface.

Figure 4.9 shows reflectivity scans before (full lines) and directly after (dashed lines) REDLS measurements. The full lines cannot be distinguished in Figure 4.9 since the very small amount of particle leads to an almost negligible shift in refractive index and thus to an almost negligible shift in position of the resonance. Using a cysteamine-functionalized gold substrate (aminogroup-terminus) no visible shift is detected even after two weeks of measurements. However, for the not functionalized gold surface, MTAB-GNRs were adsorbed on the gold surface causing shifts in the angle of incidence for surface plasmon excitation (inset in Figure 4.9).

In Figure 4.10, the normalized field autocorrelation functions measured by REDLS and DLS are compared. In polarized (VV) geometry two relaxation modes can be seen for both measurements similar to the results in refs. [22, 75] and discussed in Section 4.1. The first mode, henceforth called fast process, is related to the rotation of MTAB-GNRs. It is well known that the relaxation rates of the VH correlation functions and

fast process in VV correlation functions are dominated by rotational diffusion [75]. The second mode, henceforth referred to as slow process, is related to translational diffusion. The shape of the autocorrelations function measured with polarized scattered

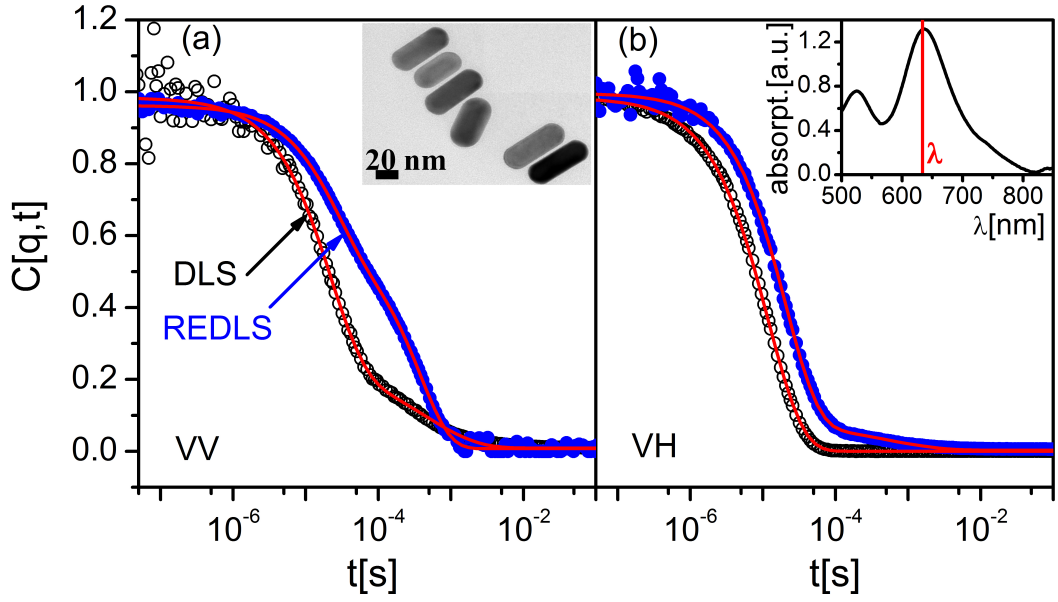

Figure 4.10: Normalized field autocorrelation function C[q,t] for diffusion near a gold surface from REDLS (blue full circle) and from DLS measurements in bulk (black open circle) in VV and VH geometry at a scattering angle of 90° (q= 0.019 nm^{-1}). The solid lines denote the fits of eqs. 2.31 and 2.33 to the experimental C_{VH}[q,t] in (b) and C_{VV}[q,t] in (a), respectively. Insets: in (a) TEM image of MTAB-GNRs. In (b) absorption spectrum of MTAB-GNRs (60/25 nm) with the vertical, full line marking the incident wavelength close to the maximum of the absorption.

light C_{VV}[q,t] by REDLS was similar to the shape of C_{VV}[q,t] in DLS. However, close to the wall for C_{VV}[q,t] the amplitude ratio $a_f/a_s = I_{VH}/I_{iso}$ changes (Table 4.3). The decay rate slows down in both VV and VH geometries (blue full circle in Figure 4.10). This slowing down is attributed to the presence of the solid wall which leads to the anisotropic diffusion [25, 77, 124] and is included in the theory (eq. 4.14). As I_{VV}(=I_{iso}+κI_{VH}) includes both isotropic and anisotropic scattering contributions, it is the strong I_{VH} of plasmonic anisotropic particles at 634 nm that makes the anisotropic signal visible even in VV scattering geometry.

Scattering intensities measured with DLS and REDLS in VV geometry were fitted with equation 2.33. In the case of VH geometry, I have used equation 2.31 for DLS data.

For REDLS, I have used two exponential functions (eq. 2.33) and kept the values of relaxation time from the translational process in VV geometry fixed. The reason is, that for REDLS in VH geometry I observed a slow correlation with low amplitude starting at 10^{-4} s (Figure 4.10). It is comparable with the translational relaxation time observed in VV geometry. So even by using a polarizer with extinction coefficient of 10^{-8} (B. Halle, Germany) part of the VV signal was detected in VH geometry.

To screen the electrostatic interactions between the positively charged gold wall and the GNRs, NaCl salt with two concentrations (0.1 mM, 0.5 mM) has been used. In Table 4.3, total intensities of the MTAB-GNRs in bulk and close to the wall are compared. I_{iso} and I_{VH} are computed from the contract of the correlation function multiplied by the scattered intensity.

Table 4.3: Total intensities (I_{tot}) of isotropic scattering in polarized (I_{iso}) and depolarized (I_{VH}) scattering at q= 0.019 nm^{-1} and depolarization ratio (I_{VH}/I_{iso}) of the MTAB-GNRs in bulk and close to the wall.

	DLS			REDLS		
NaCl [mM]	I_{iso} [kHz]	I_{VH} [kHz]	I_{VH}/I_{iso}	I_{iso} [kHz]	I_{VH} [kHz]	I_{VH}/I_{iso}
0	5.25	1.89	0.36	0.04	0.01	0.20
0.1	5.50	1.94	0.35	0.07	0.02	0.29
0.5	5.50	1.89	0.34	0.33	0.08	0.25

Looking at the intensities of I_{iso} and I_{VH} contributions I find a much weaker polarized and depolarized signal in REDLS compared to DLS (Table 4.3). This can be attributed to the roughly 1000 times smaller scattering volume in REDLS compared to DLS. In REDLS the scattering volume is defined by the area defined by the footprint of the laser times the penetration depth of the evanescent light of only 200 nm.

The increasing salt concentration has no effect on the intensities in DLS, but in REDLS the intensity increases linearly with the salt concentration.

According to light scattering theory I_{VV} contains two parts [69]: the isotropic scattering plus a depolarized contribution ($I_{iso}+ \kappa I_{VH}$). While I_{iso} is connected to the translational diffusion, I_{VH} contains the rotational or reorientation part of diffusion. Adding salt has no effect on the ratio comparing results for DLS and REDLS measurements. The total intensity is for both scattering polarizations a function of the number of scattering

particles. In I_{iso} further major contributions stem from the density fluctuation caused e.g. by the difference in refractive index between the moving particle and the solvent as well as from the dependence on the square of the volume of this particle. I_{VH} has as major contribution the absolute value of the polarizability tensor of the particle. Neither the volume nor the polarizability of the particle is likely to change by the presence of a wall nor will the refractive index of either solvent or particle change considerably. Considering possible changes in the MTAB layer, I have to conclude that due to the covalent bonding of this stabilizing agent only small changes should be possible and I expect no change in volume or polarizability of the particle in a considerable amount. Out of these reasons I state that this change in total intensities must originate from the number of particles taking part in the motions described above.

The signal, i.e. the intensity, stemming from rotation in REDLS is about 50% smaller as can be seen by the depolarization ratio I_{VH}/I_{iso}. This decrease is independent of salt concentration, since within one set of results from one experimental method the depolarization ratio does not change.

While the total intensities show a difference between motions close to a wall (REDLS) and motion in the bulk solution (DLS), the distribution of relaxation times is not as strongly affected. In DLS an almost monodisperse behavior is detected with β values close to one. A slightly broader distribution was found in the REDLS measurements, where $0.8 < \beta < 0.9$, independent of the salt concentration. This broadening of relaxation times is caused by the fact that by REDLS particles at different distances from the wall are detected. Depending on their distance, they have different diffusion coefficients, due to hydrodynamic coupling with the wall. Therefore, a distribution of diffusion coefficients is recorded.

In evanescent light scattering the depth dependence of the results is worth venturing into to gain more information. Unfortunately, in REDLS one is confined, for one set of parameters as laser wavelength and materials used, to one excitation angle of the surface plasmon and thus to one penetration depth. Another feature to look at is the short range or localized plasmon on the particle themselves which can interact with the gold layer. This can lead to a considerable redshift if the particle-interface distance is

of the order of 10 nm [125, 126]. Due to the high dilution of particles and the repulsion from the wall the probability for a particle to be in this distance-range is small. I did not observe any redshift in the experiment.

To analyze the translational motion of MTAB-GNRs, the q-dependence of the characteristic relaxation rate Γ (q) was used. For particles diffusing in bulk solution, I obtained a linear q^2-dependence of Γ (q). The slope is equal to the translational diffusion coefficient D_0 (black open circle in Figure 4.11(a)). In agreement with previous studies [75], the Γ_{VH} becomes insensitive to q-variations when $D_R >> D_0$ according to equation 2.32, which was observed for both DLS and REDLS measurements (Figure 4.11(b)). With REDLS a change of slope of Γ(q)-vs-q^2 was observed (blue full circle in Figure 4.11). This slow-down can be attributed to the hindered anisotropic motion of GNRs close to a surface. Using the theoretical prediction for $\left\langle D_{\parallel,\perp} \right\rangle / D_0$ (eq. 4.15) I can qualitatively describe the experimental Γ_{VV} for the MTAB-GNRs (dashed line in Figure 4.11(a)) for an apparent hydrodynamic radius (R_h) of 26 nm as found from bulk DLS measurements. However, this model is derived for the isotropic particles close to a wall.

A positively charged GNR diffusing near a positively charged wall experiences a repulsive electrostatic force. This force slows down the GNR diffusion and also contributes to the anisotropy discussed above. The electrostatic interactions between two charged bodies in a medium containing free charges or ions (e.g. an aqueous electrolyte solution), are screened by the free charges. The net electrostatic double-layer interaction decays roughly exponentially with a characteristic length called the Debye length κ^{-1}. For water with added symmetric monovalent electrolyte at room temperature, the Debye length κ^{-1} (in nm) can be given by the expression $\kappa^{-1} = 0.304/\sqrt{I}$, where I is the ionic strength of the electrolyte and is expressed in M or mol/l. Electrostatic interactions in the experiments are screened using NaCl salt to some extent within the experimental limit of no aggregation. Any presence of agglomeration with adding NaCl was negligible for REDLS measurements as I have tested in DLS measurements and found the same diffusion coefficients with and without adding NaCl. Figure 4.12 shows the DLS measurements of MTAB-GNRs at varying NaCl concentrations. Increasing the salt concentration up to 0.5 mM does not show a change in the diffusion coefficient

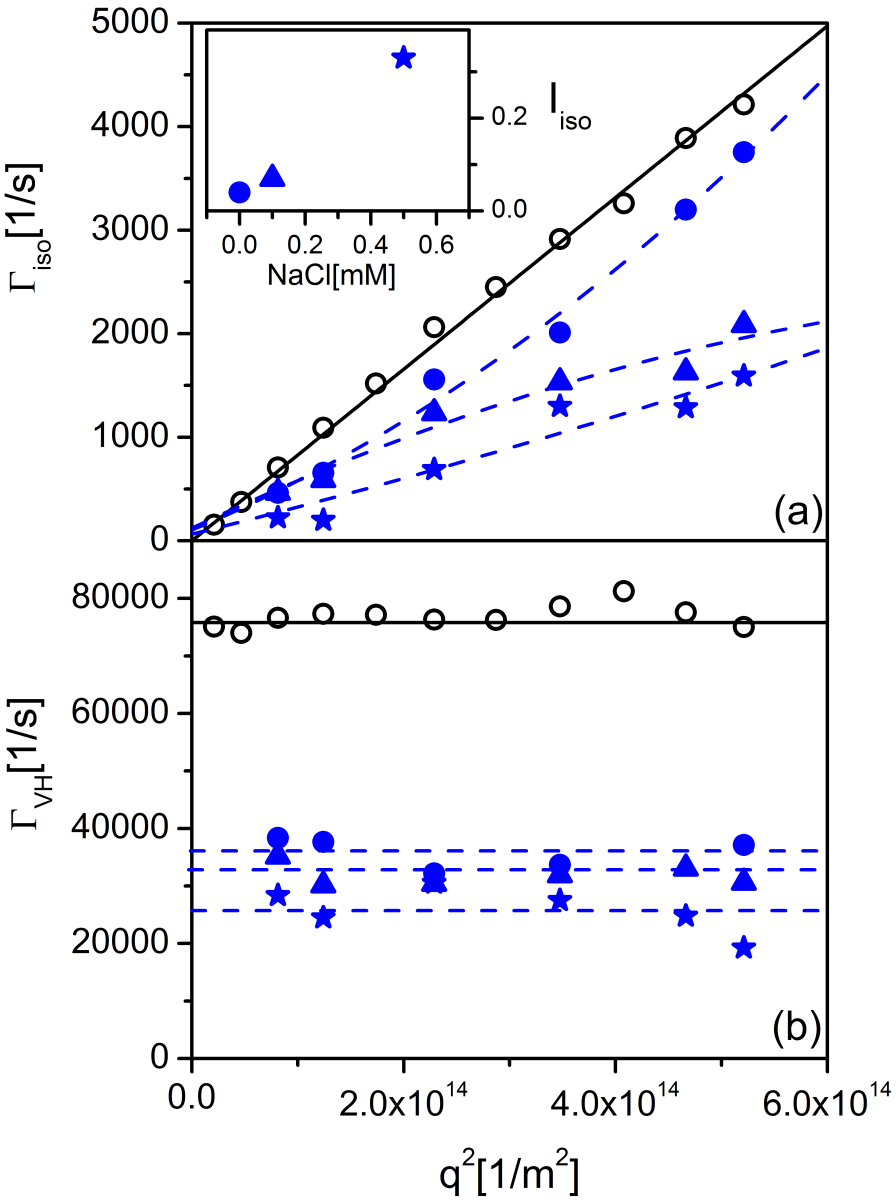

Figure 4.11: Relaxation rates Γ_{xy} as a function of q^2 of MTAB-GNRs in xy=iso (polarized) and xy=VH (depolarized) geometry in bulk measured by DLS (black open circle) and close to a wall measured by REDLS with no salt added (blue full circle) and at varying NaCl concentrations: 0.1 mM (blue full triangle) and 0.5 mM (blue full star). The solid lines denote the fits of eqs. (2.32) and (2.34) to the experimental C_{VH}[q,t] and C_{iso}[q,t], respectively. The dashed lines represent the Brownian motion near a wall (gold interface) as modeled by eq. 4.15 for R_h= 26 nm in (a) and eq. (2.32) in (b). Inset in (a): total intensity I_{iso} in VV geometry by REDLS with different salt concentrations.

within the experimental error (Table 4.4).

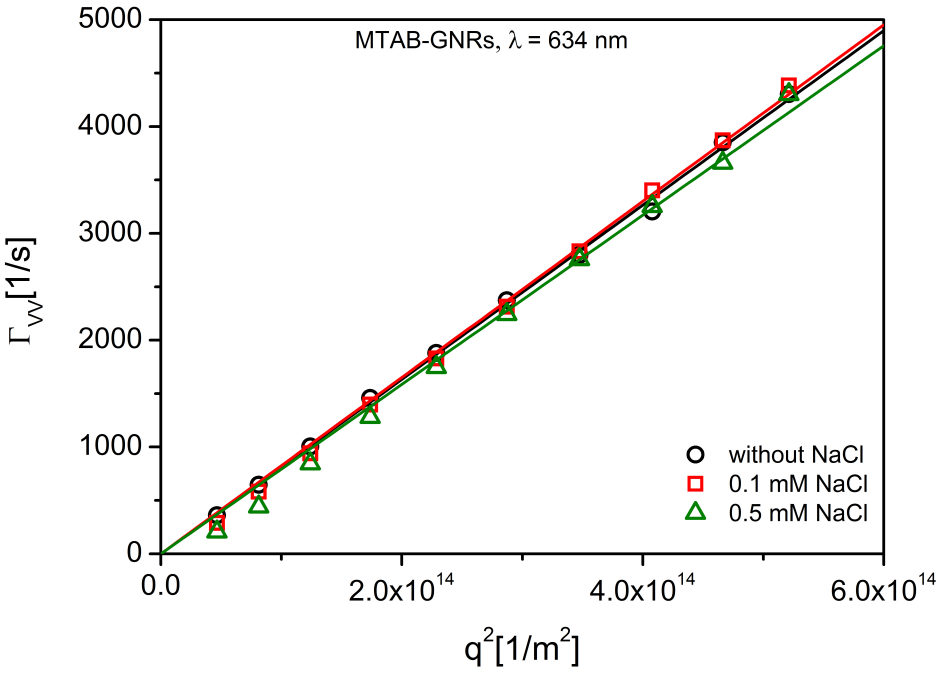

Figure 4.12: Relaxation rates Γ_{VV} as a function of q^2 of MTAB-GNRs at varying NaCl concentrations (without salt (black circles), 0.1 mM (red squares) and 0.5 mM (green triangles)) measured by DLS to check the possible aggregation with adding salt. Increasing the salt concentration up to 0.5 mM does not show a change in the diffusion coefficient. The solid lines represent the linear fit using eq. 2.34.

Compared with no salt, by using 0.1 mM (κ^{-1}= 30 nm) and 0.5 mM (κ^{-1}= 13 nm) NaCl concentrations a decrease in the MTAB-GNRs mobility close to a wall is observed. This decrease in mobility by adding salt cannot be explained by the hydrodynamic model of references [77, 80]. The reason is not an influence of the ionic strength on the mobility, but an increase of particle concentration close to a wall and thus an increase of the slower fraction of the GNRs. For very low NaCl concentrations, i.e. no added salt, most of the MTAB-GNRs are repelled by the surface of approximately the same electric charge. The average diffusion coefficient parallel to the surface is then almost the same as in bulk. By adding salt, average diffusivity parallel to a surface decreases with decrease in the electrostatic potential or in other words, an increase in salt concentration (0.1 mM (blue full triangle) and 0.5 mM (blue full star) in Figure 4.11). The values of the two transport coefficients D_0 and D_R in bulk and the translational anisotropy parallel and

Table 4.4: Anisotropy in diffusion of MTAB-GNRs with an apparent hydrodynamic radius of R_h = 26 nm with varying salt concentration measured in bulk solution with DLS and near a wall with REDLS. The Debye length (κ) for no salt solution cannot be longer than 680 nm [127].

		DLS		REDLS		
NaCl [mM]	κ^{-1} [nm]	$D_0 \times 10^{-12}$ [$m^2 s^{-1}$]	$D_R \times 10^3$ [s^{-1}]	$\langle D_\parallel \rangle / D_0$	$\langle D_\perp \rangle / D_0$	$D_R \times 10^3$ [s^{-1}]
0	680	8.2 ± 0.5	12.6 ± 0.5	0.96	0.52	6.1 ± 0.4
0.1	30	8.3 ± 0.2	12.1 ± 0.4	0.37	0.59	5.4 ± 0.2
0.5	13	8.9 ± 0.3	12.8 ± 0.3	0.35	0.29	5.0 ± 0.3

perpendicular ($\langle D_\parallel \rangle / D_0$ and $\langle D_\perp \rangle / D_0$) to the surface using eq. 4.15 are listed in Table 4.4. The translational anisotropy parallel and perpendicular to the surface decreases with increasing salt concentration within experimental error (Table 4.4).

In the inset of Figure 4.11 (and Table 4.3), total intensities (I_{tot}) of REDLS for different NaCl concentrations are compared. The added salt changes the extent of the inter-particle repulsion as well as the repulsion by the charged surface. Assuming the MTAB-GNRs to be evenly distributed in the scattering volume, about 10 times more particles entered the scattering volume at the highest salt concentration ($I_{tot} \propto N$, N number of scattering particles) compared to the sample without added salt. Due to the reduced repulsion between wall and particle, the number of particles increases linearly with salt concentration.

4.2.2 Proof of the functionalizing of MTAB-GNRs

As mentioned in Section 3.1.2, the CTAB-GNRs (60/25 nm) have been functionalized with MTAB. DLS can be used to check if the MTAB-GNRs have the same relaxation rate and hydrodynamic radius (R_h) as the CTAB-GNR and no aggregation during the process has happened. Figure 4.13 shows the relaxation function in VV (main plot) and VH geometry (inset) for CTAB-GNRs (red circle) and MTAB-GNRs (black circle). Within the experimental error the MTAB- and CTAB-GNRs exhibit the same relaxation rates and hydrodynamic radii (R_h) of 22.56 ± 0.26 nm and 25.28 ± 0.39 nm, respectively. Based on the R_h values, this finding shows the successful exchange of the CTAB bilayer for the MTAB monolayer [89]. The difference of ∼ 2.5 nm between

R_h values refers to one more layer of CTAB on the GNRs which confirms the previous studies of CTAB on the GNRs as a bilayer [128–131].

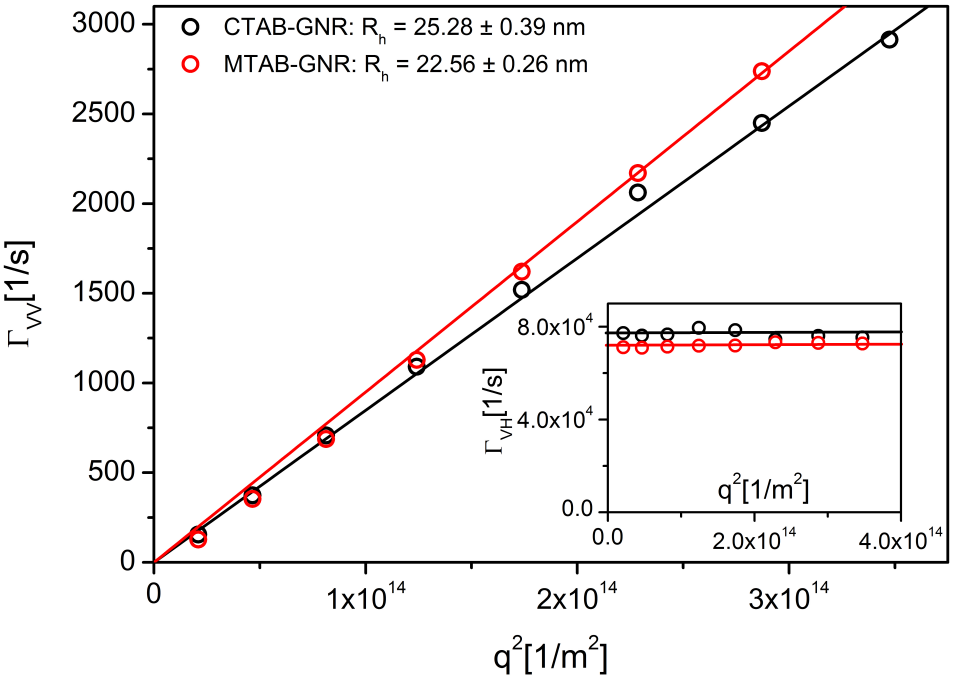

Figure 4.13: Comparison of the relaxation rates Γ_{VV} (main plot) and Γ_{VH} (inset) as a function of q^2 of CTAB- and MTAB-GNRs measured by DLS. The solid lines represent the linear fit using eqs. 2.34 in the main plot and 2.32 in the inset. Within the experimental error the CTAB- and MTAB-GNRs exhibit the same relaxation rates and hydrodynamic radii (R_h). The difference of ~ 2.5 nm between R_h values refers to one more layer of CTAB on the GNRs.

4.3 Dynamics of CTAB stabilized gold nanorods (CTAB-GNRs) near a wall

I studied the influence of the surfactant cetyltrimethylammonium bromide (CTAB) on the diffusion and rotation of gold nanrods (60/25 nm, AR = 2.4) in water close to a solid wall. Two recently introduced evanescent dynamic light scattering techniques, Resonance Enhanced Dynamic Light Scattering (REDLS) and Waveguide Enhanced Dynamic Light Scattering (WEDLS) were used. The GNRs, stabilized by CTAB, are showing a strong slowing down of the translational diffusion coefficient. For rotational

diffusion this slowing down is distinct but less pronounced. The solid walls were prepared to have positive charges (cysteamine-functionalized gold layer) or to be neutral (poly(methyl methacrylate) (PMMA) layer) - the difference had only minor effects on the slowing down. Adsorption of free CTAB at the solid wall was identified as the probable cause for the slowing down.

4.3.1 Effect of the surfactant CTAB on dynamics of CTAB-GNRs

CTAB stabilized GNRs have been analyzed with DLS in bulk and REDLS as well as WEDLS close to a solid wall. The experimental, normalized to one, relaxation functions C[q,t] for REDLS experiment in polarized (index VV: polarization axis of incident and scattered light is vertical with respect to the scattering plane) and depolarized (index VH: polarization of the scattered light is horizontal with respect to the scattering plane) geometry for dilute suspension of GNRs are shown in the inset of Figure 4.14. The polarized (VV) correlation function consists of two relaxations functions which are related to the isotropic and anisotropic scattering, whereas in the depolarized (VH) geometry only anisotropic scattering is detected. Furthermore, the fast process in the VV geometry is related to the anisotropic scattering in the VH geometry (inset in Figure 4.14(a)) [22,75]. To extract the relaxations rates and amplitudes of the correlation functions C[q,t], a stretched exponential fit (Kohlrausch-Williams-Watts function, KWW) in VH geometry was applied [71, 72]. In VV geometry, I have used a sum of KWW functions. In Section 2.4.2, the applied equations 2.31, 2.32, 2.33 and 2.34 for the data analyzing in this chapter can be found.

Looking at the VV characteristic rate Γ in Figure 4.14(a) and Table 4.5, the translational diffusion coefficient (slope of Γ_{VV} vs. q^2) is a factor of 7.7 slower close to the wall compared to bulk. The data in Figure 4.14(b) indicates that the VH decay rate, Γ_{VH}, measured close to the wall exhibits a lower slope of Γ vs. q^2 but this slowing down is less pronounced and amounts to a factor of 1.3. Furthermore, Γ_{VH} does not show a relation of the type $\Gamma_{VH} = 6D_R + D_0q^2$ and instead of that shows a q-independent behavior.

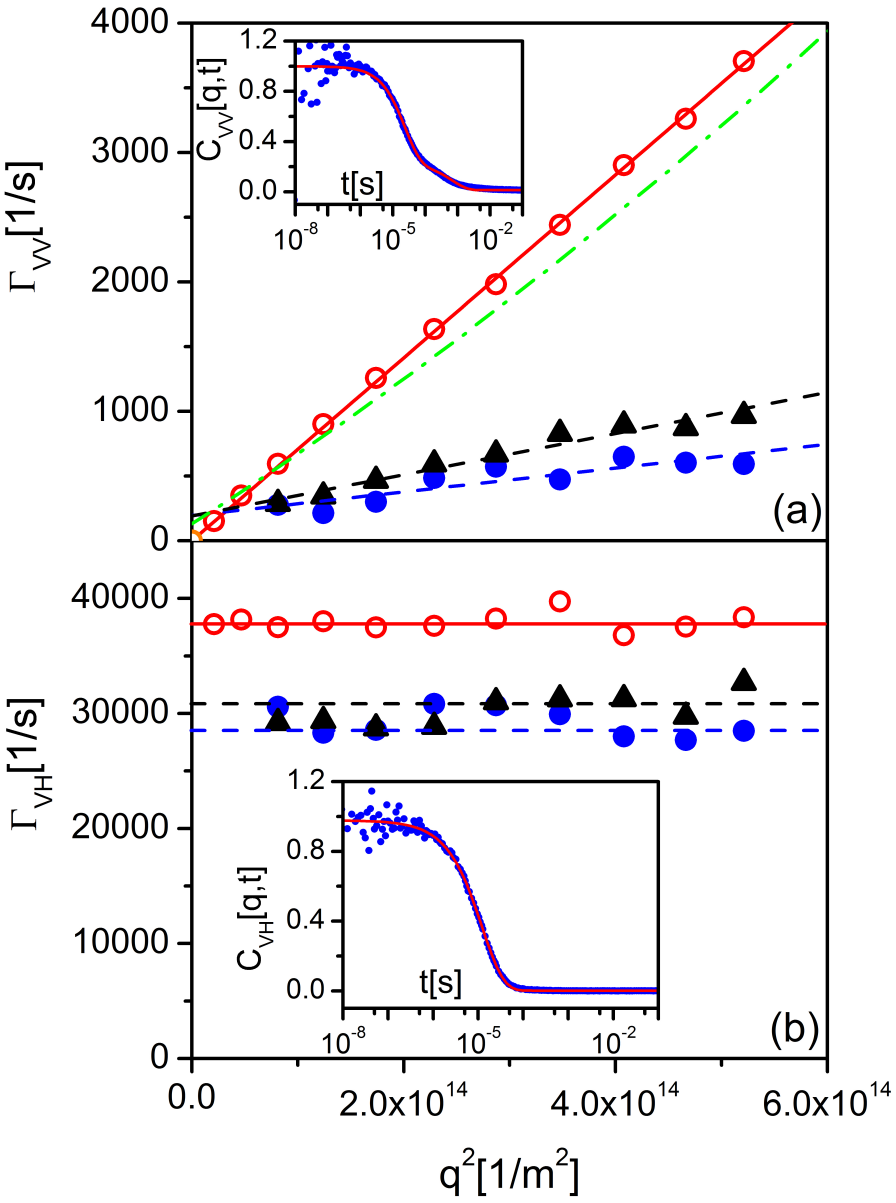

Figure 4.14: Relation rate Γ as a function q^2 of GNRs in polarized (VV) and depolarized (VH) geometry in bulk from DLS (red open circle) and close to the wall using REDLS (blue full circle) and WEDLS (black full triangle) techniques. The solid lines denote the fits of eqs. 2.32 and 2.34 to the experimental, normalized C_{VH}[q,t] and C_{VV}[q,t], respectively. The dashed lines represents the motion near a wall (blue: gold, black: PMMA) fitted by a linear fit. The dash-dotted green line is the expected behavior for hydrodynamic interactions with the wall from eq. 2.49. Inset: polarized and depolarized correlation functions C[q,t] of GNRs measured by REDLS at a scattering angle of 90° (q = 0.019 nm^{-1}). The red solid lines in the inset represent the fits of eqs. 2.33 and 2.31.

For small rods $6D_R >> D_0q^2$, therefore Γ_{VH} becomes virtually q-independent, i.e. a q-dependence cannot be resolved within the experimental error. This behavior is discussed in literature [22, 75] and also in Section 4.1 for the case of predominantly rotational vs. translational diffusion in the depolarized experiment.

Table 4.5: Translational (D_T) and rotational (D_R) diffusion of CTAB stabilized GNRs with aspect ratio 2.4 (60/25 nm) measured by DLS, REDLS and WEDLS

Method	$D_T \times 10^{-12}$ [m^2s^{-1}]	$D_R \times 10^3$ [s^{-1}]
DLS	7.07 ± 0.3	6.30 ± 0.3
REDLS	0.92 ± 0.2	4.71 ± 0.3
WEDLS	1.59 ± 0.2	5.05 ± 0.4

Due to the strong slowing down I cannot use the theoretical prediction of Γ (eq. 2.49) which is only influenced by hydrodynamic interactions with the wall [88]. The theoretical values are plotted as a dash-dotted green line in Figure 4.14(a). Therefore, I have used a linear fit to estimate the diffusion coefficient in bulk and close to a wall. From the data in Table 4.5 the translational diffusion of CTAB stabilized GNRs is the factor of 7.7 and 4.5 slower compared to the bulk for REDLS and WEDLS measurements, respectively.

In the previous section [90], I showed that a surfactant free solution of GNRs (MTAB stabilized GNRs) close to a wall exhibited an expected slowing down within hydrodynamic theory and can be explained by the theoretical calculation reported in literature [88]. In this case a slowing down of the factor of 1.2 and 2 for translational and rotational diffusion close to a wall has been shown, respectively [90].

In the work presented in this section, I observed a stronger slowing down of a non surfactant free solution of the GNRs (CTAB stabilized GNRs) of a factor of 7.7 for the translational diffusion coefficient close to the wall. Two possible explanations came to my attention for this stronger slowing down. First, it is known that CTAB binds better to the cylindrical surface of the GNRs rather than to their end caps [132–134]. Therefore, the end surface of GNRs may not be covered with CTAB completely and can attach for a short time to the wall. Second, GNRs are stabilized with CTAB, which has a hydrocarbon tail and a tetramethylammonium ion headgroup, form bilayers or even

multilayer structures on the GNRs surface. In such structures, it is postulated that the CTAB-GNRs prefer the end-to-end or end-to-side approach over side-to-side [135–137], which make it possible that the GNRs with tetramethylammonium group at the surface are adjacent to GNRs only with hydrocarbon tail. These end-to-end or end-to-side interactions may result in a slowing down of the diffusion of the GNRs.

These two explanations can be ruled out, because the same behavior would also happen in the case of a surfactant free solution for MTAB stabilized GNRs [90], which is not the case. This applies to other surfactant free solutions, where the GNRs are stabilized e.g. with thiols [89,138] or phospholipids [139] to prevent agglomeration.

There is a third possibility. Compared to the MTAB study (Section 4.2) [90], the difference here is the presence of free surfactant CTAB in the GNRs solution. Therefore, the free CTAB could be responsible for this slowing down.

The CTAB on the GNRs is widely accepted to form a bilayer. This has been supported experimentally with IR spectroscopy, thermogravimetric analysis (TGA), zeta potential analysis [128,129] and surface-enhanced raman spectroscopy (SERS) [130,131]. The adsorption of CTAB on different substrates has been investigated by various experimental methods such as quartz crystal microbalance (QCM) [140,141], atomic force microscopy (AFM) [142,143], ellipsometry [144,145] and neutron reflection [146,147] to study the adsorbed amount, layer structure, and adsorbed aggregate thickness. In a neutron reflectivity study, the adsorption onto hydrophilic silica and onto the hydrophilic cellulose surfaces have been shown to be similar, and were in the form of surface aggregates. In contrast, the adsorption onto the hydrophobic cellulose surface was lower and in the form of a monolayer [148].

However, the adsorption of CTAB on positively functionalized gold layer and PMMA layer and its influence on the near wall dynamics of the GNRs is not investigated so far. My results suggest that the large amount of CTAB in the GNRs solution and specially the free bromide (Br^-) ion can adsorb at the positively functionalized gold layer. This screens the positive charges on the gold layer and CTAB can adsorb with the tetramethylammonium ion headgroup to the gold layer. Therefore, the CTAB on the GNRs could interact with the hydrocarbon tail of the adsorbed CTAB on the gold

layer and result in the slowing down of the GNRs diffusion.

A relaxation process with characteristic time that relates to the adsorption-desorption process of the CTAB cannot be observed by REDLS experiments due to the expected very low contrast of the relaxation function.

To check for the adsorption of the CTAB on the gold and PMMA layer, I have used kinetic surface plasmon resonance (SPR) changing from water to a solution of the CTAB slightly below the critical micelle concentration of 1 mM. This is the same concentration of CTAB as in the GNRs solutions used for the REDLS and WEDLS experiments. First, a plasmon resonance curve is scanned to find out the angle for the kinetic SPR measurement and monitor the optical properties before injection of the CTAB solution. The angle used for the kinetic measurement was 65.5° for gold and 67.7° for PMMA layer, which showed an approximately linear region of the plasmon curve (inset Figure 4.15 blue curve). The intensity at this angle is then recorded as a function of time for the kinetic SPR. At a time defined as t= 0, I replaced water in the measurement cell by the CTAB solution. The following increase of the reflectivity can be attributed to the adsorption of CTAB to the gold or PMMA layer (Figure 4.15). To account for the two step adsorption visible in Figure 4.15 a fit of a double Boltzmann Sigmoidal function has been used (a parametrized version of the Logistic function);

$$R = R_0 + A\left(\frac{f}{1+e^{\frac{t-t_1}{k_1}}} + \frac{1-f}{1+e^{\frac{t-t_2}{k_2}}}\right) \tag{4.19}$$

with A the total amplitude of R increase, R_0 the starting value, f the fraction of R, t_1, t_2 the characteristic times marked by the inflection point of the curve and k_1, k_2 the slopes in the vicinity of the inflection point. The use of this function for the slow adsorption process might be physically not justified, but to compare timescales to fit with the same function gives comparable results.

The timescales from this fit for the case CTAB solution over gold was for t_1= 211 s and for t_2= 5090 s, while for the case of CTAB solution over PMMA t_1= 244 s and t_2= 1990 s. The fraction of adsorption (parameter f, 1-f) is 80% for the fast and 20% for the slow adsorption in both cases.

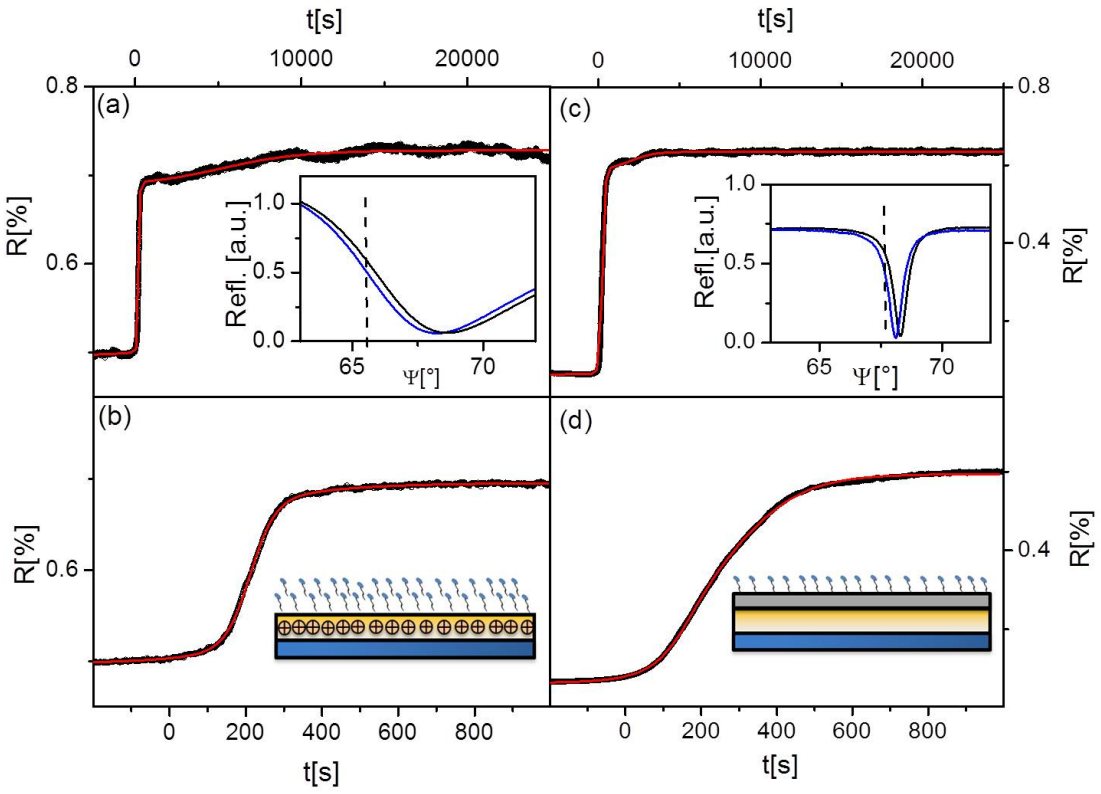

Figure 4.15: Adsorption kinetic measured by SPR on (a,b) gold layer at an angle 65.5° and (c,d) on PMMA layer at an angle 67.7°. The red lines are fits of the adsorption kinetics to a double Boltzmann distribution. Insets: in (a) the plasmon resonance and in (c) waveguide curves of pure water (blue line) and CTAB in water (black line) before and after CTAB adsorption, respectively. Inset in (b) and (d): Cartoons showing the adsorption of CTAB on gold and PMMA layer.

A full SPR curve is scanned (inset Figure 4.15 black curve) after completion of the kinetic SPR. The shift in the surface plasmon curve yields to the film thickness (eq. 3.2) of CTAB of about 4.55 nm and 2.95 nm for gold and PMMA layer, respectively. From the literature a length of 2-3 nm for a fully stretched CTAB molecule is given [149]. Therefore, I deduce a double layer of CTAB on the gold and a single layer on the PMMA. The rotation of the GNRs as being measured in the VH experiment (Figure 4.14(b)) is not as strongly effected by the CTAB layer. A slowing down can be observed but amounts only to about 30% (Table 4.5) and is within experimental error independent of the charge on the wall. Due to the high rotational rate of around 30,000 1/s (Figure 4.14(b)), an interaction of the GNRs with the adsorbed CTAB layer on the wall as well

as coupling to translational dynamics is less probable.

4.3.2 Screening the charge of the CTAB-GNRs using NaCl salt

As described in Section 4.2, the electrostatic interactions between two charged bodies in a medium containing free charges or ions are screened by the free charges. Unfortunately, the CTAB-GNRs are aggregated after adding NaCl salt. Figure 4.16 shows the relaxation function in VV geometry by increasing NaCl salt from 10^{-4} mM to 10^{-1} mM. Even using 10^{-1} mM NaCl leads to the aggregation of the CTAB-GNRs. In Figure 4.17 and Table 4.6 the corresponding translational diffusion coefficient (D_T) and hydrodynamic radius (R_h) as a function of the added salt is shown.

Table 4.6: Translational diffusion coefficient (D_T) and hydrodynamic radius (R_h) of CTAB-GNRs (60/25 nm) at varying salt concentration measured by DLS.

NaCl[mM]	$D_T \times 10^{-12}[\mathrm{m^2 s^{-1}}]$	R_h[nm]
10^{-4}	8.15	26.29
10^{-3}	8.33	25.71
10^{-2}	8.37	25.59
10^{-1}	5.63	38.09

4.4 Depolarized dynamic light scattering of spherical SiO_2@GNRs near a wall

Rotation or reorientation of particles in solution can be tested by dynamic light scattering (DLS) methods. These motions are visible in DLS via the polarizability tensor of the particle describing its electron distribution [73]. In a fixed laboratory frame, if the particle e.g. rotates the polarizability tensor rotates as well. In general, in studies of particles in solution this part of the scattered light is, compared to the signal from translational motion, small and in the analysis of polarized light scattering dismissed since the asperity is small. In order to study the rotational behavior in cases like the hydrodynamic influence of a proximity solid wall, the spherical particles with an asymmetric core were devised.

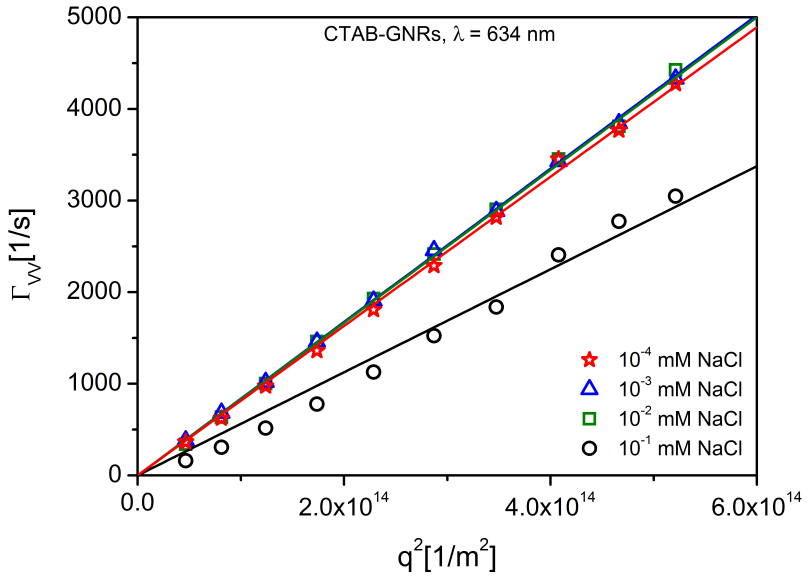

Figure 4.16: Relaxation rates Γ_{VV} as a function of q^2 of CTAB-GNRs at varying NaCl concentrations (10^{-1} mM (black circle), 10^{-2} mM (green square), 10^{-3} mM (blue triangle) and 10^{-4} mM (red star)) measured by DLS to check the possible aggregation with adding salt. Even using 10^{-1} mM NaCl leads to the aggregation of the CTAB-GNRs. The solid lines represent the linear fit using eq. 2.34.

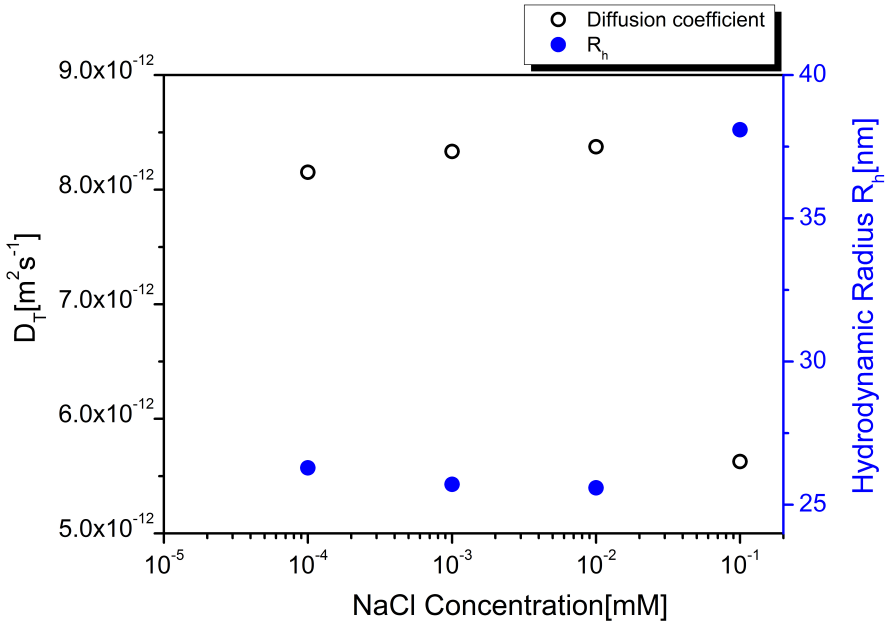

Figure 4.17: Translational diffusion coefficient (D_T) and hydrodynamic radius (R_h) of the CTAB-GNRs as a function of the added salt. By using a salt concentration of 10^{-1} mM the hydrodynamic radius increases to 38.09 nm and D_T decreases to 5.63×10^{-12}[m^{2}s^{-1}].

Little experimental work has been done to probe spatially resolved rotational diffusion of nanoparticles in the vicinity of a wall. I present the experimental study of rotational diffusion of spherical silica coated gold nanorods (SiO_2@GNRs), using resonance enhanced dynamic light scattering (REDLS).

4.4.1 Translational and rotational diffusion of SiO_2@GNRs

Translational and rotational diffusion of GNRs in bulk and close to the surface have been studied intensively in Sections 4.1, 4.2 and 4.3 [75,90]. In this section, I will focus on the translational and rotational diffusion of SiO_2@GNRs and compare the results with GNRs and silica particles of the same size as SiO_2@GNRs. GNRs with aspect ratio (L/d) of 2.4 and silica particles with the size of 177 nm in diameter (concentration: 50 mg/ml, micro particles GmbH, Berlin, Germany) have been used. The functionalizing of the SiO_2@GNRs is described in Section 3.1.3.

Polydispersity of the sample is expected to have a strong effect on the Brownian diffusion and optical properties. This depends on the particle size and shape so that the size variation may strongly affect the DLS results. To proof the polydispersity of the sample I used Cumulant fit [76–78]. The average Polydispersity Index (PDI) for SiO_2@GNRs and silica particles is 0.06 and 0.01, respectively. Therefore, the samples can be considered as monodisperse.

Figure 4.18 shows the relaxation function C[q,t] in VH (main plot) and VV (inset) geometry of GNRs, SiO_2@GNRs and silica particles at $q = 1.71 \times 10^{-2}$ nm^{-1} measured by DLS. In VH geometry one relaxation mode for GNRs and SiO_2@GNRs was observed whereas it was not possible to measure the correlated signal for spherical silica particles. This type of signal in depolarized geometry corresponds to the case of orientational fluctuations and refers to the rotational diffusion of the particles. The data for silica particles before 10^{-5} seconds were removed due to the very noisy signal. In VV geometry (inset in Figure 4.18), GNRs exhibit two relaxation modes corresponding to the translational and rotational diffusion of the GNRs. This phenomenon was discussed in detail in Section 4.1 [75]. After the silica coating of the GNRs, the fast process or the

rotational signal is not visible anymore. SiO_2@GNRs and silica particles show the same translational signal. This is an expected effect due to the same size of the SiO_2@GNRs and silica particles.

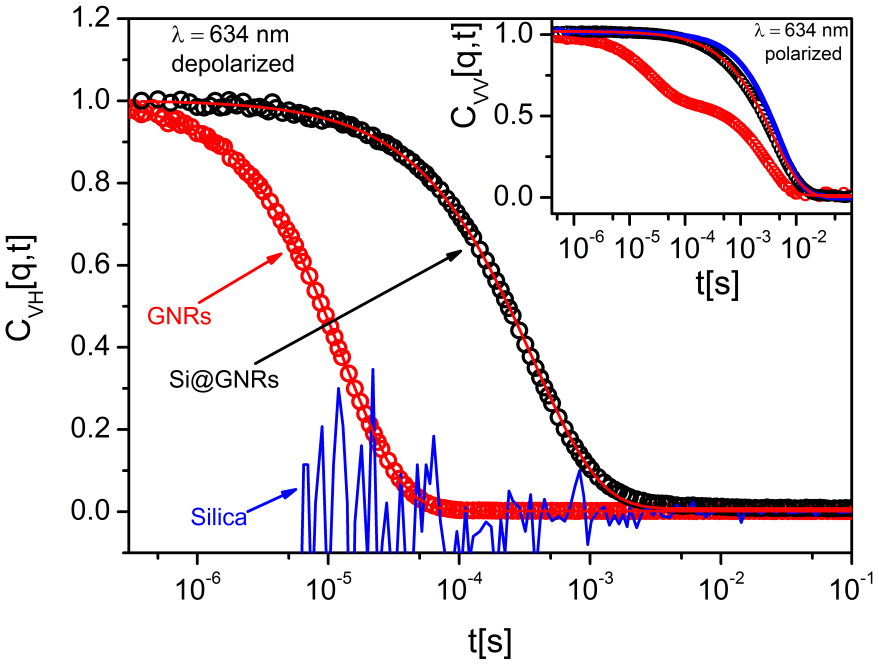

Figure 4.18: DLS in bulk solution: Normalized intensity autocorrelation functions of SiO_2@GNRs (black circles) and GNRs (red circles) at wavelength 634 nm and scattering angle 30° (q= 1.71 × 10^{-2} nm^{-1}) in VH (depolarized) geometry. There is no correlated signal for spherical silica particles in depolarized geometry. The inset is the intensity autocorrelation functions in VV (polarized) geometry. The fast process of GNRs in the VV correlation function is not visible after silica coating. For comparison the VV-correlation function of silica particle with a diameter of 177 nm is plotted as a full line. The full red lines represent the fits of eqs. 2.33 and 2.31 to the experimental functions of C_{VV}[q,t] (inset) and C_{VH}[q,t] (main plot).

Data analyses have been performed using a stretched exponential function for one signal mode relaxation function and a sum of two stretched exponential functions in the case of two relaxation modes (eqs. 2.31 and 2.33). The fast process in the VV geometry (Γ_f) is related to the relaxation rate in the VH geometry (Γ_{VH} (q) = Γ_f, Γ_s= $D_T q^2$). The shape parameter β characterizes the distribution of the relaxation time. In DLS an almost monodisperse behavior was observed with β values close to one ($\beta = 0.95$). The relaxation rate as a function of the square of the scattering wave vector q^2 is shown in Figure 4.19. Γ_s(= Γ_{VV}) was found to be diffusive, that is proportional to q^2. The

slope yielded the translational diffusion coefficient D_T. It enabled the calculation of an effective Stokes-Einstein hydrodynamic radius R_h by $D = k_BT/6\pi\eta R_h$ where k_B is the Boltzmann constant, T denotes the temperature, and η is the viscosity of the solvent. From the numbers in Table 4.7, the hydrodynamic radii of silica particles and SiO_2@GNRs are in the same range.

Table 4.7: Anisotropy in diffusion of GNRs, SiO_2@GNRs and silica particles measured in bulk solution with DLS and near a wall with REDLS

	DLS			REDLS		
Sample	$D_T \times 10^{-12}$ [m^2s^{-1}]	$D_R \times 10^3$ [s^{-1}]	R_h [nm]	$\langle D_\parallel \rangle / D_0$	$\langle D_\perp \rangle / D_0$	$D_R \times 10^3$ [s^{-1}]
GNRs	7.07±0.3	6.30±0.7	30.3±0.1	0.78	0.61	5.30±0.5
SiO_2@GNRs	2.55±0.2	0.18±0.01	84.0±0.7	0.67	0.42	0.13±0.01
Silica	2.40±0.1		89.3±0.3	0.66	0.39	

For measurements close to the interface Resonance Enhanced Dynamic Light Scattering (REDLS) was used to perform DLS measurements in polarized (VV) and depolarized (VH) geometry. It demonstrates the feasibility of such measurements even in depolarized light scattering. Figure 4.19 depicts the relaxation rate Γ of the GNRs, SiO_2@GNRs and silica particles in both VV and VH geometry measured by REDLS (full symbols) compared to the bulk measured by DLS (open symbols). A slow-down of both the translational and rotational diffusion coefficients in REDLS with respect to the bulk data is clearly observed. This slow-down near wall dynamics confirms previous findings in literature and is expected because of the wall-induced retardation [77].

The data in Figure 4.19(a) indicates that Γ_{VH} exhibits a relation of the type $\Gamma_{VH}=6D_R+D_Tq^2$ in the case of SiO_2@GNRs (solid line: DLS, dashed line: REDLS). The nonzero intercept at q = 0 is related to the rotational diffusion coefficient D_R [69, 150]. For GNRs, a q-independent behavior has been observed as discussed in Section 4.1. Whereas for the spherical silica particles no rotational signal was observed, for spherical SiO_2@GNRs it was possible to measure the rotational signal corresponding to the case of orientational fluctuations of symmetric top particles.

The solid lines in Figure 4.19(b) are fits of $\Gamma_{VV} = \Gamma_s = D_Tq^2$ for the measurement in bulk with DLS. The dashed lines in Figure 4.19(b) correspond to the theoretical

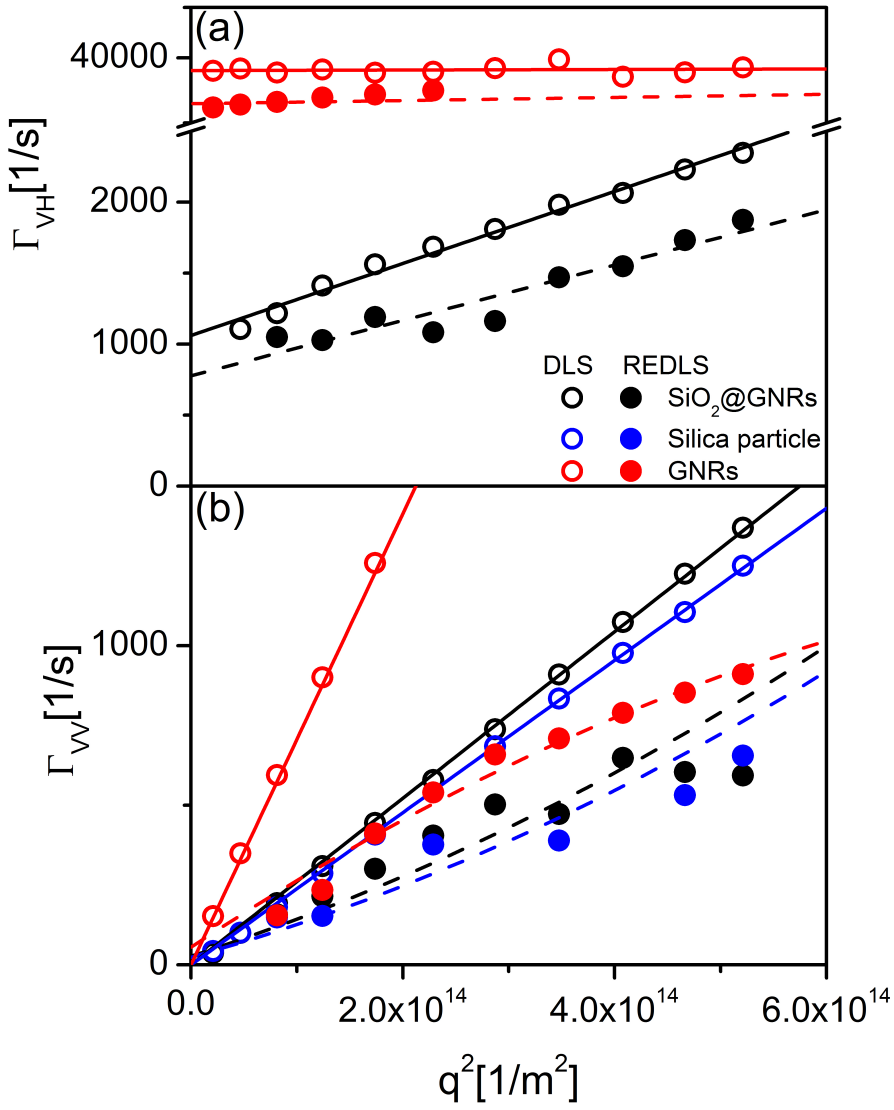

Figure 4.19: Relaxation rate Γ vs. q^2 for GNRs, SiO_2@GNRs and silica particles measured by REDLS (full symbols) and DLS (open symbols) in (a) VH and (b) VV geometry. The solid lines denote the fits of $\Gamma_{VH} = 6D_R + D_T q^2$ in (a) and $\Gamma_{VV} = \Gamma_s = D_T q^2$ in (b) to the experimental $C_{VH}[q,t]$ and $C_{VV}[q,t]$, respectively. The dashed lines represent the Brownian motion near a wall (gold interface) as modeled by $\Gamma_{VH} = 6D_R + D_T q^2$ in (a) and eq. 2.49 for $R_h = 84.04$ nm and $R_h = 89.29$ nm of SiO_2@GNRs and silica particles, respectively.

prediction of Γ influenced by hydrodynamic interaction with the wall in polarized (VV) geometry (eq. 2.49) [88]. As mentioned in Section 4.3, the GNRs stabilized with CTAB (CTAB-GNRs) exhibit a strong slowing down close to the wall, which cannot be explained by the hydrodynamic theory close to the wall. It can be explained by the adsorption of the free CTAB in the GNRs solution on the gold layer. A complete explanation of this slowing down can be found in Section 4.3.

The rotational and translational diffusion of silica particles, SiO_2@GNRs and GNRs are compared in the Table 4.7. Although the rotational diffusion of SiO_2@GNRs is about 40 times smaller compared to the GNRs, it is still possible to measure the rotational signal of spherical SiO_2@GNRs close to the wall due to the strong anisotropic signal produced by GNRs in the silica shell.

Chapter 5

Conclusion and Outlook

5.1 Conclusion

Understanding dynamics of the GNRs in bulk solution and close to a wall plays a key role in a number of important physical phenomena. Therefore, I have achieved several objectives in my thesis regarding the dynamics of the GNRs which are summarized in the following.

I have presented a thorough dynamic light scattering (DLS) study of dilute GNRs solutions for the anisotropic (VH) and polarized (VV) components analyzed in the time domain by DLS. The two scattering contributions are associated with rotational diffusion (D_R, normal to the GNR axis) and the average translation diffusion D_0 (parallel and normal to this axis). Both are surface plasmon resonance (SPR) enhanced. The present work revealed that the enhancement becomes stronger for the VH component when the wavelength of the incident laser light wavelengths falls near the longitudinal surface plasmon resonance (LSPR) mode. The latter as observed in the absorption spectrum depends sensitively on size, shape, composition, orientation and local dielectric environment of the GNRs. The broadening of the plasmonic peaks is much wider than what is expected for a monodisperse sample of metallic particles. In order to account for this effect, the polydispersity has been modeled using lognormal distribution of rod lengths and a large number of spherical particles. However, the discrepancy between

TEM images regarding polydispersity leads to the conclusion that other factors, such as the polarizability of the surfactant layer, are contributing to this effect.

The biased resonance enhancement has several pertinent consequences: (i) it allows to measure the VH contribution in the VV-relaxation function through an additional decay yielding D_R; (ii) this anisotropic contribution is solely recorded in the VH component in the nanomolar concentration range; (iii) it opens the application to probe dynamics in complex environments at tracer concentrations without the necessity of fluorescent labeling; (iv) therefore it might help develop polarized microscopy techniques to sort plasmonic nanoparticles according to their shape.

I also utilized the dependence of SPR on the orientation normal to the long axis to reveal the inherent translational anisotropy of rod-like objects by recording the VV-relaxation function near the LSPR mode. In this case, it is rather $D_{\parallel}$ along the symmetry axis than the average D_0 that is observed. This resolution possibility, along with the independent access to D_R, might help address experimentally challenging questions on the rotation-translational coupling in dense systems. Finally, a quantitative description of all three transport coefficients concurrently using the standard analytical expressions, under stick boundary conditions [151], was not feasible. The length and aspect ratio as obtained from electron transmission images can only semi-quantitatively capture D_0 and D_R. Numerical calculations of the Stokes equations for a cylinder of prescribed shape should help elucidate the origin of the observed disparity.

Furthermore, I have investigated the dynamics of GNRs in a surfactant free solution (MTAB-GNRs) and with presence of the surfactant CTAB (CTAB-GNRs) close to a wall using a recently developed evanescent technique - Resonance Enhanced Dynamic Light Scattering (REDLS) - to study relaxation with incident electromagnetic fields localized in the sub-wavelength range close to a solid wall. Although CTAB can be replaced by thiols [128, 138] or phospholipids [89], it is still the most widely used surfactant in producing and handling GNRs. In most preparation methods of the GNRs reported so far, CTAB has been essential for the generation of GNRs. Thus, GNRs are covered with a physisorbed double layer of CTAB molecules. There has to be a large amount of CTAB in the GNR solution to stabilize the GNRs against aggregation.

For MTAB-GNRs, the influence of a solid wall on the diffusion of MTAB-GNRs with apparent hydrodynamic radius of R_h= 26 nm (60/25 nm, AR=2.4) in aqueous dispersions of varying salt concentrations has been shown for a penetration depth of 200 nm. I screened the electrostatic interactions using NaCl to change the repulsion between the positively charged gold wall and the GNR. I was able to measure the translational and rotational coefficients of dilute GNRs close to a solid wall with enhanced sensitivity and signal-to-noise ratio. In addition, I compared the q-dependence of the relaxation rate with hydrodynamic theory under evanescent wave illumination at different salt concentrations. The result revealed that in the case of no added salt, the GNRs are effectively repelled by the wall. In this case, it was possible to describe the data by hydrodynamic theory [77, 88]. By adding salt, more particles enter the scattering volume defined by the evanescent field and the footprint of the laser. I have observed an apparent decrease of the diffusion coefficient of the GNRs close to a wall. This can be attributed to the increased number of particles in the scattering volume. While in the case of no added salt, the repulsion of the particles by the charged wall leaves only a small number in its vicinity, adding salt leads to a more uniform distribution, and thus leads to more particles in the evanescent field which is the scattering volume. The general trend of adding salt is a slowing down of both the parallel and the perpendicular component of the translational diffusion. Only the solution without added salt can be described by the hydrodynamic model of references [77] and [88]. This suggests the need of a modified electro-hydrodynamic theory to explain the diffusion of colloidal particles near a wall.

For CTAB-GNRs, the present study was designed to determine the influence of CTAB surfactant on the translational and rotational diffusion of GNRs with the aspect ratio 2.4 (60/25 nm) in aqueous dispersions. The surface charge of the solid wall was varied. The experiments close to the interface were performed by using REDLS and Waveguide Enhanced Dynamic Light Scattering (WEDLS). The results showed that with the presence of the surfactant CTAB in the GNR solution, a strong slowing down of the translational diffusion can be observed. This slowing down close to the wall cannot be explained by the hydrodynamic theory. My result suggests that the free CTAB in the GNRs solution adsorb on the wall and interact via the hydrocarbon tail with the CTAB

on the GNRs approaching the wall. The adsorption phenomena can be monitored with kinetic surface plasmon resonance and enable to calculate the thickness of the adsorbed CTAB interphase.

Finally, I have measured translational and rotational diffusion of the spherical silica coated GNRs (SiO_2@GNRs) in bulk and close to a wall. Coating silica on GNRs is advantageous for robust bioapplications because it reduces toxicity, improves stability, has good biocompatibility and offers the convenience of surface functionalization [152]. Rotational diffusion is an important feature in the study of many physical, chemical and biological topics and it is experimentally difficult to find a convenient technique to probe spatially resolved rotational diffusion of nanoparticles in the vicinity of a wall. Therefore, REDLS and spherical SiO_2@GNRs are appropriate candidates for investigating rotational diffusion close to a wall.

5.2 Outlook

From all the above results, we now have a better understanding of the dynamics of the GNRs in bulk solution and close to a wall. Since the GNRs have been investigated with different aspect ratios in bulk, the next step would be to examine the dynamics of different aspect ratio of GNRs close to a wall as well. One can also focus on interfacial phenomena to investigate the particle-surface interactions depending on surface chemistry and their effects on diffusivity. It would also be helpful to use other type of neutral surfaces which does not work as waveguide. In this case, the effects of two types of wall could be measured with the same technique, rather than using different techniques for each type of wall. The challenge here would be the preparation of e.g. a stable layer of ~ 5 nm on the gold layer to exclude the effect of the charged gold layer on diffusivity. One can go one step further, demonstrating the transport process inside membranes to understand e.g. how the GNRs diffuse through membranes. Because of the rapidly growing field of nanoparticles in therapeutic applications, understanding and controlling the interaction between nanoparticles and membranes is of great importance. Specially, GNRs have great potential for widespread applications in biomedical and photothermal

therapy due to unique surface plasmon resonance (SPR) ranging from visible to near infrared (NIR) region.

Finally, using REDLS to measure the diffusivity of GNRs close to a metal layer, one is limited to a fixed penetration depth of 200 nm. In order to measure the dynamics of GNRs at different penetration depths with REDLS, one has three possibilities. First, by using different laser wavelength to excite the surface plasmons (560 nm $<\lambda<$ 1000 nm), one can vary in-situ the penetration depth between 100 nm and 600 nm [96]. Second, one can increase the penetration depth using long-range surface plasmons (LRSPs) configuration. LRSPs are electromagnetic modes formed by the coupling of the surface plasmons propagating along opposite interfaces of thin metal layers sandwich between two dielectrics with similar refractive indices (e.g. cytop and water with the refractive indices of ~ 1.33). This enables measurements of the diffusivity with a penetration depth of 600 nm [96,153,154]. Third, in order to change the penetration depth of the evanescent waves in-situ and arrange the measurement with the same wavelength, coupled long-range surface plasmons can be used. This allows the excitation of the evanescent fields with a penetration depth of 360 nm and 950 nm by the same wavelength of 632.8 nm [155].

List of symbols and abbreviations

SPP	Surface Plasmon Polariton
SPR	Surface Plasmon Spectroscopy
LSPR	Longitudinal Surface Plasmon Resonance
TIR	Total Internal Reflection
DLS	Dynamic Light Scattering
REDLS	Resonance Enhanced Dynamic Light Scattering
WEDLS	Waveguide Enhanced Dynamic Light Scattering
EWDLS	Evanescent Wave Dynamic Light Scattering
SERS	Surface Enhanced Raman Spectroscopy
MeNP	Metal Nanoparticle
GNR	Gold Nanorod
SiO_2@GNRs	Silica Coated Gold Nanorods
MTAB	16-Mercaptohexadecyl Trimethylammonium Bromide
CTAB	Cetyltrimethylammonium Bromide
AR	Aspect Ratio
TEM	Transmission Electron Microscopy
PMMA	Poly(methyl methacrylate)
UV-Vis	UV-Visible
T-matrix	Transition Matrix
KWW	Kohlrausch-Williams-Watts
q	Experimental Wave vector $(k_s - k_i)$
k	Wave vector

λ	Wavelength
ξ	Penetration Depth
D_T	Translational Diffusion Coefficient
D_R	Rotational Diffusion Coefficient
R_h	Hydrodynamic Radius
τ	Relaxation Time
Γ	Relaxation Rate
ρ	Depolarization Ratio
ε	Dielectric Constant
ω	Angular Frequency
n	Refractive Index
T_g	Glass Transition Temperature

List of Figures

List of Tables

Bibliography

[1] K.A. Willets; R.P. Van Duyne. Localized surface plasmon resonance spectroscopy and sensing. *Annu. Rev. Phys. Chem.*, 58:267–297, 2007.

[2] P.K. Jain; X. Huang; I.H. El-Sayed; M.A. El-Sayed. Review of some interesting surface plasmon resonance-enhanced properties of noble metal nanoparticles and their applications to biosystems. *Plasmonics*, 2(3):107–118, 2007.

[3] V. Sharma; K. Park; M. Srinivasarao. Colloidal dispersion of gold nanorods: Historical background, optical properties, seed-mediated synthesis, shape separation and self-assembly. *Mater. Sci. Eng. Reports*, 65(1-3):1–38, 2009. Times Cited: 47.

[4] J.N. Anker; W.P. Hall; O. Lyandres; N.C. Shah; J. Zhao; R.P. Van Duyne. Biosensing with plasmonic nanosensors. *Nat. Mater.*, 7:442–453, 2008.

[5] C. Saennichsen; A.P. Alivisatos. Gold nanorods as novel nonbleaching plasmon-based orientation sensors for polarized single-particle microscopy. *Nano Lett.*, 5(2):301–304, 2005.

[6] M. Hu; C. Novo; A. Funston; H. Wang; H. Staleva; S. Zou; P. Mulvaney; Y. Xia; G.V. Hartland. Dark-field microscopy studies of single metal nanoparticles: Understanding the factors that influence the linewidth of the localized surface plasmon resonance. *J. Mater. Chem.*, 18:1949–1960, 2008.

[7] R. Elghanian; J.J. Storhoff; R.C. Mucic; R.L. Letsinger; C.A. Mirkin. Selective colorimetric detection of polynucleotides based on the distance-dependent optical properties of gold nanoparticles. *Science*, 277:1078–1081, 1997.

[8] G. Von Maltzahn; J.H. Park; K.Y. Lin; N. Singh; C. Schwoeppe; R. Mesters; W.E. Berdel; E. Ruoslahti; M.J. Sailor; S.N. Bhatia. Nanoparticles that communicate in vivo to amplify tumour targeting. *Nat. Mater.*, 10(7):545–552, 2011.

[9] P. Zijlstra; P.M.R. Paulo; M. Orrit. Optical detection of single non-absorbing molecules using the surface plasmon resonance of a gold nanorod. *Nat. Nanotechnol.*, 7:379–382, 2012.

[10] M. Pelton; M. Liu; H.Y. Kim; G. Smith; P. Guyot-Sionnest; N.F. Scherer. Optical trapping and alignment of single gold nanorods by using plasmon resonances. *Opt. Lett.*, 31:2075–2077, 2006.

[11] J.A. Schuller; E.S. Barnard; W. Cai; Y.C. Jun; J.S. White; M.L. Brongersma. Plasmonics for extreme light concentration and manipulation. *Nat. Mater.*, 9:193–204, 2010.

[12] F. Schwaiger; W. Zimmermann; W. Koehler. Transient cage formation around hot gold colloids dispersed in polymer solutions. *J. Chem. Phys.*, 135(22):224905–224909, 2011. Times Cited: 1.

[13] R.A. Nome; M.J. Guffey; N.F. Scherer; S.K. Gray. Plasmonic interactions and optical forces between au bipyramidal nanoparticle dimers. *J. Phys. Chem. A*, 113:4408–4415, 2009.

[14] B. Luk'yanchuk; N.I. Zheludev; S.A. Maier; N.J. Halas; P. Nordlander; H. Giessen; C.T. Chong. The fano resonance in plasmonic nanostructures and metamaterials. *Nat. Mater.*, 9:707–715, 2010.

[15] N. Liu; M. Hentschel; T. Weiss; A.P. Alivisatos; H. Giessen. Three dimensional plasmon rulers. *Science*, 332:1407–1410, 2011.

[16] M.S. Hu; H.L. Chen; C.H. Shen; L.S. Hong; B.R. Huang; K.H. Chen; L.C. Chen. Photosensitive gold-nanoparticle-embedded dielectric nanowires. *Nat. Mater.*, 5:102–106, 2006.

[17] Q. Liu; Y. Cui; D. Gardner; X. Li; S. He; I.I. Smalyukh. Self-alignment of plasmonic gold nanorods in reconfigurable anisotropic fluids for tunable bulk metamaterial applications. *Nano Lett.*, 10:1347–1353, 2010.

[18] J.A. Fan; C. Wu; K. Bao; J. Bao; R. Bardhan; N.J. Halas; V.N. Manoharan; P. Nordlander; G. Shvets; F. Capasso. Self-assembled plasmonic nanoparticle clusters. *Science*, 328:1135–1138, 2010.

[19] N.G. Khlebtsov; A.G. Melnikov; V.A. Bogatyrev; L.A. Dykman; A.V. Alekseeva; L.A. Trachuk; B.N. Khlebtsov. Can the light scattering depolarization ratio of small particles be greater than 1/3? *J. Phys. Chem. B*, 109:13578–13584, 2005.

[20] N. Calander; I. Gryczynski; Z. Gryczynski. Interference of surface plasmon resonances causes enhanced depolarized light scattering from metal nanoparticles. *Chem. Phys. Lett.*, 434:326–330, 2007.

[21] B.N. Khlebtsov; V.A. Khanadeev; N.G. Khlebtsov. Observation of extra-high depolarized light scattering spectra from gold nanorods. *J. Phys. Chem. C*, 112:12760–12768, 2008.

[22] J. Rodríguez-Fernández; J. Pérez-Juste; L.M. Liz-Marzán; P.R. Lang. Dynamic light scattering of short Au rods with low aspect ratios. *J. Phys. Chem. C*, 111(13):5020–5025, 2007.

[23] E. Antoniou; P. Voudouris; A. Larsen; B. Loppinet; D. Vlassopoulos; I. Pastoriza-Santos; L.M. Liz-Marzán. Static and dynamic plasmon-enhanced light scattering from dispersions of polymer-grafted silver nanoprisms in the bulk and near solid surfaces. *J. Phys. Chem. C*, 116:3888, 2012.

[24] R. Sigel. Light scattering near and from interfaces using evanescent wave and ellipsometric light scattering. *Curr. Opin. Colloid Interface Sci.*, 14:426–437, 2009.

[25] K. Lan; N. Ostrowsky; D. Sornette. Brownian dynamics close to a wall studied by photon correlation spectroscopy from an evanescent wave. *Phys. Rev. Lett.*, 57:17–20, 1986.

[26] P. Holmqvist; D. Kleshchanok; P.R. Lang. Unexpected slow near wall dynamics of spherical colloids in a suspension of rods. *Langmuir*, 23:12010–12015, 2007.

[27] S. A. Rogers; M. Lisicki; B. Cichocki; J.K.G. Dhont; P.R. Lang. Rotational diffusion of spherical colloids close to a wall. *Phys. Rev. Lett.*, 109:098305, 2012.

[28] M.A. Plum; W. Steffen; G. Fytas; W. Knoll; B. Menges. Probing dynamics at interfaces: Resonance enhanced dynamic light scattering. *Opt. Express*, 17:10364–10371, 2009.

[29] M.A. Plum; B. Menges; G. Fytas; H.J. Butt; W. Steffen. Resonance enhanced dynamic light scattering. *Rev. Sci. Instrum.*, 82(1):015102–015102–11, 2011.

[30] J. Zenneck. Über die Fortpflanzung ebener elektromagnetischer Wellen längs einer ebenen Leiterfläche und ihre Beziehung zur drahtlosen Telegraphie. *Ann. Phys.*, 328:846–866, 1970.

[31] A. Sommerfeld. Über die Ausbreitung der Wellen in der drahtlosen Telegraphie. *Ann*, 333:665–736, 1909.

[32] D. Pines; D. Bohm. A collective description of electron interactions: Collective vs individual particle aspects of the interactions. *Phys. Rev.*, 85:338–353, 1952.

[33] R. H. Ritchie. Plasma losses by fast electrons in thin films. *Phys. Rev.*, 106:874–881, 1957.

[34] L. Novotny; B. Hecht. *Principles of Nano-Optics*. Cambridge University Press, 2012.

[35] W.L. Barnes; A. Dereux; T.W. Ebbesen. Surface plasmon subwavelength optics. *Nature*, 424:824–830, 2003.

[36] S. Zeng; X. Yu; W.-C. Law; Y. Zhang; R. Hu; X.-Q. Dinh; H.-P. Ho; K.-T. Yong. Size dependence of au np-enhanced surface plasmon resonance based on differential phase measurement. *Sensors and Actuators B: Chemical*, 176:1128–1133, 2013.

[37] E. Kretschmann. *Untersuchungen zur Anregung und Streuung von Oberflächenplasmaschwingungen an Silberschichten*. PhD thesis, Hamburg, 1972.

[38] A. Otto. Excitation of nonradiative surface plasma waves in silver by the method of frustrated total reflection. *Zeitschrift für Physik*, 216:398–410, 1968.

[39] S. Underwood; P. Mulvaney. Effect of the solution refractive index on the color of gold colloids. *Langmuir*, 10:3427–3430, 1994.

[40] P. Mulvaney. Surface plasmon spectroscopy of nanosized metal particles. *Langmuir*, 12:788–800, 1996.

[41] G. Raschke. *Molekulare Erkennung mit einzelnen Gold-Nanopartikeln*. PhD thesis, Ludwig-Maximilians-Universität, München, 2005.

[42] M. Moskovits. Surface-enhanced spectroscopy. *Rev. Mod. Phys.*, 57:783–826, 1985.

[43] X. Huang; I.H. El-Sayed; W. Qian; M.A. El-Sayed. Cancer cell imaging and photothermal therapy in the near-infrared region by using gold nanorods. *J. Am. Chem. Soc.*, 128:2115–2120, 2006.

[44] M.L. Brongersma; J.W. Hartman; H. A. Atwater. Electromagnetic energy transfer and switching in nanoparticle chain arrays below the diffraction limit. *Phys. Rev. B*, 62:R16356–R16359, 2000.

[45] D. Ricard; P. Roussignol; C. Flytzanis. Surface-mediated enhancement of optical phase conjugation in metal colloids. *Opt. Lett.*, 10:511–513, 1985.

[46] L. Novotny; R. X. Bian; X.S. Xie. Theory of nanometric optical tweezers. *Phys. Rev. Lett.*, 79:645–648, 1997.

[47] J. Aizpurua; P. Hanarp; D.S. Sutherland; M. Käll; G.W. Bryant; F. J. García de Abajo. Optical properties of gold nanorings. *Phys. Rev. Lett.*, 90:057401, 2003.

[48] P.W. Barber; S.C. Hill. *Light scattering by particles: computational methods.* World Scientific, Singapore, 1990.

[49] M.I. Mishchenko; L.D. Travis. Capabilities and limitations of a current fortran implementation of the t-matrix method for randomly oriented, rotationally symmetric scatterers. *Journal of Quantitative Spectroscopy and Radiative Transfer*, 60:309–324, 1998.

[50] P.C. Waterman. New formulation of acoustic scattering. *J. Acoust. Soc. Am.*, 45:1417–1429, 1969.

[51] P.C. Waterman. Symmetry, unitarity and geometry in electromagnetic scattering. *Phys. Rev. D*, 3:825–839, 1971.

[52] P.C. Waterman . Matrix formulation of electromagnetic scattering. *Proc. IEEE*, 53:805–812, 1965.

[53] Stratton JA. *Electromagnetic theory.* New York: McGraw-Hill, 1991.

[54] K.F. Riley; M.P. Hobson; S.J. Bence. *Mathematical methods for physics and engineering.* Cambridge University Press, ch. 19, 2002.

[55] E.A.S. Bahaa; M. Carl Teich. *Fundamentals of Photonics. ISBN 0-471-83965-5. Chapter 3, "Beam Optics", pp. 80–107.* New York: John Wiley & Sons, 1991.

[56] F. Bowman. *Introduction to Bessel Functions.* Dover: New York, 1958.

[57] G. Arfken. *"Hankel Functions". §11.4 in Mathematical Methods for Physicists.* Academic Press, 1985.

[58] A. Quirantes. A t-matrix method and computer code for randomly oriented, axially symmetric coated scatterers. *Journal of Quantitative Spectroscopy & Radiative Transfer*, 92:373–381, 2005.

[59] L.T. Tsang; J.A. Kong; R.T. Shin;. Radiative transfer theory for active remote sensing of a layer of nonspherical particles. *Radio Sci.*, 19:629, 1984.

[60] M.I. Mishchenko; L.D. Travis; A.A. Lacis. *Scattering, Absorption, and Emission of Light by Small Particles.* Cambridge University Press, 2002.

[61] S. Ström B. Peterson. T-matrix formulation of electromagnetic scattering from multilayered scatterers. *Phys. Rev. D.*, 10:2670–2684, 1974.

[62] P. Johnson; R. Christy. Optical constants of the noble metals. *Phys. Rev. B.*, 6:4370, 1972.

[63] C. Bohren; D. Huffman. *Light Scattering and Absorption by Small Particles.* Wiley-VCH, New York, 1983.

[64] D. Sarid; W. Challener. *Modern Introduction to Surface Plasmons: Theory, Mathematica Modeling, and Applications.* Cambridge University Press, 2010.

[65] C. Sönnichsen. *Plasmons in metal nanostructures.* PhD thesis, Ludwig-Maximilians-Universität München, 2001.

[66] W. Karthe. *Integrierte Optik.* Akadem. Verlagsges. Geest & Portik, 1991.

[67] T. Fließbach. *Elektrodynamik.* Spektrum Akademischer Verlag, 2005.

[68] M. Hosoda; K. Sakai; K. Takagi. Measurement of anisotropic brownian motion near an interface by evanescent light-scattering spectroscopy. *Phys. Rev. E*, 58:6275–6280, 1998.

[69] B.J. Berne; R. Pecora. *Dynamic Light Scattering: With Applications to Chemistry, Biology, and Physics.* Dover Publications, New York, 2000.

[70] W. Schärtl. *Light Scattering from Polymer Solutions and Nanoparticle Dispersions.* Springer-Verlag, Berlin, 2007.

[71] C.P. Lindsey; G.D. Patterson. Detailed comparison of the williams-watts and cole-davidson functions. *J. Chem. Phys.*, 73:3348–3357, 1980.

[72] G. Williams; D.C. Watts. Non-symmetrical dielectric relaxation behaviour arising from a simple empirical decay function. *Trans. Faraday Soc.*, 66(0):80–85, 1970.

[73] A. Patkowski; W. Steffen; H. Nilgens; E.W. Fischer; R. Pecora. Depolarized dynamic light scattering from three low molecular weight glass forming liquids: A test of the scattering mechanism. *J. Chem. Phys.*, 106:8401–8408, 1997.

[74] M. Glidden; M. Muschol. Characterizing gold nanorods in solution using depolarized dynamic light scattering. *J. Phys. Chem. C*, 116(14):8128–8137, 2012.

[75] M. Haghighi; M.A. Plum; G. Gantzounis; H.J. Butt; W. Steffen; G. Fytas. Plasmon-enhanced dynamic depolarized light scattering. *J. Phys. Chem. C*, 117(16):8411–8419, 2013.

[76] D.E. Koppel. Analysis of macromolecular polydispersity in intensity correlation spectroscopy: The method of cumulants. *J. Chem. Phys.*, 57:4814–4820, 1972.

[77] P. Holmqvist; J.K.G. Dhont; P.R. Lang. Colloidal dynamics near a wall studied by evanescent wave light scattering: experimental and theoretical improvements and methodological limitations. *J. Chem. Phys.*, 126:44707–1–10, 2007.

[78] M. Lisicki; B. Cichocki; J.K.G. Dhont; P.R. Lang. One-particle correlation function in evanescent wave dynamic light scattering. *J. Chem. Phys.*, 136:204704, 2012.

[79] B. Cichocki; E. Wajnryb; J. Blawzdziewicz; J.K.G. Dhont; P.R. Lang. The intensity correlation function in evanescent wave scattering. *J. Chem. Phys.*, 132:074704, 2010.

[80] J. Happel; H. Brenner; R. Moreau. *Low Reynolds number hydrodynamics: with special applications to particulate media (mechanics of fluids and transport processes)*. Kluwer, Boston, 1983.

[81] S.W. Provencher. Contin: a general purpose constrained regularization program for inverting noisy linear algebraic and integral equations. *Comput. Phys. Commun.*, 27(3):229–242, 2006.

[82] S.W. Provencher. A constrained regularization method for inverting data represented by linear algebraic or integral equations. *Comput. Phys. Commun.*, 27(3):213–227, 2006.

[83] B. Wyn. *Dynamic light scattering: The method and some applications*. Clarendon Press Oxford, 1993.

[84] R.F. Roskamp; H.J. Butt; B. Menges; W. Steffen M.A. Plum; S.D.B. Vianna; A. Unger. Probing dynamics near surfaces: waveguide enhanced dynamic light scattering. *Soft Matter*, 7(4):1501–1505, 2011.

[85] H.J. Butt; M. Kappl. *Surface and Interfacial Forces*. Wiley, 2010.

[86] A.J. Goldman; R.G. Cox; H. Brenner. Slow viscous motion of a sphere parallel to a plane wall-i motion through a quiescent fluid. *Chemical Engineering Science*, 22:637–651, 1967.

[87] M.A. Plum; J Ricka; H.J. Butt; W. Steffen. Anisotropic hindered motion close to an interface studied by resonance-enhanced dynamic light scattering. *New J. Phys.*, 12:103022, 2010.

[88] P. Holmqvist; J.K.G. Dhont; P.R. Lang. Anisotropy of brownian motion caused only by hydrodynamic interaction with a wall. *Phys. Rev. E.*, 74:021402–5, 2006.

[89] L. Vigderman; P. Manna; E.R. Zubarev. Quantitative replacement of cetyl trimethylammonium bromide by cationic thiol ligands on the surface of gold nanorods and their extremely large uptake by cancer cells. *Angew. Chem. Int. Ed.*, 124(3):660–665, 2012.

[90] M. Haghighi; M.N. Tahir; W. Tremel; H.J. Butt; W. Steffen. Translational and rotational diffusion of gold nanorods near a wall. *J. Chem. Phys.*, 139(6):064710–7, 2013.

[91] Y.S. Chen; W. Frey; S. Kim; K. Homan; P. Kruizinga; K. Sokolov; S. Emelianov. Enhanced thermal stability of silica-coated gold nanorods for photoacoustic imaging and image-guided therapy. *Opt. Express*, 18:8867–8877, 2010.

[92] Y.S. Chen; P. Kruizinga; P.P. Joshi; S. Kim; K. Homan; K. Sokolov; W. Frey; S. Emelianov. On stability of molecular therapeutic agents for noninvasive photoacoustic and ultrasound image-guided photothermal therapy. *Proc. SPIE*, pages 7564–7561, 2010.

[93] C. Extrand. Spin-coating of very thin polymer films. *Polymer Engineering & Science*, 34:390–394, 1994.

[94] I. Anac; A. Aulasevich; M. J. N. Junk; P. Jakubowicz; R. F. Roskamp; B. Menges; U. Jonas; W. Knoll. Optical characterization of co-nonsolvency effects in thin responsive pnipaam-based gel layers exposed to ethanol/water mixtures. *Macromolecular Chemistry and Physics*, 211:1018–1025, 2010.

[95] W. Knoll. Interfaces and thin films as seen by bound electromagnetic waves. *Annu. Rev. Phys. Chem.*, 49:569–638, 1998.

[96] J. Homola; J. Dostalek; S. Jian; J. Ladd; S. Löfas. *Surface Plasmon Resonance Based Sensors.* Springer: Berlin, 2006, Vol.4.

[97] E. Kretschmann. Determination of optical constants of metals by excitation of surface plasmons. *Zeitschrift für Physik*, 241:313–324, 1971.

[98] R.B.M. Schasfoort; A.J. Tudos. *Handbook of Surface Plasmon Resonance.* The Royal Society of Chemistry, 2008.

[99] P. Horowitz; W. Hill. *The Art of Electronics.* Cambridge University Press, 1989.

[100] J.F. Tassin; R.L. Siemens; W.T. Tang; G. Hadziioannou; J.D. Swalen; B.A. Smith. Kinetics of adsorption of block copolymers revealed by surface plasmons. *J. Phys. Chem.*, 93:2106–2111, 1989.

[101] I. Pockrand. Surface plasma oscillations at silver surfaces with thin transparent and absorbing coatings. *Surf. science*, 72(3):577–588, 1978.

[102] R.G.W. Brown. Dynamic light scattering using monomode optical fibers. *Applied Optics*, 26:4846–4851, 1987.

[103] J. Ricka. Dynamic light scattering with single-mode and multimode receivers. *Applied Optics*, 32:2860–2875, 1993.

[104] F.T. Arecchi; M. Corti; V. Degiorgio; S. Donati. Measurements of light intensity correlations in the subnanosecond region by photomultipliers. *Optics Communications*, 3:284–288, 197.

[105] K. Holst; H. Raether. The influence of thin surface flms on the plasma resonance emission. *Optics Communications*, 2:312–316, 1970.

[106] A. Otto; W. Sohler. Modifcation of the total refection modes in a dielectric film by one metal boundary. *Optics Communications*, 3:254–258, 197.

[107] M. Osterfeld; H. Franke; C. Feger. Optical gas detection using metal film enhanced leaky mode spectroscopy. *Appl. Phys. Lett.*, 62:2310–2312, 1993.

[108] H. Raether. *Surface plasmons on smooth and rough surfaces and on gratings.* Springer, 1988.

[109] A.H. Harvey; J.S. Gallagher; J.M.H. Levelt Sengers. Revised formulation for the refractive index of water and steam as a function of wavelength, temperature, and density. *Journal of Physical and Chemical Reference Data*, 27:761–774, 1998.

[110] J.D. Lytle. *Handbook of Optics: Devices, Measurements, and Properties, Second Edition.* McGraw-Hill Professional, 2003.

[111] *WINSPALL is a software computing reflectivity of optical multilayer systems. It is based on Fresnel's equations and the transfer matrix formalism and can be downloaded for free from: http://www.mpip-mainz.mpg.de/knoll/soft/.*

[112] R.G. Hunsperger. *Integrated optics: theory and technology.* Springer, 2009.

[113] A. Unger; U. Trutschel; U. Langbein. Design software for stratified optical systems with planar and cylindrical symmetry. *DGaO-Proceedings*, pages 1614–8436, 2007.

[114] G. Gantzounis. Plasmon modes of axisymmetric metallic nanoparticles: A group theory analysis. *J. Phys. Chem. C*, 113:21560–21565, 2009.

[115] H.C. van de Hulst. *Light Scattering by Small Particles.* Wiley:New York, 1957.

[116] S.W. Prescott; P. Mulvaney. Gold nanorod extinction spectra. *J. Appl. Phys.*, 99:123504–123507, 2006.

[117] B. Khlebtsov; V. Khanadeev; T. Pylaev; N.A. Khlebtsov. A new t-matrix solvable model for nanorods: Tem-based ensemble simulations supported by experiments. *J. Phys. Chem. C*, 115:6317–6323, 2011.

[118] J. Aitchison; J. Brown. *The Lognormal Distribution.* Cambridge University Press: New York, 1957.

[119] M. Tagliazucchi; M.G. Blaber; G.C. Schatz; E.A. Weiss; I. Szleifert. Optical properties of responsive hybrid Au@Polymer nanoparticles. *Acs Nano*, 6:8397–8406, 2012.

[120] Y. Han; A. Alsayed; M. Nobili; J. Zhang; T.C. Lubensky; A.G. Yodh. Brownian motion of an ellipsoid. *Science*, 314:626–630, 2006.

[121] S.M. Anthony; M. Kim; S. Granick. Translation-rotation decoupling of colloidal clusters of various symmetries. *J. Chem. Phys.*, 129:244701, 2008.

[122] D. La Torre; J. García; M.C.L. Martinez; M.M. Tirado. Dimensions of short, rodlike macromolecules from translational and rotational diffusion coefficients. study of the gramicidin dimer. *Biopolymers*, 23:611–615, 2004.

[123] M.M. Tirado; C.L. Martínez; J.G. de la Torre. Comparison of theories for the translational and rotational diffusion coefficients of rod-like macromolecules. application to short dna fragments. *J. Chem. Phys.*, 81:2047–2052, 1984.

[124] S. Ekgasit; A. Tangcharoenbumrungsuk; F. Yu; A. Baba; W. Knoll. Resonance shifts in spr curves of nonabsorbing, weakly absorbing, and strongly absorbing dielectrics. *Sensors and Actuators B: Chemical*, 105(2):532–541, 2005.

[125] J.W. Ha; K. Marchuk; N. Fang. Focused orientation and position imaging (fopi) of single anisotropic plasmonic nanoparticles by total internal reflection scattering microscopy. *Nano Lett.*, 12:4282–8, 2012.

[126] J.J. Mock; R.T. Hill; A. Degiron; S. Zauscher; A. Chilkoti; D.R. Smith. Distance-dependent plasmon resonant coupling between a gold nanoparticle and gold film. *Nano Lett.*, 8:2245–2252, 2008.

[127] H.J. Butt; K. Graf; M. Kappl. *Physics and Chemistry of Interfaces*. Wiley-VCH Verlag, Weinheim, 2004.

[128] B. Nikoobakht; M.A. El-Sayed. Evidence for bilayer assembly of cationic surfactants on the surface of gold nanorods. *Langmuir*, 17:6368–6374, 2001.

[129] T.K. Sau; C.J. Murphy. Self-assembly patterns formed upon solvent evaporation of aqueous cetyltrimethylammonium bromide-coated gold nanoparticles of various shapes. *Langmuir*, 21:2923–2929, 2005.

[130] B. Nikoobakht; J. Wang; M.A. El-Sayed. Surface-enhanced raman scattering of molecules adsorbed on gold nanorods: off-surface plasmon resonance condition. *Chemical Physics Letters*, 366:17–23, 2002.

[131] S. Lee; L.J. Anderson; C.M. Payne; J.H. Hafner. Structural transition in the surfactant layer that surrounds gold nanorods as observed by analytical surface-enhanced raman spectroscopy. *Langmuir*, 27:14748–14756, 2011.

[132] M. Sethi; G. Joung; M.R. Knecht. Linear assembly of au nanorods using biomimetic ligands. *Langmuir*, 25(3):1572–1581, 2009.

[133] S. Zhang; X. Kou; Z. Yang; Q. Shi; G.D. Stucky; L. Sun; J. Wang; C. Yan. Nanonecklaces assembled from gold rods, spheres, and bipyramids. *Chem. Commun.*, (18):1816–1818, 2007.

[134] K. Liu; Z. Nie; N. Zhao; W. Li; M. Rubinstein; E. Kumacheva. Step-growth polymerization of inorganic nanoparticles. *Science*, 329(5988):197–200, 2010.

[135] K. Caswell; J.N. Wilson; U.H. Bunz; C.J. Murphy. Preferential end-to-end assembly of gold nanorods by biotin-streptavidin connectors. *J. Am. Chem. Soc.*, 125(46):13914–13915, 2003.

[136] N.R. Jana; L. Gearheart; S.O. Obare; C.J. Murphy. Anisotropic chemical reactivity of gold spheroids and nanorods. *Langmuir*, 18(3):922–927, 2002.

[137] C.J. Orendorff; T.M. Alam; D.Y. Sasaki; B.C. Bunker; J.A. Voigt. Phospholipid-gold nanorod composites. *Acs Nano*, 3(4):971–983, 2009.

[138] H. Liao; J.H. Hafner. Gold nanorod bioconjugates. *Chem. Mat.*, 17(18):4636–4641, 2005.

[139] H. Takahashi; Y. Niidome; T. Niidome; K. Kaneko; H. Kawasaki; S. Yamada. Modification of gold nanorods using phosphatidylcholine to reduce cytotoxicity. *Langmuir*, 22(1):2–5, 2006.

[140] D. Johannsmann; I. Reviakine; E. Rojas; M. Gallego. Effect of sample heterogeneity on the interpretation of qcm (-d) data: comparison of combined quartz crystal microbalance/atomic force microscopy measurements with finite element method modeling. *Analytical chemistry*, 80:8891–8899, 2008.

[141] P.M. Karlsson; A.E. Palmqvist; K. Holmberg. Adsorption of sodium dodecyl sulfate and sodium dodecyl phosphate on aluminum, studied by qcm-d, xps, and aas. *Langmuir*, 24:13414–13419, 2008.

[142] H.N. Patrick; G.G. Warr; S. Manne; I.A. Aksay. Surface micellization patterns of quaternary ammonium surfactants on mica. *Langmuir*, 15:1685–1692, 1999.

[143] S. Manne; J. Cleveland; H. Gaub; G. Stucky; P. Hansma. Direct visualization of surfactant hemimicelles by force microscopy of the electrical double layer. *Langmuir*, 10:4409–4413, 1994.

[144] F. Tiberg; B. Joesson; B. Lindman. Ellipsometry studies of the self-assembly of nonionic surfactants at the silica-water interface: kinetic aspects. *Langmuir*, 10:3714–3722, 1994.

[145] F. Tiberg; B. Joensson; J.a. Tang; B. Lindman. Ellipsometry studies of the self-assembly of nonionic surfactants at the silica-water interface: Equilibrium aspects. *Langmuir*, 10:2294–2300, 1994.

[146] G. Fragneto; R.K. Thomas; A.R. Rennie; J. Penfold. Neutron reflection from hexadecyltrimethylammonium bromide adsorbed on smooth and rough silicon surfaces. *Langmuir*, 12:6036–6043, 1996.

[147] I. Purcell; J. Lu; R. Thomas; A. Howe; J. Penfold. Adsorption of sodium dodecyl sulfate at the surface of aqueous solutions of poly (vinylpyrrolidone) studied by neutron reflection. *Langmuir*, 14:1637–1645, 1998.

[148] J. Penfold; I. Tucker; J. Petkov; R. Thomas. Surfactant adsorption onto cellulose surfaces. *Langmuir*, 23:8357–8364, 2007.

[149] Z.M. Sui; X. Chen; L.Y. Wang; L.M. Xu; W.C. Zhuang; Y.C. Chai; C.J. Yang. Capping effect of ctab on positively charged ag nanoparticles. *Physica E: Low-dimensional Systems and Nanostructures*, 33(2):308–314, 2006.

[150] B.M. van der Zande; J.K. Dhont; M.R. Böhmer; A.P. Philipse. Colloidal dispersions of gold rods characterized by dynamic light scattering and electrophoresis. *2000*, 16:459–464, Langmuir.

[151] C.M. Hu; R. Zwanzig. Rotational friction coefficients for spheroids with the slipping boundary condition. *J. Chem. Phys.*, 60:4354, 1974.

[152] Q.Q. Zhan; J. Qian; X. Li; S. He. A study of mesoporous silica-encapsulated gold nanorods as enhanced light scattering probes for cancer cell imaging. *Nanotechnology*, 21:055704, 2010.

[153] G.I. Stegeman; J.J. Burke; D.G. Hall. Surface-polaritonlike waves guided by thin, lossy metal films. *Optics Letters*, 8:383–385, 1983.

[154] P. Berini. Long-range surface plasmon polaritons. *Adv. Opt. Photon*, 1:484–588, 2009.

[155] J. Dostálek; R.F. Roskamp; W. Knoll. Coupled long range surface plasmons for the investigation of thin films and interfaces. *Sensors and Actuators B: Chemical*, 139:9–12, 2009.

Acknowledgment

[in printed version available]

[in printed version available]

Curriculum Vitæ

[in printed version available]

[in printed version available]

[in printed version available]